Title

Metal–Organic Frameworks Composed of Metal Nanocrystals and Metal Complexes for Heterogeneous Catalysis and Hydrogen Storage

Author

Rungtaweevoranit, Bunyarat

Publication Date

2018

Metal–Organic Frameworks Composed of Metal Nanocrystals and Metal Complexes for Heterogeneous Catalysis and Hydrogen Storage

By

Bunyarat Rungtaweevoranit

A dissertation submitted in partial satisfaction of the

requirements for the degree of

Doctor of Philosophy

in

Chemistry

in the

Graduate Division

of the

University of California, Berkeley

Committee in charge:

Professor Omar M. Yaghi, Chair
Professor Felix R. Fischer
Professor Alex Zettl

Spring 2018

Abstract

Metal–Organic Frameworks Composed of Metal Nanocrystals and Metal Complexes for Heterogeneous Catalysis and Hydrogen Storage

by

Bunyarat Rungtaweevoranit

Doctor of Philosophy in Chemistry

University of California, Berkeley

Professor Omar M. Yaghi, Chair

The assembly of organic and inorganic building units into porous crystalline structures has given rise to metal-organic frameworks (MOFs). The wide variety of these building blocks has propelled the discovery of MOFs with new structures, topologies and chemical properties. In retrospect, MOFs itself can be used as a building unit for subsequent synthesis to impart functionalities for specific purposes. In this dissertation, I used MOFs as a building unit for functionalizing metal nanocrystals (NCs) and for post-synthetic modifications of their interior to synthesize metal complexes for heterogeneous catalysis and hydrogen storage.

Following this direction, a zirconium-based MOF, UiO-66, was used to encapsulate copper NCs to affect the catalytic activity of copper NC for CO_2 hydrogenation to methanol. In this construct, a periodic array of zirconium oxide clusters is situated on the Cu surface resulting in high interfacial contact between copper NC and zirconium oxide clusters. We found that this catalyst is highly active and selective for the synthesis of methanol. Systematic investigations and X-ray photoelectron spectroscopy suggest the presence of the interaction between copper NC and zirconium oxide cluster at the interface, also known as strong–metal support interaction (SMSI), that leads to such catalytic performance.

We have used the same interaction to anchor a single atom of copper on the missing linker defect site of zirconium oxide clusters of UiO-66. The resulting catalyst is highly active for CO oxidation with high stability and selectivity for CO oxidation. In-situ X-ray absorption spectroscopy and in-situ infrared spectroscopy show that the single copper site remains isolated throughout the heat treatment under different gases including nitrogen and hydrogen even at 350 °C.

With regard to modifications of MOF interior, MOFs have a wide range of structures, topologies and chemical functionalities primed for creating a complexity akin to the active sites of enzymes. We employed this diversity to create an active site inspired by particulate methane monooxygenase (pMMO), an enzyme that oxidizes methane to methanol in nature with high activity and high selectivity. By judicious selection of MOF with desired geometric parameters, we used MOF-808 as a precursor for post-synthetic modifications to install ligands bearing

imidazole units and metalation with Cu(I) in the presence of dioxygen. The catalysts show high selectivity for methane oxidation to methanol under isothermal conditions at 150 °C. Combined spectroscopies and density functional theory calculations reveal bis(μ-oxo) dicopper species as the active site of the catalysts.

Finally, we have employed the post-synthetic modification of MOFs to install metal sites functioning as hydrogen adsorption sites for gas storage purpose. In this work, IRMOF-74-III equipped with primary amines was functionalized to install metal-binding ligands including Schiff base and catecholate ligands. The MOFs were subsequently metalated with Ni(II) and tested for hydrogen adsorption properties.

---

*The work includes material (text and figures) from Rungtaweevoranit, B.; Diercks, C. S.; Kalmutzki, M. J.; Yaghi, O. M. Progress and prospects of reticular chemistry. *Faraday Discuss.* **2017,** *201*, 9. Rungtaweevoranit, B.; Baek, J.; Araujo, J. R.; Archanjo, B. S.; Choi, K. M.; Yaghi, O. M.; Somorjai, G. A. Copper Nanocrystals Encapsulated in Zr-based Metal–Organic Frameworks for Highly Selective CO_2 Hydrogenation to Methanol. *Nano Lett.* **2016,** *16*, 7645. Rungtaweevoranit, B.; Zhao, Y.; Choi, K. M.; Yaghi, O. M. Cooperative effects at the interface of nanocrystalline metal–organic frameworks. *Nano Res.* **2016,** *9*, 47. The use of co-authored material is permitted by all contributing authors. The material is reproduced with permission. Copyright 2017 Royal Society of Chemistry. Copyright 2016 American Chemical Society. Copyright 2016 Springer Nature.

To my parents and my grandmother

Table of Contents

Acknowledgments

I would like to thank my research advisor Professor Omar M. Yaghi for persuading me to come to UC Berkeley and his support throughout my study. His guidance and honest criticism have impacted the way I approach problems. I am thankful to my qualifying exam and thesis committee members Professors Felix R. Fischer, Alex Zettl, K. Peter C. Vollhardt and John Arnold for their helpful comments and suggestions.

I thank Kyungmin Choi and Peter Siman for mentorship during the first few years in the lab. I am grateful to the Yaghi group members for all the discussions in various aspects, particularly Alejandro M. Faracaroli, Christopher A. Trickett, Hiroyasu Furukawa, Hyung Mo Jeong, Philipp Urban, Eugene Kapustin, Roc Matheu, Seungkyu Lee, Juncong Jiang, Yingbo Zhao, Chenfei Zhao, Yue-Biao Zhang, Xiaokun Pei, Robinson Flaig and Christian Diercks. I wish to thank my collaborators outside the Yaghi lab: Professor Gabor Somorjai, Professor R. Jürgen Behm and Ali M. Abdel-Mageed. I would like to thank Karen Wong and Markus Kalmutzki for being on top of things and keeping the labs in order. I am thankful to Roc Matheu and Robinson Flaig for proofreading of my dissertation.

I am grateful to Dr. Jayeon Baek for her patience and collaboration. I have learned so many things in catalysis throughout the collaboration with her.

I thank my undergraduate research advisor Assoc. Prof. Tienthong Thongpanchang for his motivation and guidance during my undergraduate study. I would not have been where I am now if not for his encouragement.

I would like to thank Kananat Naksomboon for the joy we have together and putting up with me through my graduate study.

I thank my dad, mom and grandma for being supportive and allowing me to pursue my dream.

VITA

Jul. 14, 1988	Born, Bangkok, Thailand
Mar., 2010	B. Sc. (Chemistry) Department of Chemistry Mahidol University Bangkok, Thailand
Jun., 2013	M. Sc. (Organic Chemistry) Department of Chemistry Mahidol University Bangkok, Thailand
Aug., 2013 – Present	Graduate Student Instructor and Researcher Department of Chemistry University of California, Berkeley Berkeley, California, United States

PUBLICATIONS

Rungtaweevoranit, B.; Diercks, C. S.; Kalmutzki, M. J.; Yaghi, O. M. *Faraday Discuss.* **2017,** *201*, 9–45.

Choi, K. M.; Kim, D.; Rungtaweevoranit, B.; Trickett, C. A.; Barmanbek, J. T. D.; Yang, P.; Yaghi, O. M. *J. Am. Chem. Soc.* **2017,** *139*, 356.

Rungtaweevoranit, B.; Baek, J.; Araujo, J. R.; Archanjo, B. S.; Choi, K. M.; Yaghi, O. M.; Somorjai, G. A. *Nano Lett.* **2016,** *16*, 7645.

Rungtaweevoranit, B.; Zhao, Y.; Choi, K. M.; Yaghi, O. M. *Nano Res.* **2016,** *1*, 47.

Chapter 1

Introduction

1.1 General Aspects of Metal–Organic Frameworks

Metal–organic frameworks (MOFs) are porous crystalline solids that are constructed by linking metal oxide clusters with organic linkers to produce three-dimensional structures. The porous nature of this class of materials allows guest molecules to diffuse in and out freely, a desirable quality for a wide range of applications such as catalysis and gas storage.[1] One prominent example of MOF is MOF-5 which is synthesized from linking $Zn_4O(\text{-}CO_2)_6$ octahedral secondary building units (SBUs) with benzenedicarboxylate (BDC^{2-}) to provide a cubic framework (Figure 1.1).[2] The covalent linkages between rigid multimetallic clusters and the organic linkers impart the structural stability to this MOF which allowed for examination of its porosity by gas adsorption measurement. The N_2 adsorption isotherm measured at 77 K of this MOF shows a Brunauer-Emmett-Teller (BET) surface area of 2,320 $m^2\ g^{-1}$.

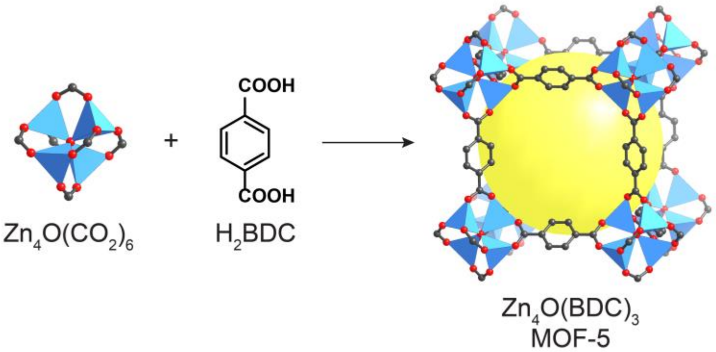

Figure 1.1. Construction of MOF-5 that comprises $Zn_4O(\text{-}CO_2)_6$ and H_2BDC. Atom labeling scheme: C, black; O, red; Zn, blue polyhedra. H atoms are omitted for clarity. The yellow sphere represents the space in the framework.

Because MOFs are synthesized from two classes of materials, i.e. inorganic and organic building blocks with each having an array of different structures, a wide variety of MOFs have been synthesized along their intriguing structures possessing different kinds of topology, local chemical properties, and gas adsorption profile (Figure 1.2).[3] In addition to MOFs with different topologies, substitution of organic building blocks with others having the same type of linkages produces MOFs with functionalities without changing the underlying topology of the structures (Figure 1.3). Up until 2017, more than 70,000 crystal structures of MOFs have been deposited in Cambridge Structural Database making it the largest class of porous crystalline structures reported to date.[3] Such a large pool of MOFs can be used as a precursor for post-synthetic modification or integration with other materials to obtain MOFs with unique properties.

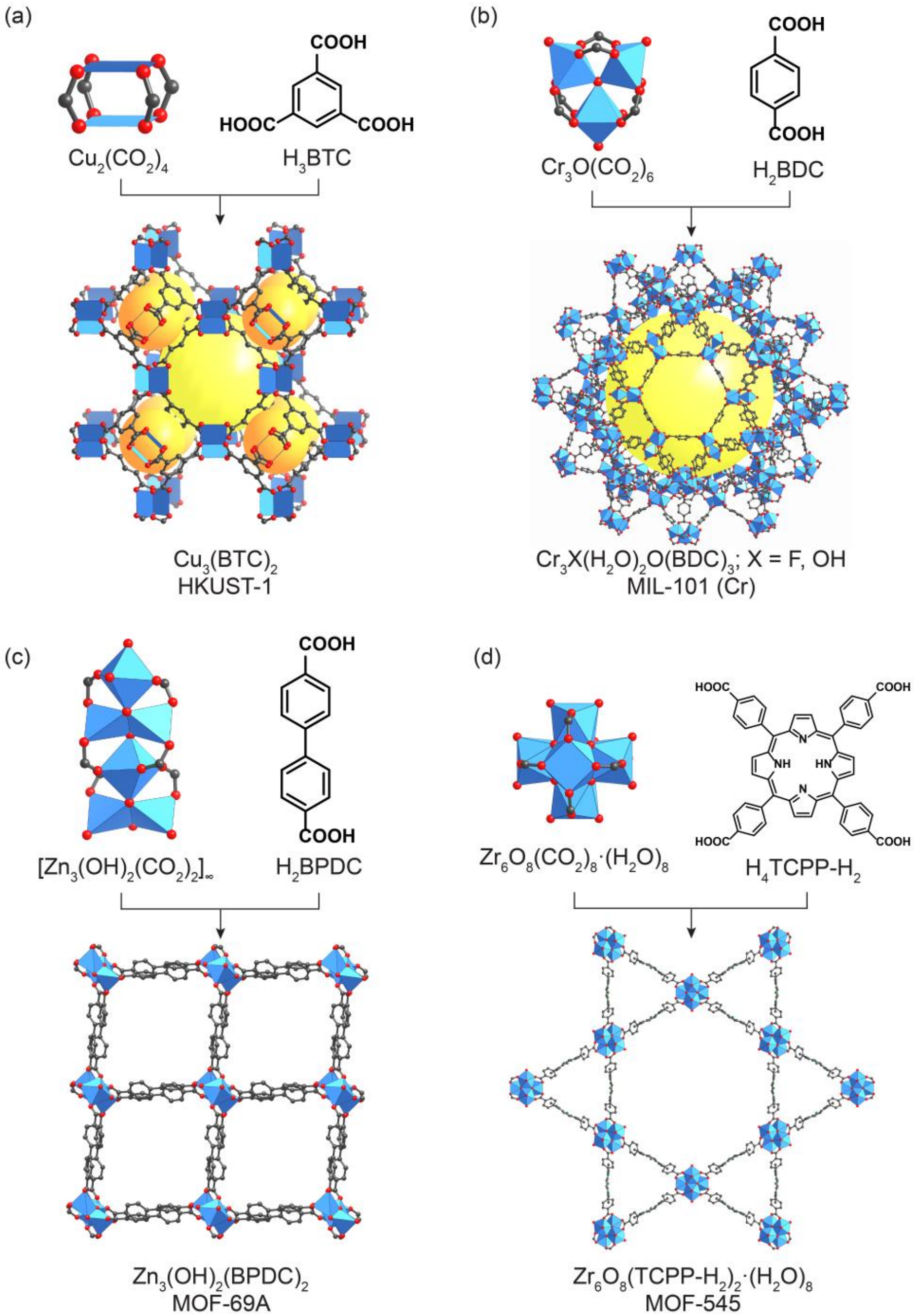

Figure 1.2. Combination of different kinds of multimetallic clusters and organic linkers leads to a wide variety of MOF structures possessing varying topologies. Atom labeling scheme: C, black; O, red; metals, blue polyhedra. H atoms are omitted for clarity. Yellow and orange spheres represent the space in the framework.

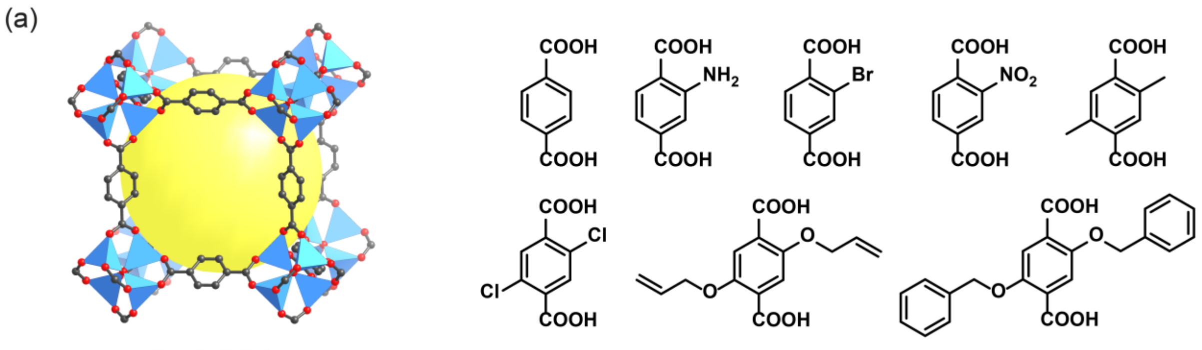

$Zn_4O(BDC)_3$
MOF-5

Selection of organic linkers for isoreticular functionalization of MOF-5

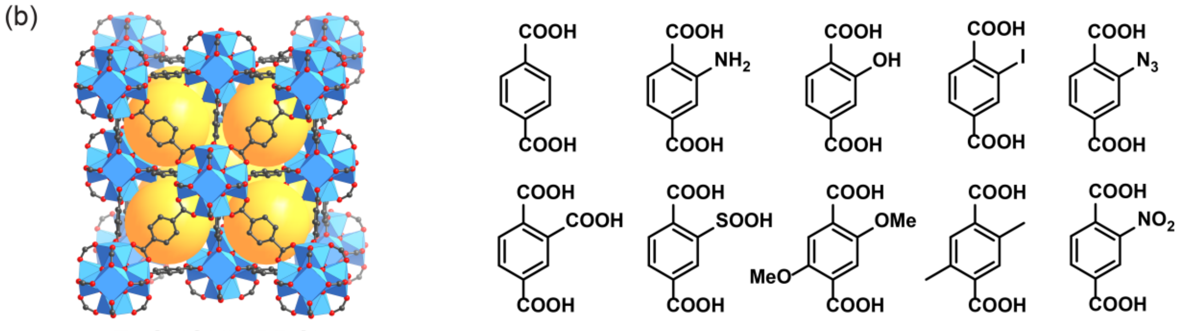

$Zr_6O_4(OH)_4(BDC)_6$
UiO-66

Selection of organic linkers for isoreticular functionalization of UiO-66

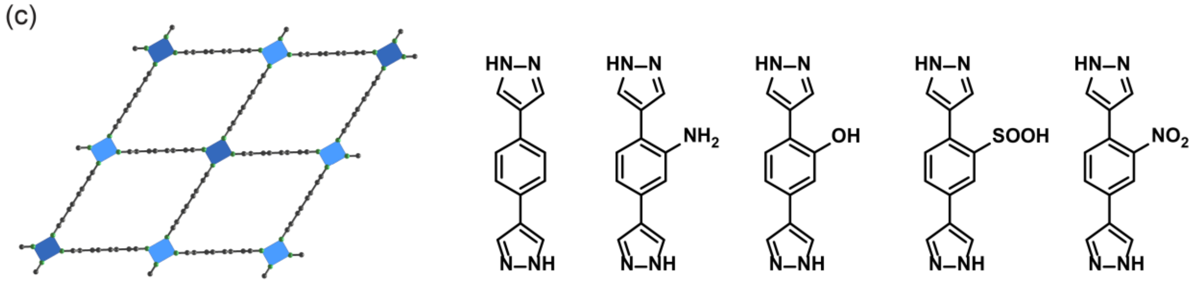

Ni(BDP)

Selection of organic linkers for isoreticular functionalization of Ni(BDP)

Figure 1.3. Substitution of organic linkers with functionalized ones can produce MOFs with functionalities. Atom labeling scheme: C, black; O, red; metals, blue polyhedra. H atoms are omitted for clarity. Yellow and orange spheres represent the space in the framework.

The assembly of inorganic and organic building blocks into one crystal provides an opportunity to functionalize and craft the interior of a MOF by employing the synthetic procedures developed from inorganic and organic chemistry.[4] The well-defined structure of MOFs allows this chemistry to be performed with high tunability and high precision. Such attributes are desirable not only for creating new kinds of materials but also for designing the interface.

1.2 Integration of MOFs with Metal Nanocrystals

The integration of MOF with metal nanocrystals (NCs) provides a mean for controlling the chemistry at the interface of nanocrystalline solids and achieving properties unattainable by individual species where both materials could function synergistically.[5] Incorporation of metal NCs within MOF in a well-defined nanostructure offers an opportunity not only to tailor the properties of the resulting hybrid materials but also the ability to elucidate the structure at the interface. The construction of these hybrid nanostructures may lead to materials with unique plasmonic effects,[6] improved stability,[7] enhanced gas sorption properties[8] and novel catalytic processes.[9] One of the earliest approach to integrate metal NCs in MOF employs the impregnation of metal precursors into the MOF pores followed by reduction of those metal salts.[10] This process results in the deposition of metal NCs of varying sizes penetrating through the multiple-pore network. To alleviate this problem, a coordinating group such as amine has been introduced into the pore of MOF to enhance the interaction between the metal precursor and the framework prior to reduction of the metal salt. Synthesis of Pd NCs in a MOF using this method shows a fine dispersion of metal NCs inside the framework.[11]

To express better control over the design of the mesoscopic construct, metal NCs are pre-synthesized and subsequently encapsulated within MOFs. This approach offers opportunities to control metal nanomaterials' size, morphology, composition, location and order which are important features that largely determine the properties of nanomaterials in most applications. Here, the metal NCs are synthesized with the desired metrics and then encapsulated into MOFs.[6a,12] The common synthetic approach to realize this is to synthesize MOFs in the presence of NCs. By selecting suitable capping agents on the NCs' surface, metal NCs can then be readily dispersed in the MOF synthesis solution and functionalities of these capping agents can interact with MOF crystal nuclei inducing the heterogeneous nucleation of MOF on the surface of NCs. At the same time, the MOF synthetic conditions should be controlled to suppress homogeneous nucleation by varying the concentration of linker and metal precursor, temperature, and reaction time. A general method for encapsulation was demonstrated in 2012 with the synthesis of various nanoparticles, such as Pt, CdTe, Fe_3O_4 and lanthanide-doped $NaYF_4$ NCs, Ag nanocubes, polystyrene nanospheres, β-FeOOH nanorods and lanthanide-doped $NaYF_4$ nanorods, encapsulated in ZIF-8 [$Zn(mIM)_2$; mIM^- = 2-methylimidazolate] (Figure 1.4).[13] The surface of nanoparticles was functionalized with polyvinylpyrrolidone (PVP), which not only maintains the colloidal stability of the nanoparticles but also increases their interactions with ZIF-8.

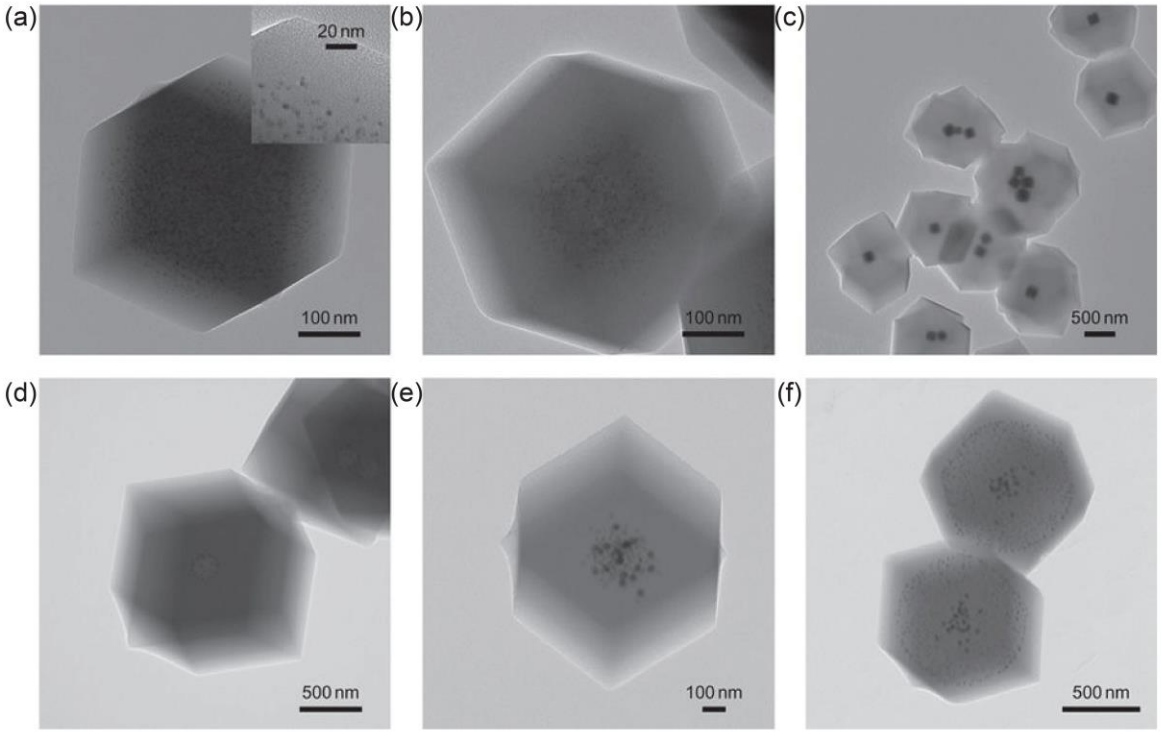

Figure 1.4. TEM images of inorganic NPs incorporated in ZIF-8: (a) 3.3 nm Pt NCs in ZIF-8 at 3.3 wt%, (b) 3.3 nm Pt NCs in ZIF-8 at 0.7 wt%, (c) 160 nm Ag cubes in ZIF-8, (d) 13 nm Au NCs adsorbed on 180 nm polystyrene spheres in ZIF-8, (e) 13 nm and 34 nm Au NPs in ZIF-8, (f) 34 nm Au NPs rich cores and 13 nm Au NPs rich shell in ZIF-8. Copyright 2012 Nature Publishing Group.

Having catalytically active metal NCs enclosed within a crystalline structure of MOF is intriguing from the catalytic point of view because the catalytic performance of metal NCs is largely controlled by structure and properties at the catalyst surface. Common factors affecting the catalytic properties include size, composition and morphology of metal NCs and their exterior. In comparison to other factors, the exteriors of metal NCs are generally ill-defined and hence difficult to study and control the catalytic properties. MOF coatings around metal NCs can provide a tunable environment where chemical functionalities can be controlled through MOF chemistry while the main constructs remain unchanged. As an example, Pt NCs fully encapsulated within UiO-66 [$Zr_6(OH)_4O_4(BDC)_6$; BDC^{2-}=1,4-benzenedicarboxylate] were prepared and studied for catalytic conversion of methylcyclopentane.[14] In this construct, Pt NCs of the same size and shape were used allowing a systematic study of catalytic properties arising from the change in the exterior of Pt NCs. The chemical environment around Pt NCs was controlled by the encapsulation of Pt NCs in UiO-66 with different functionalities on H_2BDC linker including NH_2/–NH_3^+ (denoted as Pt⊂UiO-66-N* and Pt⊂UiO-66-N), –SOOH/–SOO^- (denoted as Pt⊂UiO-66-S and Pt⊂UiO-66-S*) or a combination of both functionalities (Figure 1.5a and b). Pt⊂UiO-66-S exhibited 62.4% selectivity toward cyclohexane, the highest reported for this reaction while the catalytic activity was enhanced by 2-fold in comparison to Pt-on-SiO_2 and Pt⊂nUiO-66 (Figure 1.5c and d). This enhancement has been attributed to the synergistic catalytic interplay of Pt NCs and the strong acidic sites of the sulfonic acid in UiO-66. Further, the structure, integrity and catalytic performance remained unaltered after the reaction. The stability together with the tunable MOF structures indicates that MOFs can serve as a platform for heterogeneous catalysis.

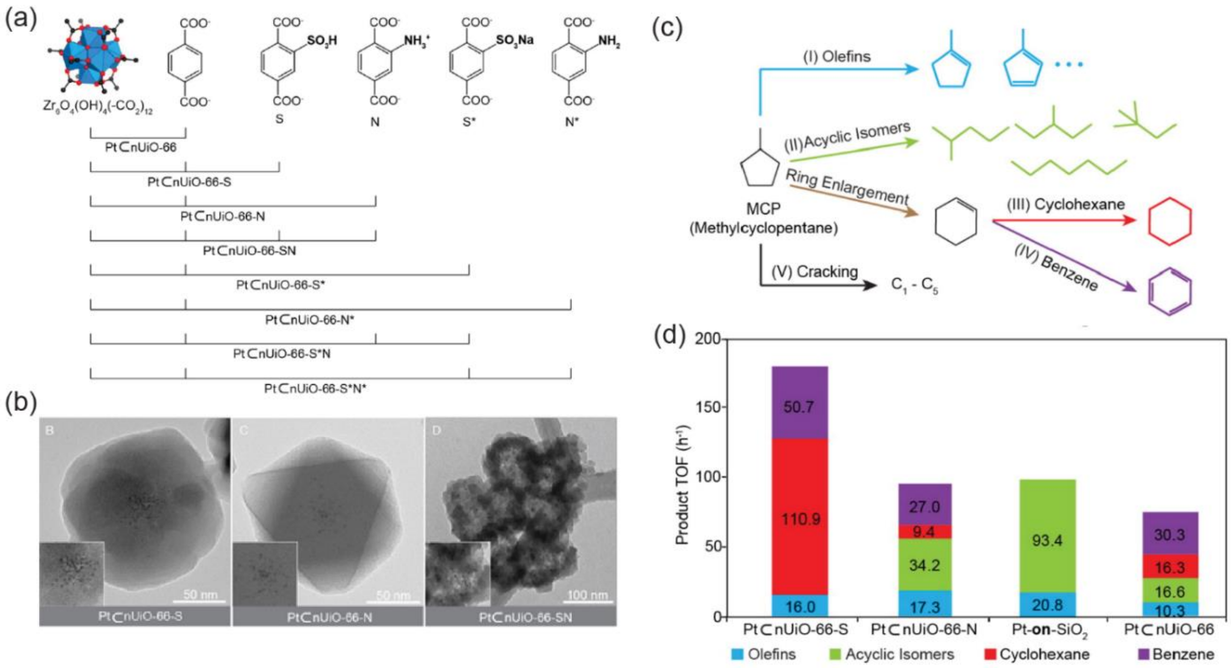

Figure 1.5. (a) Combination of functionalized linkers used to make nMOFs in the Pt⊂nUiO-66 constructs (b) TEM images of Pt⊂nUiO-66 constructs (c) Schematic reaction diagram of the conversion of MCP (d) turnover frequency (TOF, h^{-1}) obtained at 150 °C over Pt⊂nUiO-66-S and N, Pt⊂nUiO-66, and Pt-on-SiO_2. Copyright 2015 American Chemical Society.

Another example of controlling the catalytic reaction at the surface of nanocrystals involves Pt NCs sandwiched within MOFs where open metal sites are positioned over the entire nanocrystal, thereby interacting with substrates during catalysis (Figure 1.6).[15] As a result, selective hydrogenations towards carbonyl over carbon-carbon double bonds in α,β-unsaturated aldehydes were achieved.

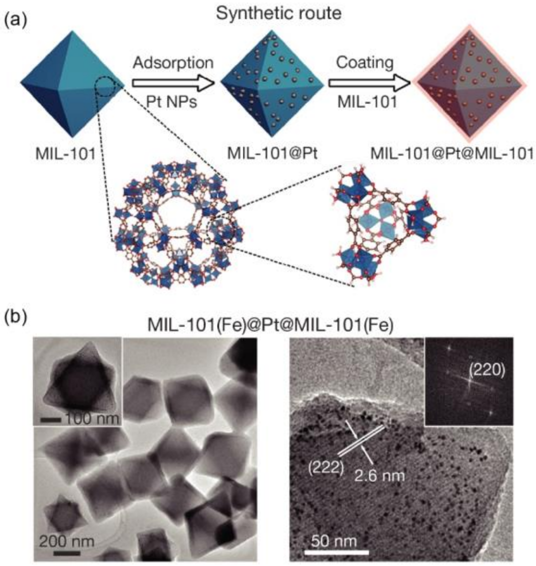

Figure 1.6. Pt NCs were sandwiched between the MOFs which regulate the hydrogenation selectivity. Shown are the synthetic route (a) and TEM images (b) of the sandwich nanostructure. Copyright 2016 Nature Publishing Group.

1.3 Anchoring Metal onto SBUs of MOFs

The ability to maximize the specific surface area of the metal NCs is desirable in heterogeneous catalysis because only the surface of these active sites participate in the catalytic cycle.[16] Besides maximizing the specific surface area through size reduction, the catalytic properties of the NCs change drastically once the particle diameter is reduced into the nanoregime, particularly less than 10 nm.[17] This is due to the significant increase in the number of low coordinated metal atoms; substantial changes in surface atomic structure, electronic structure and defects. In many cases, it has been shown that reduction in particle size enhances catalytic activity and selectivity or even displays unusual catalytic performance. There have been intensive efforts in decreasing the size of these particles down to its atomic limit and that is in the realm of single-atom catalysis.[18] However, such high surface free energy of single atom results in high propensity for these atoms to migrate and sinter during the reaction. One approach to address this problem involves the use of extremely low loading of metal on metal oxide supports. Following this approach, single-atom Pt_1/FeO_x catalyst was prepared by controlling Pt loading to 0.17 wt% to give a fine dispersion of single Pt atom on FeO_x support.[19] The catalyst was then subjected to hydrogenation. Extended X-ray absorption fine structure (EXAFS) indicates the presence of Pt–O coordination suggesting the strong metal-support interaction between Pt and the FeO_x. This interaction has been ascribed to enhance the stability of single atom in this catalyst.

However, this approach does not provide the absolute control over the density of metal active per volume or area because they rely on using extremely dilute amount of metal precursor. In contrast to conventional metal oxides where M–O is a repeating unit of the entire structure, MOFs are composed of isolated clusters of metal oxide separated by organic linkers. The isolated nature of metal oxides provides new opportunities for creating site isolated active sites. In addition, metal oxide clusters in MOF have a wide variety in size, shape and composition. Regarding the size, it can vary from just one atom as in a single metal node or an infinite number of atoms where metal atoms in an SBUs are connected as a rod. At the same time, the composition of SBUs can also vary greatly from having only one kind metal up to 10 different kinds of metals in one SBU.

Zr-based MOFs are an ideal platform for anchoring metal active site on the SBUs due to the presence of hydroxy group on the SBUs. Atomic layer deposition in MOFs technique (AIM) has been developed to deposit metal onto the SBU of a MOF where volatile metal precursors are introduced into the MOF pore in gas phase. NU-1000, a Zr-based MOF composed of $Zr_6O_4(OH)_4(H_2O)_4(OH)_4$ and 1,3,6,8-tetrakis(*p*-benzoate)pyrene ($TBAPy_4^{-}$) linkers (Figure 1.7a), was used to install Ni site onto the SBU (Figure 1.7b) in which the Ni loading was found to be 4.1 Ni atoms per Zr_6 node.[20] This Ni-NU-1000 catalyst displayed long-term stability for ethylene hydrogenation and Ni ions are isolated throughout the catalytic reaction.

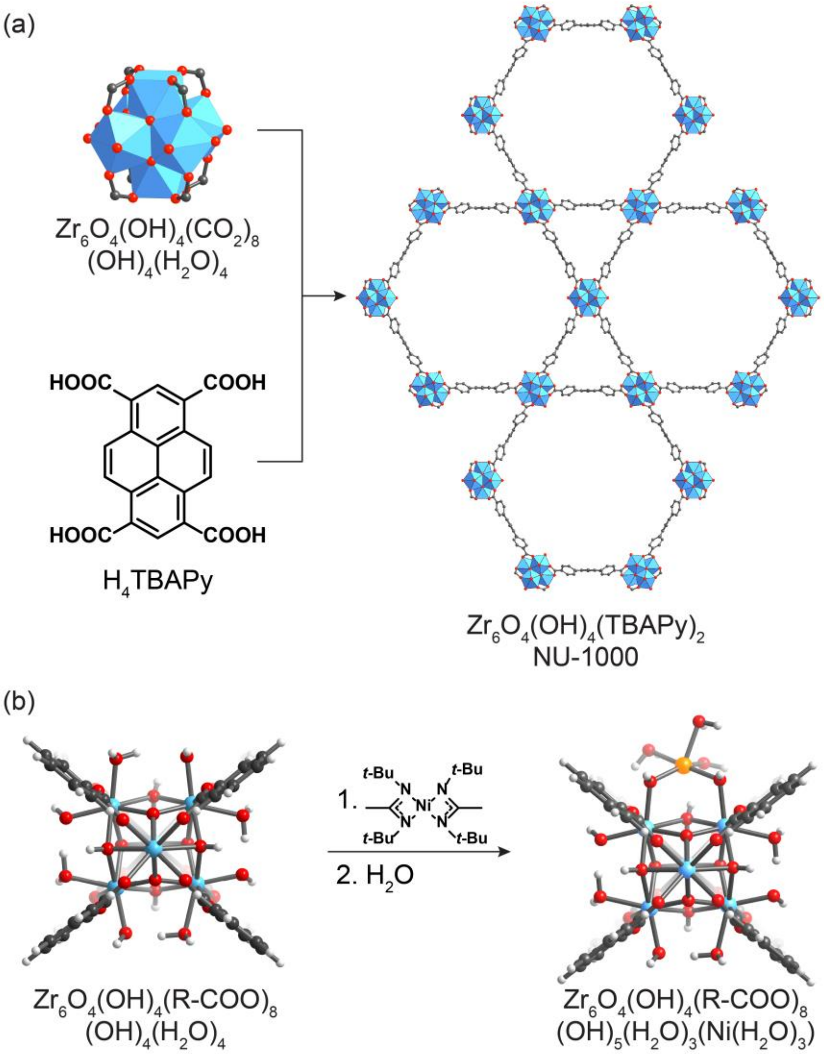

Figure 1.7. (a) Crystal structure of NU-1000 and (b) installation of Ni atom onto the cluster using AIM.

1.4 Functionalization of MOFs to Create Catalytic Sites Inspired by Enzymes

Due to a large variety of structures of MOFs with available sites for functionalization situated in three-dimensional space, one can envisage that post-synthetic modification of these materials can create an active site with complexities of enzymes.

Enzymes have been a source of inspiration for designing novel catalysts because of their high selectivity and ability to operate under mild temperature and pressure conditions.[21] In enzymes, a number of active sites require that certain functional groups are located in specific patterns or enclosed within space to prevent undesired reaction pathway. To hold these functionalities provided by the side chain of amino acids, nature uses peptide backbone of specific sequences to create secondary or tertiary structures to encompass the space of which functionalities are contained. In analogy, MOF scaffold may serve as a secondary or tertiary structure and the functionalities may be incorporated into the MOF during post-synthetic modifications.

As an example, Mg-IRMOF-74-III [Mg_2(DH3PHDC), $DH3PHDC^{4-}$ = dioxido-(1,1′:4′,1″-terphenyl)-4,4″-dicarboxylate] functionalized with primary amine was post-synthetically modified with amino acids through seven post-synthetic modification steps to introduce a short peptide, a Cis–His–Asp chain, in its interior resulting in a material capable of catalyzing a selective bond breaking reaction, a catalytic selectivity similar to the active site of the tobacco etch virus (Figure 1.8).[22]

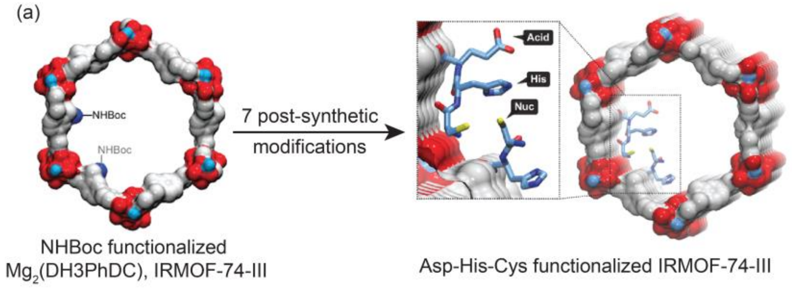

NHBoc functionalized Mg_2(DH3PhDC), IRMOF-74-III

Asp-His-Cys functionalized IRMOF-74-III

Figure 1.8. Amine functional groups in functionalized IRMOF-74-III were post-synthetically functionalized with amino acids leading to catalytic sites similar to TEV endoprotease. Copyrights 2016 American Chemical Society.

1.5 Functionalization and Metalation in MOFs for Hydrogen Storage

One of the earliest applications explored in MOFs is gas storage due to its high specific surface area. Such high surface area can be expected because almost every atom in MOF structure is exposed to adsorbate. Single crystal diffraction experiments on MOF-5 conducted at 30 K at various stages of Argon pressure reveals primary gas adsorption sites located near the SBUs followed by the organic linkers (Figure 1.9).[23]

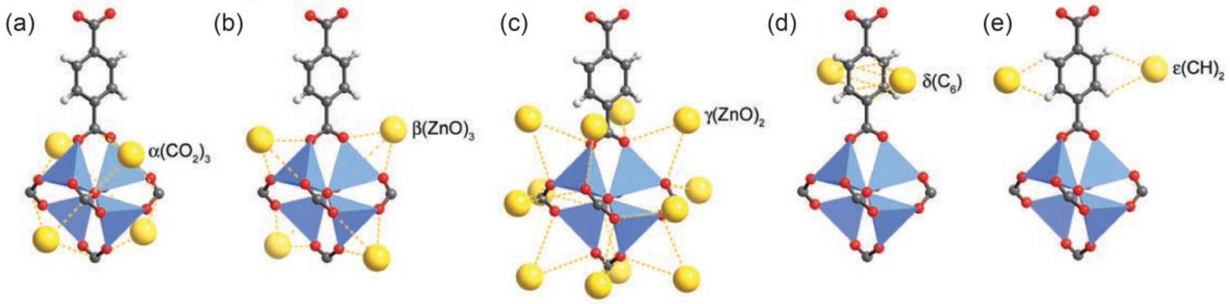

Figure 1.9. Single crystal X-ray diffraction study of adsorption sites in MOF using Ar gas as a probe to locate the location of adsorption at 30 K. This study reveals three primary adsorption sites associated with the SBU (a–c) and two adsorption sites associated with the organic linker. Copyright 2005 American Association for the Advancement of Science.

With the knowledge of adsorption sites known, MOF-177 [$Zn_4O(BTB)_2$, BTB^{3-}=4,4',4''-benzene-1,3,5-triyl-tribenzoate] with the ultrahigh surface area was reported which maximizes the gas adsorption site on the framework by using the long organic linker.[24] Subsequently, many more MOFs with even higher surface areas have been synthesized.[25] Such high surface areas are particularly important in gas storage applications such as hydrogen. Systematic studies on the gravimetric uptake of hydrogen of various MOFs reveals a linear correlation between surface area and hydrogen uptake.[26] Inelastic neutron scattering also confirms that the presence of adsorption site of hydrogen similar to what was observed in single crystal gas adsorption studies of Ar.[27]

However, in practical applications for on-board hydrogen storage, suitable sorbent materials must be able to store hydrogen at ambient conditions. According to the 2025 DOE targets for onboard hydrogen storage for light-duty vehicles, the system, which includes the sorbent and container, must have a volumetric capacity of 40 g L^{-1} and a gravimetric capacity of 5.5 wt% operating at ambient temperature and applicable pressure.[3] Hydrogen has negligible dipole moment making it difficult to polarize and store the gas molecules using only van der Waals interaction.[28] It has been calculated that adsorption enthalpy between a hydrogen molecule and the sorbent must reach 15 kJ mol^{-1} in order to achieve the DOE target.[29] One of the most promising strategies to enhance the adsorption enthalpy is the use of open metal sites through charge-induced dipole interaction.[30] The current record holder is Ni_2(*m*-dobdc) which utilized the open metal sites to achieve the hydrogen uptake of 12 g L^{-1} at 25 °C and 100 bar.[31]

The objective of this dissertation is to impart functionalities in MOFs by (a) integration of MOFs with metal NCs and (b) post-synthetic modifications to affect catalytic properties and gas adsorption properties.

Chapter 2 describes the systematic investigation of a strong-metal support interaction (SMSI) in MOFs of a catalyst where single Cu nanocrystal (NC) is encapsulated within a single crystal of a Zr-based MOF, UiO-66, for CO_2 hydrogenation to methanol. SMSI has been known in metal/metal oxide systems since 1978 and been demonstrated to affect catalytic properties in many industrial catalysts.[32] Being able to affect SMSI in MOFs, a much higher interfacial contact between metal and metal oxide can be achieved due to the nanosized nature of metal oxide SBUs in MOFs. In this particular work, an ordered array of Zr oxide SBUs of the MOF is precisely placed on Cu NC yielding high interfacial contact between Zr oxide SBUs and Cu NC. This interface is active and highly selective for methanol production using CO_2 and H_2 as reactants. Catalytic studies of Cu NCs on various supports and X-ray photoelectron spectroscopy analysis reveal that the presence of SMSI between Zr-oxide clusters of the MOF and Cu NC is responsible for such interesting catalytic property.

Based on the study in Chapter 2, in Chapter 3, the SMSI of metal oxide SBU of the MOF was employed to produce a single site catalyst. It has been a challenge to produce a stable single-site metal catalyst supported on metal oxide during catalysis due to the migration of metal and sintering into large particles. This sintering is typically undesirable because this process decreases the specific surface area of catalytic species. However, such process is rather unlikely in MOFs where metal oxide SBUs are discrete and they are separated by organic linkers. Migration of metal on metal oxide SBUs is limited to the cluster where it resides. By using the defect in UiO-66, single Cu atom is deposited onto the Zr oxide SBU of the MOF that functions as a catalyst for CO oxidation. Cu atom remains single throughout the reaction as indicated by in situ infrared spectroscopy and in situ extended X-ray absorption fine structure spectroscopy.

In Chapter 4, MOF-808, a Zr-based MOF, has been functionalized to produce a catalyst capable of selective oxidation to methanol inspired by particulate methane monooxygenase (pMMO). The availability of exchangeable formate sites that are situated spatially at desired positions allows for the installation of imidazole-based ligands. Metalation with Cu(I) in the presence of O_2 produces the Cu_2O_2 active sites capable of selective oxidation of methane to methanol with 100% selectivity. Ex situ Raman and ex situ X-ray absorption spectroscopic studies provide insight into the structures of the catalysts during the reaction.

Chapter 5 describes the strategies to obtain MOFs with a high density of open metal sites for hydrogen storage application. This is achieved by using MOF-74 series equipped with primary amine for functionalization to install metal binding ligand. Subsequent metalation results in MOFs with high loading of metals. Systematic studies on the effects of metals and their ligands on the hydrogen adsorption isotherm provide insights and a path forward to develop MOFs for hydrogen storage.

1.6 References

(1) Furukawa, H.; Cordova, K. E.; O'Keeffe, M.; Yaghi, O. M., *Science* **2013,** *341*, 1230444.

(2) Li, H.; Eddaoudi, M.; O'Keeffe, M.; Yaghi, O. M., *Nature* **1999,** *402*, 276.

(3) Rungtaweevoranit, B.; Diercks, C. S.; Kalmutzki, M. J.; Yaghi, O. M., *Faraday Discuss.* **2017,** *201*, 9.

(4) Jiang, J.; Zhao, Y.; Yaghi, O. M., *J. Am. Chem. Soc.* **2016,** *138*, 3255.

(5) Rungtaweevoranit, B.; Zhao, Y.; Choi, K. M.; Yaghi, O. M., *Nano Res.* **2016,** *9*, 47.

(6) (a) Sugikawa, K.; Furukawa, Y.; Sada, K., *Chem. Mater.* **2011,** *23*, 3132; (b) He, L.; Liu, Y.; Liu, J.; Xiong, Y.; Zheng, J.; Liu, Y.; Tang, Z., *Angew. Chem. Int. Ed.* **2013,** *52*, 3741; (c) Choi, K. M.; Kim, D.; Rungtaweevoranit, B.; Trickett, C. A.; Barmanbek, J. T. D.; Alshammari, A. S.; Yang, P.; Yaghi, O. M., *J. Am. Chem. Soc.* **2016,** *139*, 356.

(7) Hu, P.; Morabito, J. V.; Tsung, C.-K., *ACS Catal.* **2014,** *4*, 4409.

(8) Li, G.; Kobayashi, H.; Taylor, J. M.; Ikeda, R.; Kubota, Y.; Kato, K.; Takata, M.; Yamamoto, T.; Toh, S.; Matsumura, S., *Nat. Mater.* **2014,** *13*, 802.

(9) Zhao, M.; Deng, K.; He, L.; Liu, Y.; Li, G.; Zhao, H.; Tang, Z., *J. Am. Chem. Soc.* **2014,** *136*, 1738.

(10) Hermes, S.; Schröter, M. K.; Schmid, R.; Khodeir, L.; Muhler, M.; Tissler, A.; Fischer, R. W.; Fischer, R. A., *Angew. Chem. Int. Ed.* **2005,** *44*, 6237.

(11) Hwang, Y. K.; Hong, D. Y.; Chang, J. S.; Jhung, S. H.; Seo, Y. K.; Kim, J.; Vimont, A.; Daturi, M.; Serre, C.; Férey, G., *Angew. Chem. Int. Ed.* **2008,** *47*, 4144.

(12) Tsuruoka, T.; Kawasaki, H.; Nawafune, H.; Akamatsu, K., *ACS Appl. Mater. Interfaces* **2011,** *3*, 3788.

(13) Lu, G.; Li, S.; Guo, Z.; Farha, O. K.; Hauser, B. G.; Qi, X.; Wang, Y.; Wang, X.; Han, S.; Liu, X., *Nat. Chem.* **2012,** *4*, 310.

(14) Choi, K. M.; Na, K.; Somorjai, G. A.; Yaghi, O. M., *J. Am. Chem. Soc.* **2015,** *137*, 7810.

(15) Zhao, M.; Yuan, K.; Wang, Y.; Li, G.; Guo, J.; Gu, L.; Hu, W.; Zhao, H.; Tang, Z., *Nature* **2016,** *539*, 76.

(16) Haruta, M., *Catal. Today* **1997,** *36*, 153.

(17) Tsung, C.-K.; Kuhn, J. N.; Huang, W.; Aliaga, C.; Hung, L.-I.; Somorjai, G. A.; Yang, P., *J. Am. Chem. Soc.* **2009,** *131*, 5816.

(18) Liang, S.; Hao, C.; Shi, Y., *ChemCatChem* **2015,** *7*, 2559.

(19) Qiao, B.; Wang, A.; Yang, X.; Allard, L. F.; Jiang, Z.; Cui, Y.; Liu, J.; Li, J.; Zhang, T., *Nat. Chem.* **2011,** *3*, 634.

(20) Li, Z.; Schweitzer, N. M.; League, A. B.; Bernales, V.; Peters, A. W.; Getsoian, A. B.; Wang, T. C.; Miller, J. T.; Vjunov, A.; Fulton, J. L., *J. Am. Chem. Soc.* **2016,** *138*, 1977.

(21) Lillerud, K. P.; Olsbye, U.; Tilset, M., *Top. Catal.* **2010,** *53*, 859.

(22) Fracaroli, A. M.; Siman, P.; Nagib, D. A.; Suzuki, M.; Furukawa, H.; Toste, F. D.; Yaghi, O. M., *J. Am. Chem. Soc.* **2016,** *138*, 8352.

(23) Rowsell, J. L.; Spencer, E. C.; Eckert, J.; Howard, J. A.; Yaghi, O. M., *Science* **2005,** *309*, 1350.

(24) Chae, H. K.; Siberio-Pérez, D. Y.; Kim, J.; Go, Y.; Eddaoudi, M.; Matzger, A. J.; O'keeffe, M.; Yaghi, O. M., *Nature* **2004,** *427*, 523.

(25) Farha, O. K.; Eryazici, I.; Jeong, N. C.; Hauser, B. G.; Wilmer, C. E.; Sarjeant, A. A.; Snurr, R. Q.; Nguyen, S. T.; Yazaydın, A. O. z. r.; Hupp, J. T., *J. Am. Chem. Soc.* **2012,** *134*, 15016.

(26) Wong-Foy, A. G.; Matzger, A. J.; Yaghi, O. M., *J. Am. Chem. Soc.* **2006,** *128*, 3494.

(27) Rowsell, J. L.; Eckert, J.; Yaghi, O. M., *J. Am. Chem. Soc.* **2005,** *127*, 14904.

(28) Rowsell, J. L.; Yaghi, O. M., *Angew. Chem. Int. Ed.* **2005,** *44*, 4670.

(29) Bhatia, S. K.; Myers, A. L., *Langmuir* **2006,** *22*, 1688.

(30) Tsivion, E.; Long, J. R.; Head-Gordon, M., *J. Am. Chem. Soc.* **2014,** *136*, 17827.

(31) Kapelewski, M. T.; Geier, S. J.; Hudson, M. R.; Stück, D.; Mason, J. A.; Nelson, J. N.; Xiao, D. J.; Hulvey, Z.; Gilmour, E.; FitzGerald, S. A., *J. Am. Chem. Soc.* **2014,** *136*, 12119.

(32) (a) Tauster, S., *Acc. Chem. Res.* **1987,** *20*, 389; (b) Behrens, M.; Studt, F.; Kasatkin, I.; Kühl, S.; Hävecker, M.; Abild-Pedersen, F.; Zander, S.; Girgsdies, F.; Kurr, P.; Kniep, B.-L., *Science* **2012**, 1219831.

Chapter 2

Copper nanocrystals encapsulated in Zr-based metal-organic frameworks for CO_2 hydrogenation to methanol

2.1 Introduction

Typically, metal nanocrystals (NCs) immobilized on supports are employed for gas-phase catalysis due to their high catalytic activities and high specific surface areas.[1] The ability to vary the matrix including size, dimension, and composition at the surface of heterogeneous catalysts is crucial to gain better understandings of the catalyst and thus achieve better catalytic performance.[2] In this context, the effects of size and shape of metal NCs on the catalytic properties have been extensively investigated due to the progress in the synthesis of nanomaterials.[3] However, altering the catalysts interface between metal NCs and support such as metal oxides with similar levels of control remains difficult. We envisaged that the well-defined nature of metal oxide clusters in MOFs can be used to control the interface and allow for a systematic study.

CO_2 hydrogenation to methanol reaction is generally known to be structure sensitive in that the catalytic properties are strongly associated with the dimension and composition of the metal oxide-metal interface.[4] Furthermore, this reaction is an attractive route to recycle the captured CO_2 from fossil fuel combustion sources into a chemical feedstock.[5] Currently, methanol is produced industrially from synthesis gas (a mixture of CO, CO_2, and H_2) using a $Cu/ZnO/Al_2O_3$ catalyst.[6] Therefore, finding catalysts that use CO_2 and H_2 as the only sources to produce methanol selectively is desirable but remains a challenge.[7] For instance, CO has been observed as a by–product from the reverse water–gas shift reaction, *i.e.* $CO_2 + H_2 \rightleftharpoons CO + H_2O$, over $Cu/ZnO/Al_2O_3$ catalyst and newly discovered Ni-Ga heterogeneous catalyst as well.[8] More recently, ‘MnO_x’/mesoporous Co_3O_4 catalyst was used to produce the highest reported yield of methanol under mild temperature and pressure conditions (250 °C, 6 bar).[9] However, these catalysts suffer from lower selectivity as either hydrocarbons and/or CO are also produced along with methanol. Here, we report a catalyst composed of Cu nanocrystal (NC) encapsulated within a metal-organic framework (MOF) for the conversion of CO_2 to methanol with 100% selectivity and high yield.

Specifically, we report a catalyst where Cu NC is encapsulated inside a Zr(IV)-based MOF denoted as $Cu\subset$UiO-66; UiO-66 [$Zr_6O_4(OH)_4(BDC)_6$, BDC = 1,4-benzenedicarboxylate][10] (Scheme 2.1) for CO_2 hydrogenation to methanol. In this construct, an ordered array of Zr oxide SBUs is precisely placed on the Cu surface yielding high interfacial contact between Cu NC and Zr oxide SBUs. Furthermore, these Zr oxide SBUs are spatially spaced by organic linkers ensuring the accessibility of reactants to the active sites. We found that $Cu\subset$UiO-66 shows 8-fold enhanced catalytic activity in comparison to the benchmark $Cu/ZnO/Al_2O_3$ catalyst[11] while maintaining the 100% selectivity towards methanol.

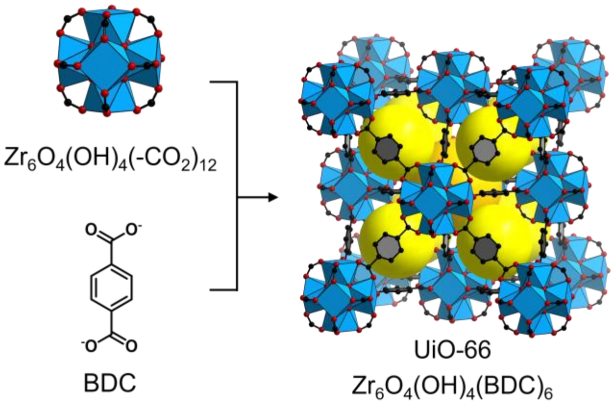

Scheme 2.1. Crystal structure of UiO-66 where Zr oxide SBUs are linked with BDC to form an ordered array of the SBUs. Atom labeling scheme: C, black; O, red; Zr, blue polyhedra. H atoms are omitted for clarity.

2.2 Experimental Section

Chemicals used in this work. All chemicals unless noted were obtained from Sigma-Aldrich. *N*,*N*-dimethylformamide (DMF), acetone, methanol, and acetic acid were obtained from EMD Millipore Chemicals. Copper(II) acetylacetonate and zirconium(IV) *n*-propoxide (70 wt.% in 1-propanol) were obtained from STREM Chemicals. These chemicals were used without further purification. The monoclinic ZrO_2 support and γ-phase Al_2O_3 support were purchased from Alfa Aesar. The purchased ZrO_2 support was used after calcination at 400 °C.

Analytical techniques. Powder X-ray diffraction patterns (PXRD) were recorded using a Bruker D8 Advance diffractometer (Göbel-mirror monochromated Cu Kα radiation $\lambda = 1.54056$ Å). Gas adsorption analyses were performed on a Quantachrome Quadrasorb-SI automatic volumetric gas adsorption analyzer. A liquid nitrogen bath (77 K), ultra-high purity grade N_2 and He (99.999%, Praxair) were used for the measurements. The samples were prepared and measured after evacuating at 120 °C for 12 h. Transmission Electron Microscopy (TEM) samples were prepared by dispersing the samples in acetone using a sonic bath followed by drop casting onto carbon film on copper grids. The images were taken using JEOL JEM-2100 LaB_6 or Philips CM200/FEG both operating at 200 kV. The amounts of Cu in the samples were analyzed by an ICP–AES spectroscope (Optima 7000 DV, Perkin Elmer). The samples were digested in a solution mixture of nitric acid, hydrochloric acid and hydrofluoric acid in 70 °C water bath for an hour. The resulting solutions were diluted with 2 % v/v aqueous nitric solution to 10 mL before the measurement. Solution ^1H NMR spectra of digested samples were acquired on Bruker Avance II 500 MHz spectrometer at 297 K. Elemental microanalyses (EA) were performed in the Microanalytical Laboratory at the College of Chemistry, UC Berkeley using a Perkin Elmer 2400 Series II CHNS elemental analyzer.

Synthesis of Materials:

Cu NCs. In a 50 mL 3-neck round bottom flask, a solution of 32 mg of $Cu(acac)_2$ and 1.3 g of polyvinylpyrrolidone (MW 10,000) in 15 mL of 1,5-pentanediol was heated at 100 °C under dynamic vacuum for 25 min using a heating mantle equipped with a temperature controller. Then the reaction was refilled with N_2 and the reaction temperature was increased rapidly to 180 °C which was then kept constant for 40 min. The synthesized Cu NCs were cooled down naturally, washed with acetone using a centrifuge (8000 rpm, 1 min), rinsed with acetone (5 mL × 2), and dried under N_2 flow for 30 seconds.

Cu$\subset$UiO-66. For MOF precursors solution, DMF (39 mL), terephthalic acid (50 mg, 0.300 mmol), acetic acid (7.25 mL), and $Zr(OPr)_4$ (128.4 μL, 0.286 mmol) were added sequentially into a 100 mL round bottom flask which was then sealed with a septum. The solution was degassed by bubbling with N_2 for 15 min while stirring gently. For Cu NCs solution, freshly synthesized Cu NCs described above were redispersed in degassed DMF (10 mL). The solution of Cu NCs was degassed for another 5 min and 2 mL of Cu NCs solution was injected into the MOF precursor solution. The flask was placed in a 65 °C isothermal oven for 15 h. After heating, the pink suspension was transferred to a N_2 filled 50 mL centrifuge tube via cannula transfer under N_2. The supernatant was discarded under N_2 and the resulting solid was redispersed in degassed acetonitrile (5 mL). This suspension was lyophilized for 48 h. Lyophilized sample was immersed in degassed DMF (10 mL × 3) over 24 h period and in degassed acetone (10 mL × 3) over 24 h period. Finally, the suspension was centrifuged to remove the supernatant and the solid was dried under dynamic vacuum overnight at room temperature.

Cu$\subset$ZIF-8. The synthesis was performed according to the reported procedure with some modifications.[12] Freshly synthesized Cu NCs as described above were dispersed in degassed methanol (10 mL) and the solution was degassed for another 5 min. In a N_2 filled 20 mL scintillation vial capped with a septum, 9 mL of 2-methylimidazole dissolved in methanol (25 mM), 1 mL of Cu NCs solution, and 9 mL of $Zn(NO_3)_2 \cdot 6H_2O$ (25 mM) were added. The vial was left undisturbed overnight at room temperature. The suspension was collected using a centrifuge under air-free conditions and immersed in degassed MeOH (5 mL × 3) over 24 h period. Finally, the suspension was centrifuged to remove the supernatant and the solid was dried under dynamic vacuum overnight at room temperature.

UiO-66. Acetic acid (1.375 mL) and $Zr(OPr)_4$ (64.2 μL, 0.143 mmol) were added sequentially to a 20 mL scintillation vial containing terephthalic acid (25 mg, 0.150 mmol) dissolved in DMF (9.75 mL). The vial was sealed and placed in a 50 °C isothermal oven overnight. UiO-66 was collected using a centrifuge (8,000 rpm, 5 min), immersed in DMF (5 mL × 3) over 24 h period and in acetone (5 mL × 3) over another 24 h period. Finally, UiO-66 was dried under dynamic vacuum overnight at room temperature.

MIL-101 (Cr). Terephthalic acid (2.08 g, 12.5 mmol) and $Cr(NO_3)_3 \cdot 9H_2O$ (5.00 g, 12.5 mmol) were stirred in 50 mL deionized water at room temperature for 20 min. The resulting mixture was transferred to a 100 mL Teflon-lined autoclave bomb and was heated at 220 °C for 18 h. After slowly cooled down to room temperature, the green precipitate was collected using a centrifuge (5,000 rpm, 8 min), immersed in deionized water (50 mL × 12) over 3 days period and in ethanol (50 mL × 12) over 3 days period. Finally, MIL-101 (Cr) was dried under dynamic vacuum at room temperature for 24 hours followed by the evacuation at 150 °C for 24 hours.

Mesoporous MCF-26. The synthesis was conducted according to the reported procedure.[13] 4 g of triblock copolymer Pluronic P123 were dissolved in a 10 ml of 37% HCl and 65 ml of H_2O. 5 g of 1,3,5-trimethylbenzene (TMB) was added, and the resulting solution was heated to 40 °C with vigorous stirring for 2 h. A total of 9.2 mL of tetraethoxysilane (TEOS) was then added and stirred for 5 min. The solution was transferred to an autoclave and aged at 40 °C for 20 h under a quiescent condition. A total of 46 mg of NH_4F was added, and the mixture was aged at 140 °C for another 24 h. The resulting precipitate was filtered, washed with water and ethanol, and dried. The white powder obtained was calcined in air at 550 °C for 6 h.

Cu/ZnO/Al_2O_3 catalyst. The synthesis was performed by co-precipitation method according to the reported procedure with some modifications.[14] 30 ml of a 1 M aqueous solution of Cu and Zn and Al nitrates (60:30:10 atomic ratio) was added dropwise (2 ml/min) using a syringe pump to 50 ml of deionized water (pH kept at 7 with Na_2CO_3) under 65 °C silicone oil bath. Simultaneously, 1.5 M Na_2CO_3 solution was added in dropwise in order to keep the pH at 7 ± 0.1. The obtained precipitate was aged for 2 h at 65 °C in the mother liquor under vigorous stirring. The precipitate was filtered, washed with water, dried at 70 °C oven, and calcined at 330 °C in an air furnace.

General procedure for immobilization. Cu on UiO-66, Cu on MIL-101 (Cr), Cu on MCF-26, Cu on ZrO_2 and Cu on Al_2O_3: Freshly prepared Cu NCs (0.78 mg/mL) dispersed in 10 mL EtOH were sonicated with the desired support (390 mg) suspended in ethanol under sonication for 1 h. The resulting catalysts were washed with ethanol three times using a centrifuge (8,000 rpm, 5 min) to ensure complete removal of unimmobilized Cu NCs.

Catalysis:

The catalytic testing was performed using custom-designed continuous flow tubular reactor including back pressure regulator (Parr Instrument Co.). Mass flow controllers were calibrated using ADM 1000 flow meter (Agilent Technologies) and ultrahigh purity He, H_2 (99.999%, Praxair), and CO_2 (4.8 RS, Praxair) were flowed into the 30 cm long quarter inch 316 stainless steel reactor. Catalysts (0.1–0.4 g) were used depending on the concentration of Cu NC after sieving in the range of 100-250 μm. The catalyst was placed in the middle of the reactor tube, delimited by a layer of purified glass wool and a layer of quartz sand (50-70 mesh) at each end. Pretreatment of catalysts was conducted under 30 sccm He at 250 °C (3 °C/min) for 1 h and cooled down to 50 °C under He flow. For the reduction of catalysts, we change gas to 100% H_2 flow (30 sccm) and ramp up to 250 °C (3 °C/min) and hold it for 2 h. After cooling down to 50 °C, the reactor cell was flowed 7 sccm CO_2 and 21 sccm H_2 and pressurized to 10 bar. After stabilization, the reaction temperature was increased to 175-250 °C (3 °C/min) and after 3 min when the reaction temperature reached to set reaction temperature, the outstream was analyzed by gas chromatograph (Model: GC-2014, Shimadzu Co.). The measurement time is 56 min per GC program and we use GC data after 2nd measurement (~1 h). The reactants and products were separated using connected Hayesep D, SP-2100, and 5 Å molecular sieve column. The CO_2 and CO were monitored using a thermal conductivity detector and methanol was monitored using a flame ionization detector. The number of active Cu surface was determined using N_2O titration, in which a stoichiometry of 2Cu:1N_2O corresponding to the reaction $2Cu + N_2O(g) \rightarrow Cu_2O + N_2(g)$. The catalyst was reduced under 100% H_2 for 2 h and cooldown to room temperature and then backfilled with He. The analysis was performed at room temperature by flowing 3% N_2O/He over the reduced catalyst and observing the corresponding increase in N_2 concentration on the thermal conductivity detector. The integration area was used to determine the number of Cu active site.

X-ray photoelectron spectroscopy analysis (XPS):

Chemical characterization of the catalyst was performed using an ultra-high vacuum (UHV) PHI 5400 X-ray photoelectron spectroscopy (XPS) system with a non-monochromatic Al X-ray source ($K\alpha$=1486.7 eV) operated at 350 W power. Survey XPS spectra were obtained with analyzer pass energy of 178.5 eV and step size of 1 eV. High-resolution spectra of Cu 2p and Zr 3d regions were obtained with analyzer pass energy of 35 eV and 0.05 eV energy steps. The binding energy scale was corrected setting C 1s peak in 284.6 eV. The peak fitting was performed using Casa XPS software. Binding energy values for the Zr 3d were obtained by fitting this region using two spin-orbit components (Δ=2.4eV). The values for XPS binding energy were referenced by NIST XPS database (http://srdata.nist.gov/xps/).

2.3 Results and Discussion

Synthesis of Cu NCs. Typical procedures for the encapsulation of metal NCs inside MOFs involve the addition of metal NCs into the solution of MOF precursors. Such metal NCs must be colloidally stable in the MOF precursors solution and function as a nucleation site for the MOF growth for successful encapsulation. Polyvinylpyrrolidone (PVP) has been shown to be a suitable capping agent for the encapsulation of metal NCs in MOFs. Although a wide variety of synthetic procedures exist for the synthesis metal NCs capped with PVP for other noble metals, reproducible synthesis of Cu NCs capped with PVP did not exist. Thus, the synthesis procedure of Cu NCs was developed in this project using a polyol process where Cu salt and PVP were dissolved in polyol solvent. Various parameters were optimized including Cu precursors [$Cu(acac)_2$, $Cu(NO_3)\cdot 2.5H_2O$, $Cu(OAc)_2$ and Cu(OAc)], polyol solvents [1,5-pentanediol, triethylene glycol, ethylene glycol], PVP molecular weight [10K, 29K, 55K], concentration of each components and reaction temperature profile. It was found that the combination of $Cu(acac)_2$ with 10K PVP using 1,5-pentanediol at solvent heated up to 180 °C gave Cu NCs of 18 nm in diameter suitable for the encapsulation and catalytic studies (Figure 2.1). Cu NCs synthesized by this method were used throughout this study. This permitted us to systematically study the change in the catalytic properties as a function of various MOFs and other supports.

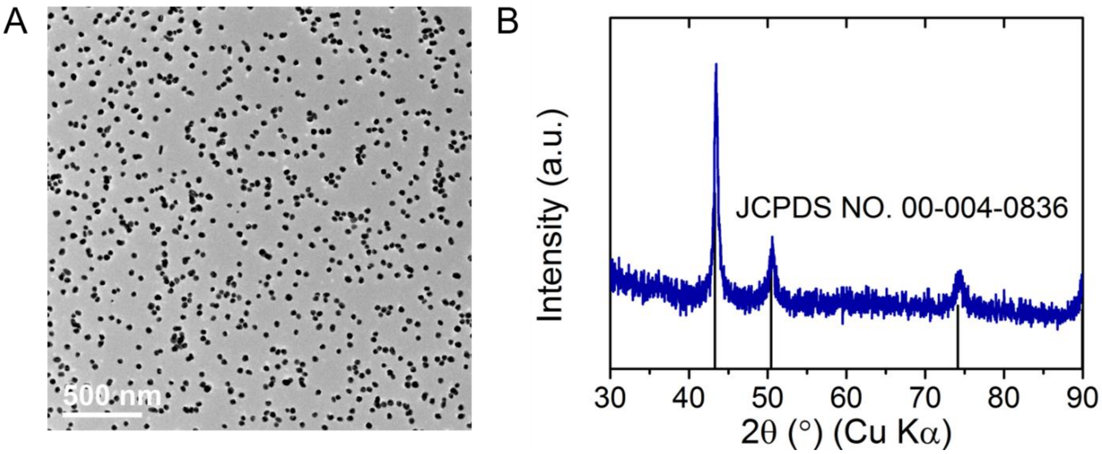

Figure 2.1. (A) TEM image of Cu NCs, and (B) PXRD of Cu NCs overlaid with diffraction lines of Cu.

Synthesis and Characterization of Cu NC within (Cu⊂UiO-66) and on UiO-66 (Cu on UiO-66). The selection of capping ligands is also important in order to control the growth of MOFs on the metal NCs. Capping ligands are molecules or polymers that stabilize the metal NCs to prevent particle aggregation. The functional groups presented in the capping ligands can also be used to control the growth of MOFs. In order for MOFs to grow on the surface of the metal NCs, the selected capping ligand on the surface of the metal NCs must contain reactive sites that can be used for MOF nucleation. If this surface nucleation does not happen, MOFs will nucleate in the solution generating non-encapsulated metal NCs.

For Cu⊂UiO-66, the pre-synthesized Cu NCs were added to the solution containing the MOF precursors. In addition to the exclusion of oxygen to prevent the surface oxidation and subsequent acid-mediated dissolution of Cu NCs,[15] we observed that the choice of metal precursors dramatically affected the encapsulation process. Typical Zr precursors for the synthesis of UiO-66 are $ZrOCl_2 \cdot 8H_2O$ and $ZrCl_4$, which led to the dissolution of Cu NCs.[16] We found that the use of $Zr(OPr^n)_4$ led to the successful production of Cu⊂UiO-66 as single Cu inside single nanocrystalline UiO-66 (Figure 2.2A). This material is the first example of Cu NCs being encapsulated inside the framework as a well-defined construct.[17]

For Cu NCs immobilized on UiO-66 (Cu on UiO-66), we deposited Cu NCs on the pre-synthesized UiO-66 by mixing colloidal solutions of Cu NCs and UiO-66 where UiO-66 was prepared using $Zr(OPr^n)_4$ as well (Figure 2.2B).

The catalysts were further characterized by powder X-ray diffraction (PXRD), N_2 adsorption-desorption isotherms, and inductively coupled plasma atomic emission spectroscopy (ICP-AES). The Cu NC-MOF constructs display diffraction lines that coincide with the simulated patterns confirming the crystallinity and identity of the materials (Figure 2.2C). N_2 adsorption isotherms show that all the materials are porous (Figure 2.2D) and ICP-AES measurements indicate 1 wt.% and 1.4 wt.% of Cu for Cu⊂UiO-66 and Cu on UiO-66, respectively.

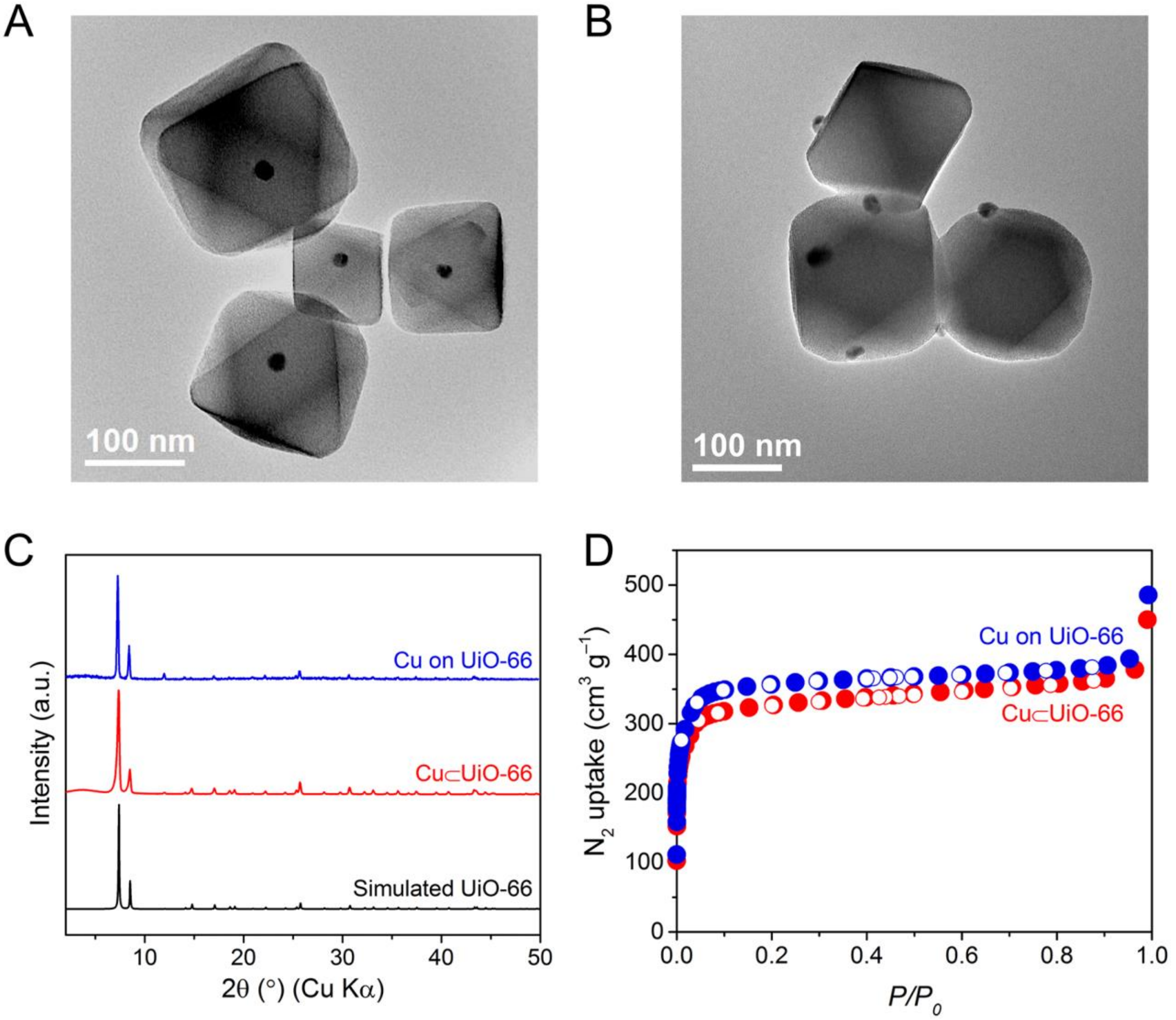

Figure 2.2. Characterization of Cu decorated MOFs: TEM images of (A) Cu⊂UiO-66 (single Cu NC inside UiO-66), (B) Cu on UiO-66, (C) experimental PXRD patterns in comparison with simulated pattern from single crystal X-ray diffraction data, and (D) N_2 adsorption-desorption isotherms at 77 K with adsorption and desorption points represented by closed circles and open circles, respectively ($P/P_\circ$, relative pressure).

CO_2 Hydrogenation to Methanol. We first study the catalytic properties of Cu NCs integrated with various MOFs and conventional supports. We tested three MOFs with different SBUs namely UiO-66 with a Zr oxide SBU, MIL-101 (Cr) [$Cr_3O(H_2O)_2(BDC)_3(OH)$] with a Cr oxide SBU,[18] and ZIF-8 [$Zn(C_4H_5N_2)_2$] with a Zn-N SBU (Figure 2.3).[19] We also tested Cu NCs supported on traditional supports, mesoporous silica (MCF-26), ZrO_2, and Al_2O_3, as they are commonly known to be either inert or active supports for this reaction. For comparison, industrial Cu/ZnO/Al_2O_3 catalyst was used as a benchmark reference and tested under the same reaction condition.

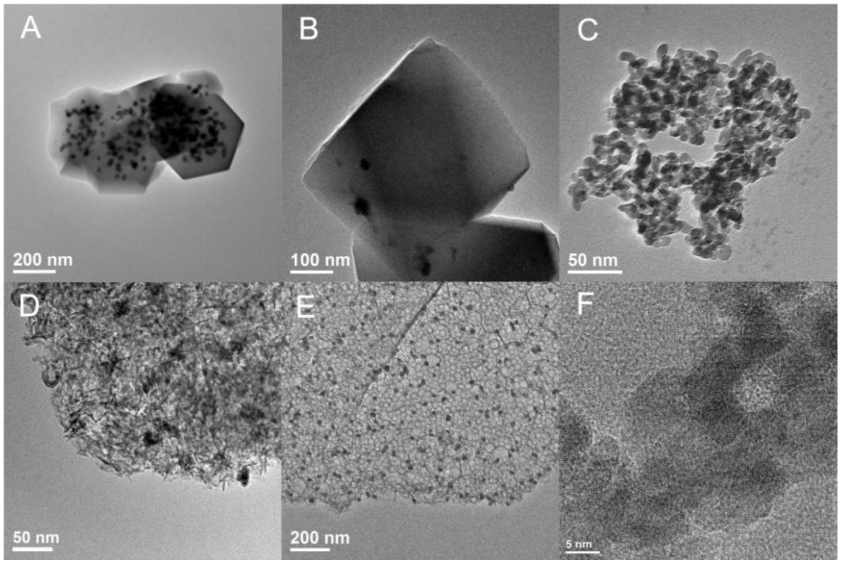

Figure 2.3. TEM images of (A) Cu⊂ZIF-8, (B) Cu on MIL-101 (Cr), (C) Cu on ZrO_2, (D) Cu on Al_2O_3, (E) Cu on MCF-26, and (F) $Cu/ZnO/Al_2O_3$.

CO_2 hydrogenation at 175 °C and 10 bar using CO_2 and H_2 in a 1:3 molar ratio revealed that only Cu⊂UiO-66, Cu on UiO-66, Cu on ZrO_2, and $Cu/ZnO/Al_2O_3$ can convert CO_2 to methanol with initial turnover frequencies (TOF) of methanol formation of 3.7×10^{-3} s^{-1}, 1.7×10^{-3} s^{-1}, 0.42×10^{-3} s^{-1}, and 0.45×10^{-3} s^{-1}, respectively. Neither Cu NCs on MIL-101 (Cr) nor Cu NCs⊂ZIF-8 showed catalytic activity. This result indicates that only the materials containing Zr oxide or Zn oxide in either cluster or nanocrystal form can catalyze CO_2 hydrogenation to methanol. Furthermore, it is remarkable that Zr oxide SBUs of UiO-66 can function as ZrO_2 or even better in promoting Cu catalyst.

The difference in catalytic activity can be attributed to the variations in the composition of the SBUs and not from variations in the structural stability. We examined the structural integrity of the MOF-based catalysts after the reaction by TEM, PXRD, and N_2 adsorption-desorption measurement. The crystallinity and porosity of UiO-66, MIL-101 (Cr), and ZIF-8 were preserved throughout the reaction. From the elemental analysis (EA), ^1H NMR, and TGA measurement results, we do not observe coking deposited inside the catalysts

Figure 2.4 displays the initial yield rates of Cu⊂UiO-66 in comparison with Cu on UiO-66 catalyst. By comparing the catalytic activity between Cu⊂UiO-66 and Cu on UiO-66, we find that the location of the Cu NC also influences the catalytic activity. Cu⊂UiO-66 catalyst shows a 2-fold increase and much-enhanced stability in activity presumably due to the higher number of contact points between the Zr oxide SBU and Cu surface and the confinement of the Cu NC in the MOF.[20] This result implies that the Cu NC environment surrounded by the Zr oxide SBU can help in creating active Cu sites for catalytic conversion of CO_2 to methanol.

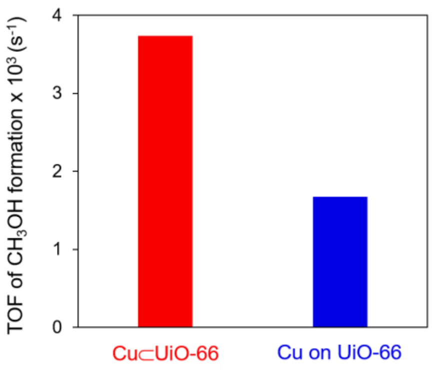

Figure 2.4. Initial TOF of methanol formation over Cu⊂UiO-66 and Cu on UiO-66. The reaction rates measured after 1 h. Reaction condition: 7 sccm of CO_2, 21 sccm of H_2, 10 bar, and 175 °C.

We increased the reaction temperature to 200 °C, 225 °C, and 250 °C at 10 bar to observe the thermodynamic effect under low conversion (below diffusion limit). As the CO_2 hydrogenation to methanol is an exothermic reaction ($CO_2 + 3H_2 \rightleftharpoons CH_3OH + H_2O$, $\Delta H^o = -49.4$ kJ mol^{-1}) whereas the reverse water gas shift reaction is endothermic ($CO_2 + H_2 \rightleftharpoons CO + H_2O$, $\Delta H^o = +41.2$ kJ mol^{-1}), CO production is favored at higher temperatures.[21] Figure 2.5 indicates the initial methanol yield rate at four different reaction temperatures for Cu⊂UiO-66 and $Cu/ZnO/Al_2O_3$. As the reaction temperature increases, the CO yield rate steeply increases in the industrial $Cu/ZnO/Al_2O_3$ catalyst [selectivity for CO = 0% (175 °C), 33% (200 °C), 42% (225 °C), and 61% (250 °C)]. Interestingly, no CO was detected in the Cu⊂UiO-66 catalyst at all reaction temperatures. This high methanol selectivity of Cu⊂UiO-66 is not due to the low CO_2 conversion but the intrinsic property of the catalyst because Cu⊂UiO-66 and $Cu/ZnO/Al_2O_3$ show similar conversion (~5%) at 200 °C.

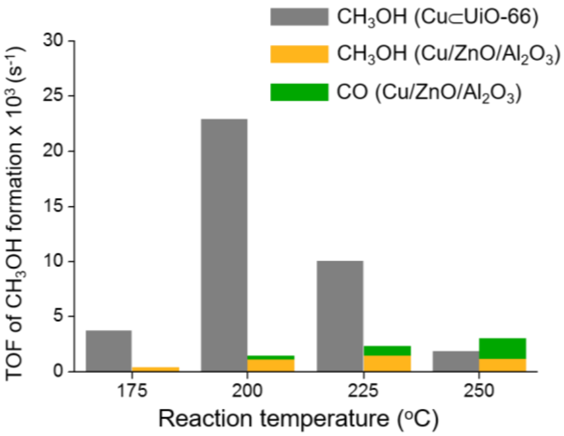

Figure 2.5. TOFs of product formation over Cu⊂UiO-66 catalyst and $Cu/ZnO/Al_2O_3$ catalyst as various reaction temperatures. No CO is produced in the case of Cu⊂UiO-66 under all reaction temperatures.

At four different reaction temperatures, the initial methanol yield rates of Cu⊂UiO-66 always outperforms Cu/ZnO/Al_2O_3. We found that the optimal reaction temperature for Cu⊂UiO-66 is 175 °C as it shows stable catalytic activity. At this reaction temperature, Cu⊂UiO-66 exhibits 8–fold enhancement of catalytic activity in comparison to Cu/ZnO/Al_2O_3.

X-ray photoelectron spectroscopy (XPS) Analysis. To understand the origin of high activity and high selectivity of Cu⊂UiO-66, we performed XPS analysis to probe the electronic properties of the catalyst. However, the distance between Cu NC and the surface of the Cu⊂UiO-66 crystal is beyond the mean free path of escaped electrons generated from X-ray used in XPS.[22] We then turned to investigate Cu on UiO-66 and used it as a proxy for Cu⊂UiO-66. We believe this is reasonable because Cu on UiO-66 also shows 100% selectivity for methanol and comparable activity and therefore most likely have the same active catalyst interface.

Despite the use of as-synthesized Cu on UiO-66 catalyst, Cu was readily oxidized under ambient condition, the surface oxidation state of the Cu NC is Cu(II) as shown by the 934 eV binding energy in the XPS Cu 2p spectrum.[22] This is presumably due to surface oxidation of Cu NCs to form a Cu/Cu_2O/CuO structure as reported previously.[23] The Zr $3d_{5/2}$ spectrum in UiO-66 without Cu exhibits binding energy of 182.8 eV which corresponds to the Zr(IV) oxidation state in the Zr oxide SBU $[Zr_6O_4(OH)_4(\text{-}CO_2)_{12}]$.[24] In the case of the Zr 3d spectrum of Cu on UiO-66 catalyst, Zr $3d_{5/2}$ peak shift from 182.8 eV to 182.2 eV is observed, highlighting that the Zr(IV) is reduced when in contact with the Cu NCs (Figure 2.6A).[25] The fact that Zr (IV) in UiO-66 is reduced implies that Cu is oxidized inherently.

These changes in oxidation state suggest the interaction between Cu NC and Zr oxide SBU, also known as a strong metal-support interaction effect. Considering this effect, Cu NC in contact with UiO-66 would result in the combination of metallic Cu and Cu cation species even after the reduction. The combination of Cu species positively affects the reaction because each species cooperatively play a role during the catalysis: (i) hydrogen dissociation by metallic Cu species,[6] and (ii) stabilization of the intermediates (*i.e.* formate) by cationic Cu species.[7c] It is generally accepted that dissociation of the hydrogen molecule is fast and hydrogenation of surface formate is the rate-determining step.[26] Thus, the presence of copper cationic species after reduction is necessary. Based on these observations, we postulate that the active site for the Cu NC-UiO-66 catalyst is the interface between Cu NC and Zr oxide SBU $[Zr_6O_4(OH)_4(\text{-}CO_2)_{12}]$ (Figure 2.6B).

In contrast to the previous report on Cu/ZrO_2 where Zr $3d_{5/2}$ peak shift was not detected despite the presence of the interaction between Cu and ZrO_2, the peak shift of Zr oxide SBU observed here suggests the higher interfacial contact area between Zr oxide SBU and Cu NC.[27] This effect can be attributed to the nanosized metal oxide SBU in the MOF backbone.

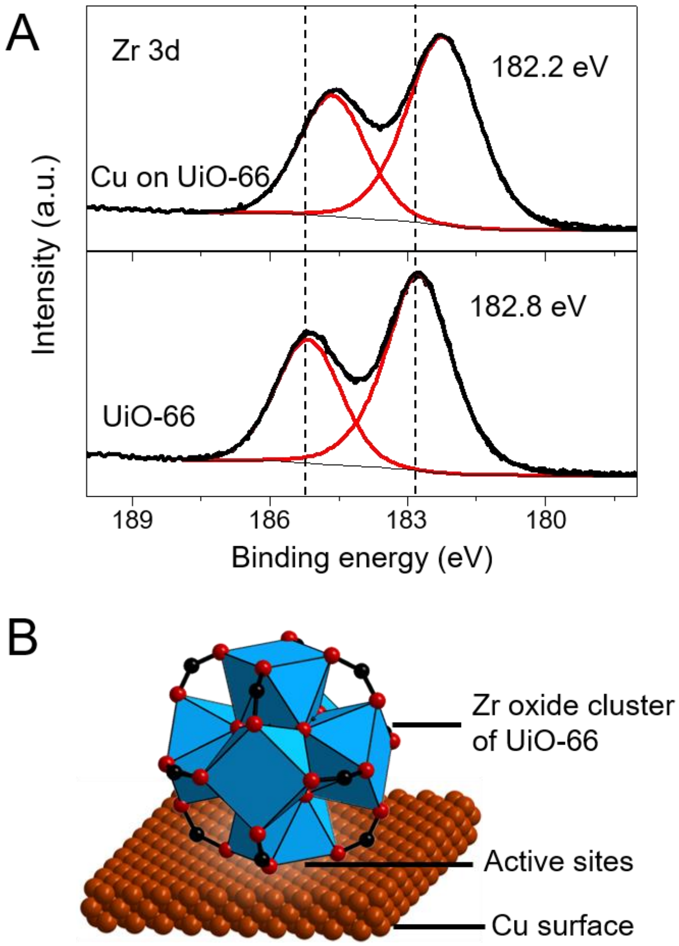

Figure 2.6. (A) XPS Zr 3d spectra of UiO-66 and Cu on UiO-66. (B) Illustration of the active site of Cu NC-UiO-66 catalyst. One Zr oxide SBU $[Zr_6O_4(OH)_4(\text{-}CO_2)_{12}]$ is used as a representative of ordered array of SBUs. Atom labeling scheme: Cu, brown; C, black; O, red; Zr, blue polyhedra. H atoms are omitted for clarity.

2.4 Conclusion

The support effect on the Cu catalyst for the CO_2 hydrogenation to methanol was investigated over different types of MOFs [UiO-66, MIL-101 (Cr), and ZIF-8], mesoporous silica (MCF-26), ZrO_2, and Al_2O_3. We found that UiO-66 is the best promoter for Cu catalyst giving high selectivity and high yield for the production of methanol from CO_2. From XPS analysis and catalytic experiments, we believe that the presence of the combination of multiple Cu oxidation states and the higher interfacial contact area between Cu NCs and Zr oxide SBUs of the MOF lead to the high TOF for methanol. To our knowledge, this is the first finding that metal oxide clusters (SBU) in MOF can have strong-metal support interaction as typically observed in bulk metal oxides.

2.5 Appendices

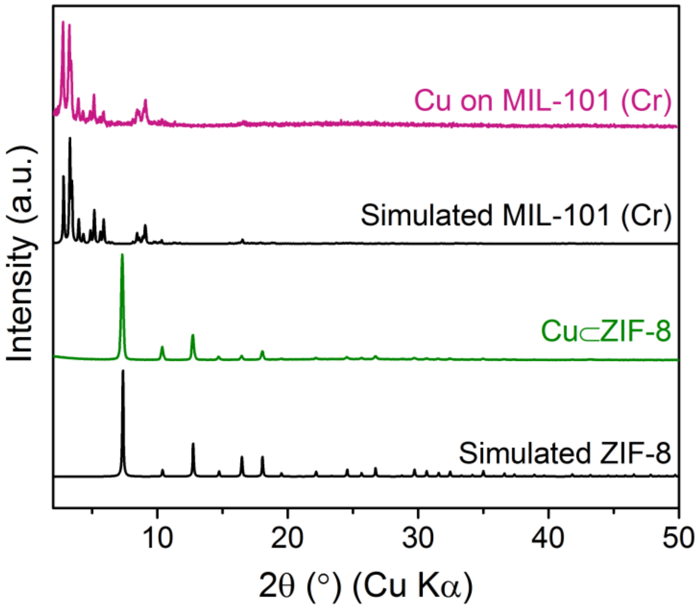

Figure A2.1. PXRD patterns of the Cu NC-MOF catalysts in comparison with their respective simulated patterns.

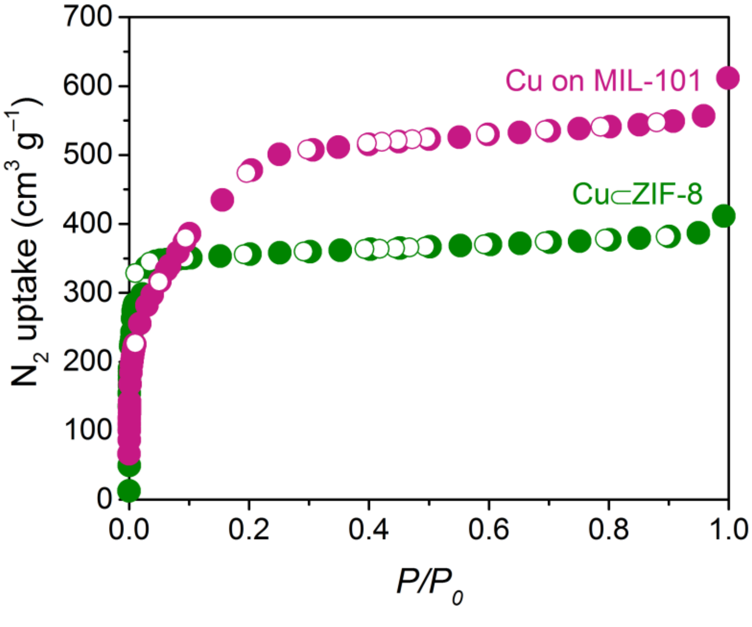

Figure A2.2. N_2 adsorption-desorption isotherms of Cu NC-MOF catalysts at 77 K with adsorption and desorption points represented by closed circles and open circles, respectively.

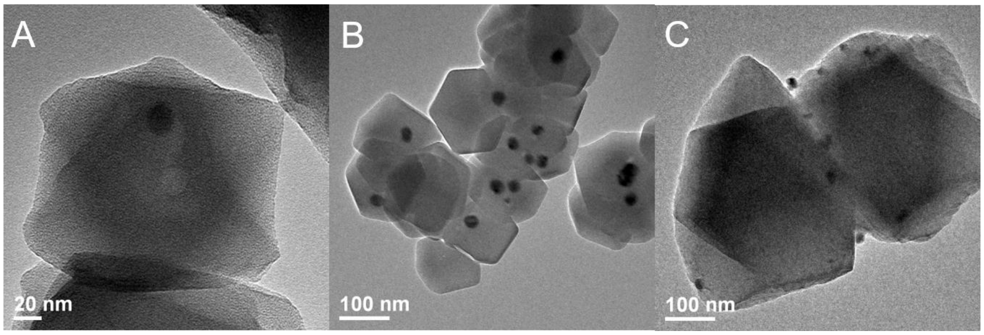

Figure A2.3. Characterization of Cu NC-MOF catalysts after reaction (reaction conditions: 7 sccm of CO_2, 21 sccm of H_2, 10 bar, and 175 °C): TEM images of (A) Cu⊂UiO-66, (B) Cu⊂ZIF-8, and (C) Cu on MIL-101 (Cr).

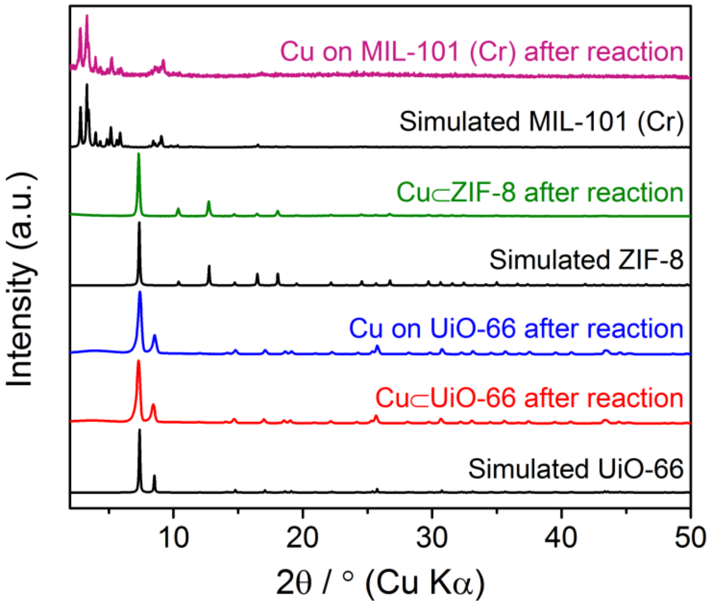

Figure A2.4. PXRD patterns of the Cu NC-MOF catalysts after the reactions (reaction conditions: 7 sccm of CO_2, 21 sccm of H_2, 10 bar, and 175 °C) in comparison with their respective simulated patterns.

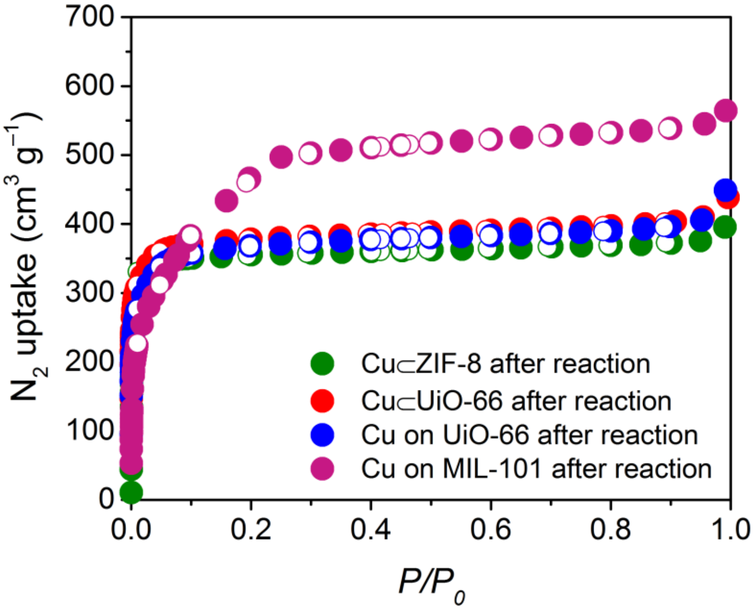

Figure A2.5. N_2 adsorption-desoprtion isotherms at 77 K of Cu NC-MOF catalysts after the reactions (reaction conditions: 7 sccm of CO_2, 21 sccm of H_2, 10 bar, and 175 °C) with adsorption and desorption points represented by closed circles and open circles, respectively.

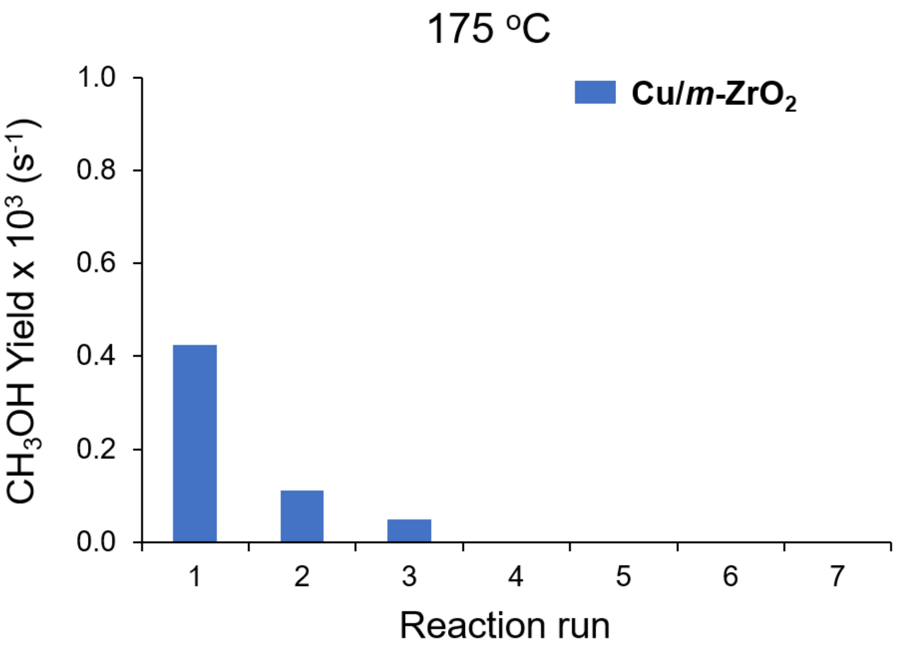

Figure A2.6. Time on stream methanol yield rate over Cu on ZrO_2. It takes 56 min per reaction run. Reaction conditions: 7 sccm of CO_2, 21 sccm of H_2, 10 bar, and 175 °C.

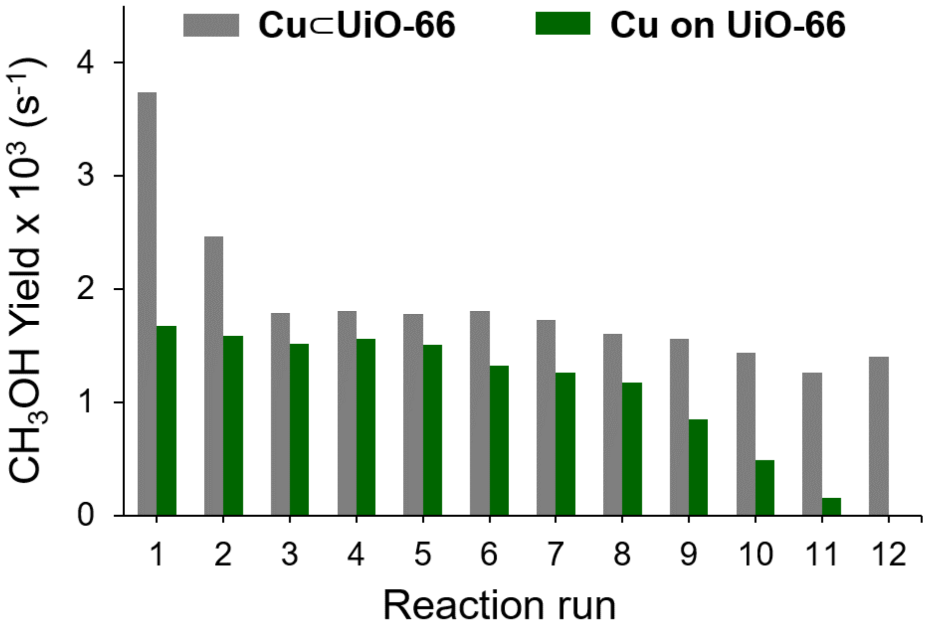

Figure A2.7. Time on stream methanol yield rate over Cu⊂UiO-66 in comparison with Cu on UiO-66. It takes 56 min per reaction run. Reaction conditions: 7 sccm of CO_2, 21 sccm of H_2, 10 bar, and 175 °C.

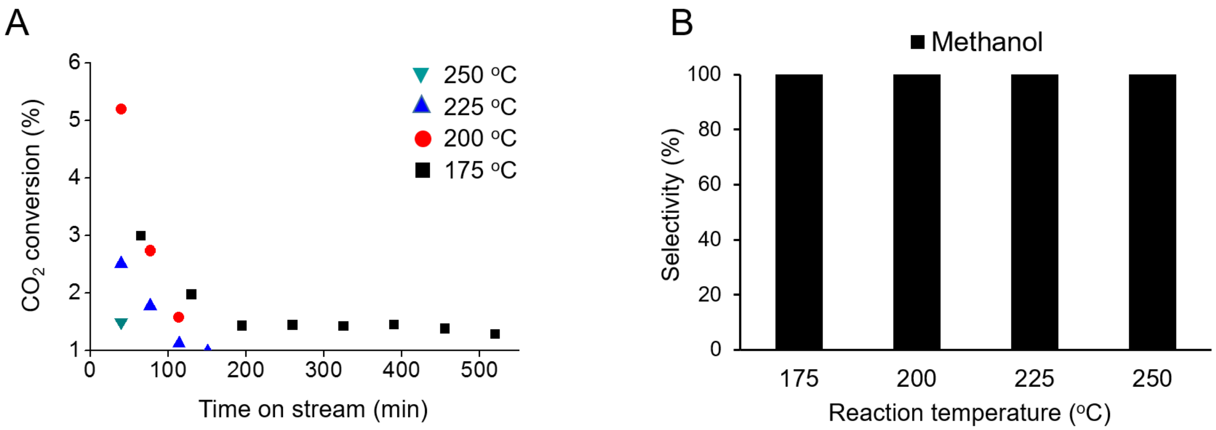

Figure A2.8. (A) Time on stream CO_2 conversion and (B) selectivity over Cu⊂UiO-66 catalyst at 175 °C, 200 °C, 225 °C, and 250 °C. Reaction conditions: 7 sccm of CO_2, 21 sccm of H_2, and 10 bar.

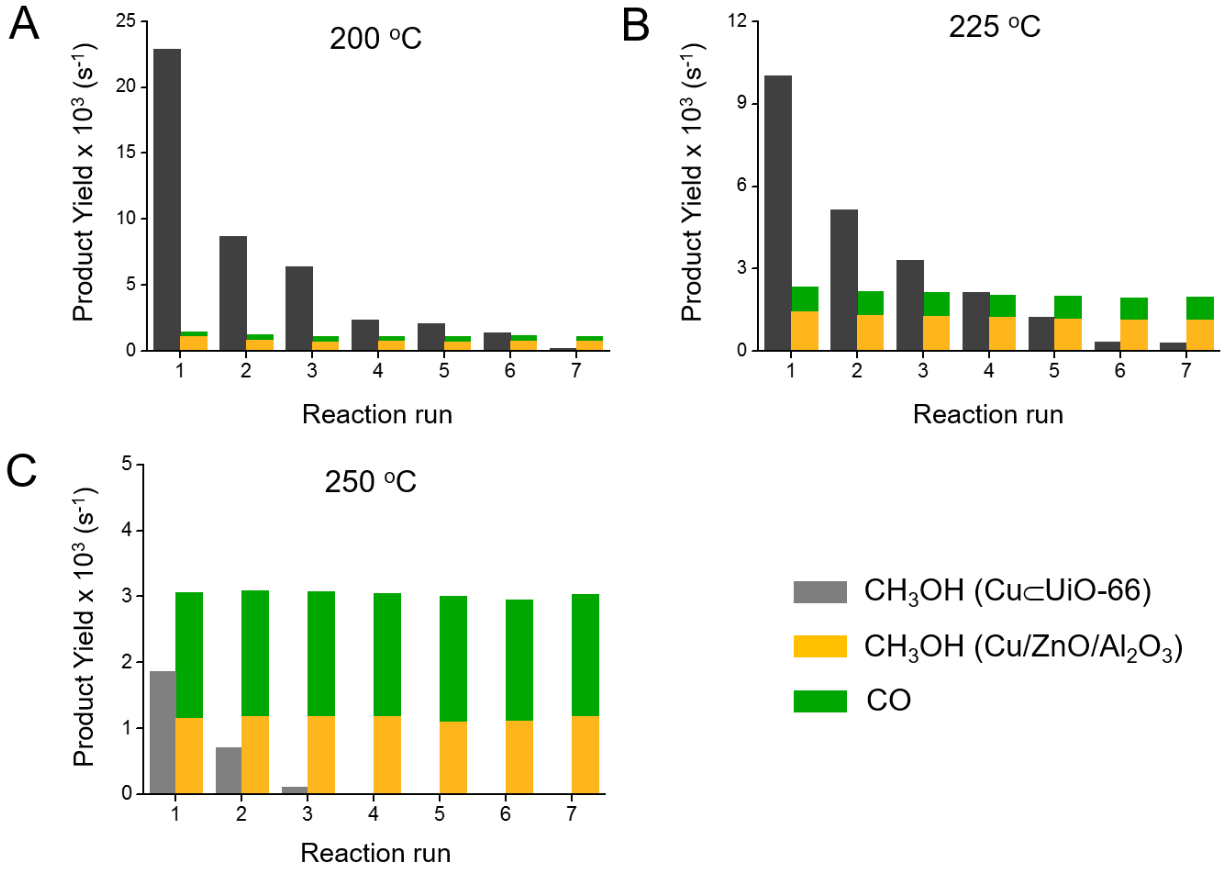

Figure A2.9. Time on stream product yield rate over Cu⊂UiO-66 catalyst in comparison with industrial Cu/ZnO/Al_2O_3 catalyst at (A) 200 °C, (B) 225 °C, and (C) 250 °C. It takes 56 min per reaction run. Reaction conditions: 7 sccm of CO_2, 21 sccm of H_2, and 10 bar.

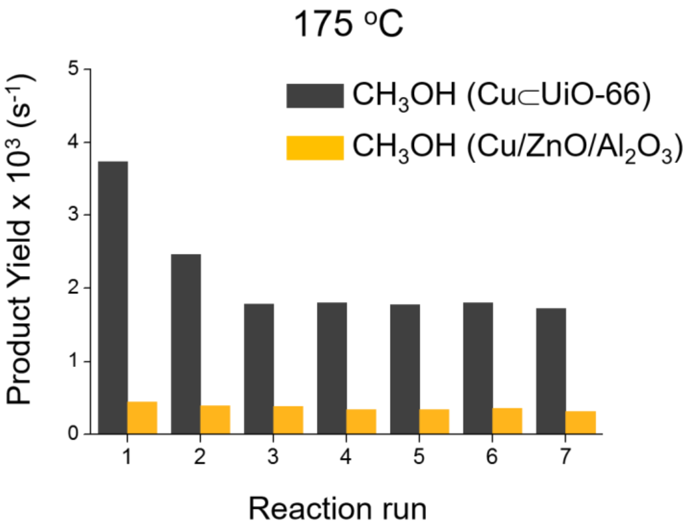

Figure A2.10. Time on stream product yield rate over Cu⊂UiO-66 catalyst in comparison with industrial Cu/ZnO/Al_2O_3 catalyst at 175 °C. It takes 56 min per reaction run. Reaction conditions: 7 sccm of CO_2, 21 sccm of H_2, and 10 bar.

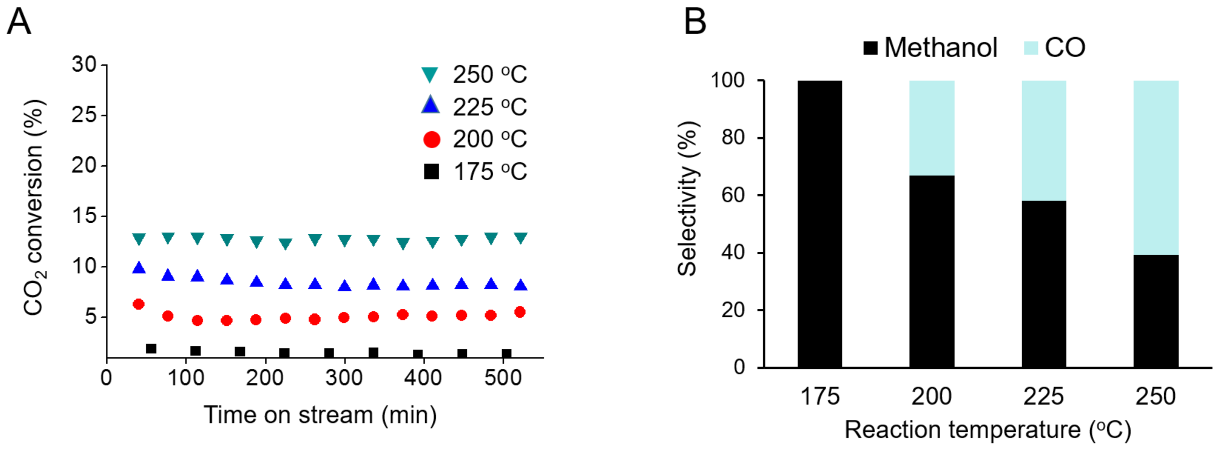

Figure A2.11. (A) Time on stream CO_2 conversion and (B) selectivity over Cu/ZnO/Al_2O_3 catalyst at 175 °C, 200 °C, 225 °C, and 250 °C. Reaction conditions: 7 sccm of CO_2, 21 sccm of H_2, and 10 bar.

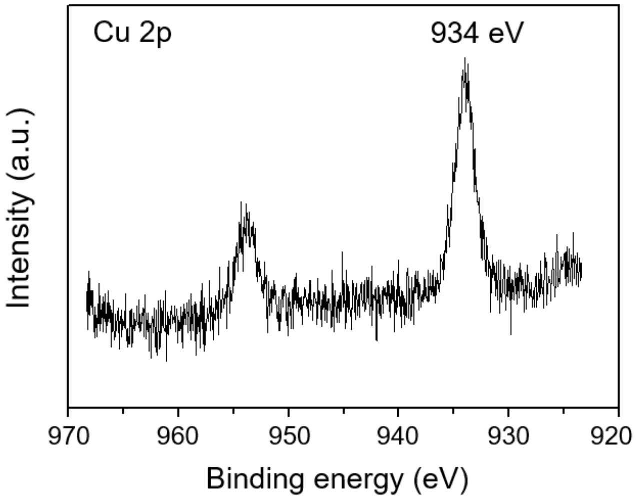

Figure A2.12. XPS Cu 2p spectrum of Cu on UiO-66.

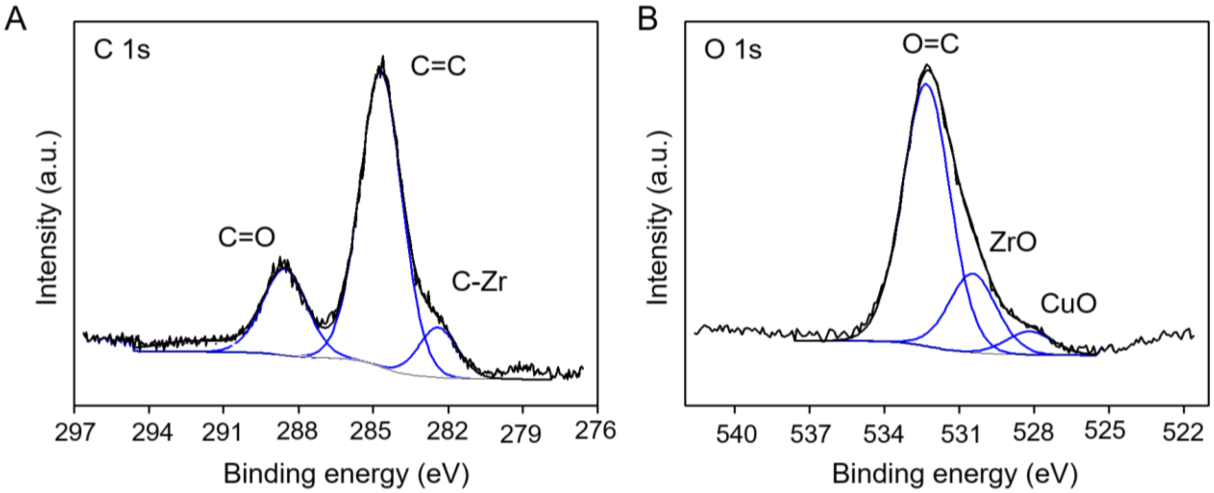

Figure A.2.13. XPS spectra of Cu on UiO-66 catalyst on (A) C 1s and (B) O 1s.

2.6 References

(1) Rothenberg, G., *Catalysis: concepts and green applications*. John Wiley & Sons: 2017.

(2) (a) Ye, R.; Hurlburt, T. J.; Sabyrov, K.; Alayoglu, S.; Somorjai, G. A., *Proc. Natl. Acad. Sci. U.S.A.* **2016,** *113*, 5159; (b) Iablokov, V.; Beaumont, S. K.; Alayoglu, S.; Pushkarev, V. V.; Specht, C.; Gao, J.; Alivisatos, A. P.; Kruse, N.; Somorjai, G. A., *Nano Lett.* **2012,** *12*, 3091; (c) Joo, S. H.; Park, J. Y.; Renzas, J. R.; Butcher, D. R.; Huang, W.; Somorjai, G. A., *Nano Lett.* **2010,** *10*, 2709.

(3) An, K.; Somorjai, G. A., *ChemCatChem* **2012,** *4*, 1512.

(4) Grabow, L.; Mavrikakis, M., *ACS Catal.* **2011,** *1*, 365.

(5) (a) Schoedel, A.; Ji, Z.; Yaghi, O. M., *Nat. Energy* **2016,** *1*, 16034; (b) Goeppert, A.; Czaun, M.; Jones, J.-P.; Prakash, G. S.; Olah, G. A., *Chem. Soc. Rev.* **2014,** *43*, 7995.

(6) Behrens, M.; Studt, F.; Kasatkin, I.; Kühl, S.; Hävecker, M.; Abild-Pedersen, F.; Zander, S.; Girgsdies, F.; Kurr, P.; Kniep, B.-L., *Science* **2012**, 1219831.

(7) (a) Graciani, J.; Mudiyanselage, K.; Xu, F.; Baber, A. E.; Evans, J.; Senanayake, S. D.; Stacchiola, D. J.; Liu, P.; Hrbek, J.; Sanz, J. F., *Science* **2014,** *345*, 546; (b) Martin, O.; Martín, A. J.; Mondelli, C.; Mitchell, S.; Segawa, T. F.; Hauert, R.; Drouilly, C.; Curulla-Ferré, D.; Pérez-Ramírez, J., *Angew. Chem. Int. Ed.* **2016,** *55*, 6261; (c) Liu, C.; Yang, B.; Tyo, E.; Seifert, S.; DeBartolo, J.; von Issendorff, B.; Zapol, P.; Vajda, S.; Curtiss, L. A., *J. Am. Chem. Soc.* **2015,** *137*, 8676.

(8) Studt, F.; Sharafutdinov, I.; Abild-Pedersen, F.; Elkjær, C. F.; Hummelshøj, J. S.; Dahl, S.; Chorkendorff, I.; Nørskov, J. K., *Nat. Chem.* **2014,** *6*, 320.

(9) Li, C.-S.; Melaet, G.; Ralston, W. T.; An, K.; Brooks, C.; Ye, Y.; Liu, Y.-S.; Zhu, J.; Guo, J.; Alayoglu, S., *Nat. Commun.* **2015,** *6*, 6538.

(10) Cavka, J. H.; Jakobsen, S.; Olsbye, U.; Guillou, N.; Lamberti, C.; Bordiga, S.; Lillerud, K. P., *J. Am. Chem. Soc.* **2008,** *130*, 13850.

(11) Wang, W.; Wang, S.; Ma, X.; Gong, J., *Chem. Soc. Rev.* **2011,** *40*, 3703.

(12) Lu, G.; Li, S.; Guo, Z.; Farha, O. K.; Hauser, B. G.; Qi, X.; Wang, Y.; Wang, X.; Han, S.; Liu, X., *Nat. Chem.* **2012,** *4*, 310.

(13) Han, Y.; Lee, S. S.; Ying, J. Y., *Chem. Mater.* **2007,** *19*, 2292.

(14) Van den Berg, R.; Parmentier, T. E.; Elkjær, C. F.; Gommes, C. J.; Sehested, J.; Helveg, S.; de Jongh, P. E.; de Jong, K. P., *ACS Catal.* **2015,** *5*, 4439.

(15) (a) Kuo, C.-H.; Tang, Y.; Chou, L.-Y.; Sneed, B. T.; Brodsky, C. N.; Zhao, Z.; Tsung, C.-K., *J. Am. Chem. Soc.* **2012,** *134*, 14345; (b) Hung, L. I.; Tsung, C. K.; Huang, W.; Yang, P., *Adv. Mater.* **2010,** *22*, 1910.

(16) Tulig, K.; Walton, K. S., *RSC Adv.* **2014,** *4*, 51080.

(17) (a) Hu, P.; Zhuang, J.; Chou, L.-Y.; Lee, H. K.; Ling, X. Y.; Chuang, Y.-C.; Tsung, C.-K., *J. Am. Chem. Soc.* **2014,** *136*, 10561; (b) Luz, I.; Loiudice, A.; Sun, D. T.; Queen, W. L.; Buonsanti, R., *Chem. Mater.* **2016,** *28*, 3839; (c) Müller, M.; Hermes, S.; Kähler, K.; van den Berg, M. W.; Muhler, M.; Fischer, R. A., *Chem. Mater.* **2008,** *20*, 4576.

(18) Férey, G.; Mellot-Draznieks, C.; Serre, C.; Millange, F.; Dutour, J.; Surblé, S.; Margiolaki, I., *Science* **2005,** *309*, 2040.

(19) Park, K. S.; Ni, Z.; Côté, A. P.; Choi, J. Y.; Huang, R.; Uribe-Romo, F. J.; Chae, H. K.; O'Keeffe, M.; Yaghi, O. M., *Proc. Natl. Acad. Sci. U.S.A.* **2006,** *103*, 10186.

(20) Joo, S. H.; Park, J. Y.; Tsung, C.-K.; Yamada, Y.; Yang, P.; Somorjai, G. A., *Nat. Mater.* **2009,** *8*, 126.

(21) Arena, F.; Barbera, K.; Italiano, G.; Bonura, G.; Spadaro, L.; Frusteri, F., *J. Catal.* **2007,** *249*, 185.

(22) Alayoglu, S.; Beaumont, S. K.; Zheng, F.; Pushkarev, V. V.; Zheng, H.; Iablokov, V.; Liu, Z.; Guo, J.; Kruse, N.; Somorjai, G. A., *Top. Catal.* **2011,** *54*, 778.

(23) Yin, M.; Wu, C.-K.; Lou, Y.; Burda, C.; Koberstein, J. T.; Zhu, Y.; O'Brien, S., *J. Am. Chem. Soc.* **2005,** *127*, 9506.

(24) Long, J.; Wang, S.; Ding, Z.; Wang, S.; Zhou, Y.; Huang, L.; Wang, X., *Chem. Commun.* **2012,** *48*, 11656.

(25) Lewera, A.; Timperman, L.; Roguska, A.; Alonso-Vante, N., *J. Phys. Chem. C* **2011,** *115*, 20153.

(26) Yang, Y.; Mims, C. A.; Mei, D.; Peden, C. H.; Campbell, C. T., *J. Catal.* **2013,** *298*, 10.

(27) Samson, K.; Sliwa, M.; Socha, R. P.; Góra-Marek, K.; Mucha, D.; Rutkowska-Zbik, D.; Paul, J.; Ruggiero-Mikołajczyk, M.; Grabowski, R.; Słoczyński, J., *ACS Catal.* **2014,** *4*, 3730.

Chapter 3

Single–Site Catalyst in Metal–Organic Framework for CO oxidation

3.1 Introduction

Reduction of nanoparticles' size to their atomic limits has been a goal in heterogeneous catalysis to maximize the number of active sites and increase their selectivity for specific reaction pathways.[1] The challenge is to stabilize and prevent such single atom with high surface free energy from migration and sintering during reactions, a common cause for catalyst deactivation. Extensive efforts to address this problem have focused on loading minute amount of active metal onto metal oxide supports using strong metal-support interaction (SMSI).[2] However, control of the spatial location and the local environment of metal active sites on these ill-defined surfaces of metal oxide supports remain difficult.[3] We envisaged that the well-defined structure of metal–organic frameworks (MOFs) can be used to install the active site with high specificity as well as to prevent the sintering problem.[4] The exceptionally large surface area of MOF can lead to a single atom dispersion with reasonable metal loadings. Additionally, isolated nature of metal oxide clusters separated by organic linkers may restrain the migration of these single atoms. The modification of SMSI can be readily achieved by the selection of suitable metal oxide clusters which are widely available in MOFs.[5]

Among any others, CO oxidation occupies a central role in heterogeneous catalysis as a reaction for both for fundamental studies and practical applications.[6] It is an essential reaction for reducing CO emissions in gas exhausts and for the ultra-purification of H_2 feed gases for ammonia synthesis and low-temperature fuel cell applications, through preferential CO oxidation (PROX).[7] In addition, CO oxidation is an ideal model reaction for the assessment of catalytic performances of different catalytic systems.[6a]

Here, we report Cu/UiO-66 catalyst where Cu atoms are covalently attached onto the Zr oxide clusters of UiO-66, $Zr_6O_4(OH)_4(BDC)_6$ (BDC^{2-} = 1,4-benzenedicarboxylate).[8] We investigated its catalytic performance for CO oxidation under idealized and completely realistic reaction conditions over a wide temperature range, as well as for the preferential CO oxidation (PROX). Geometric and electronic properties of the catalyst were examined using a combination of time-resolved operando and ex-situ spectroscopies providing insights into the structure of the living catalyst during reaction. Density functional theory (DFT) calculations guided by experimental data provides further information into the structure of the catalyst.

3.2 Experimental Section

Chemicals. All chemicals unless noted were obtained from Sigma-Aldrich. Acetone was purchased from Fischer Scientific. Acetic acid was obtained from EMD Millipore Chemicals. These chemicals were used without further purification. DEF was purified with activated charcoal and molecular sieves before passing them through the columns of a Grubbs-type solvent purification system.

Analytical techniques. Powder X-ray diffraction patterns (PXRD) were recorded using a Bruker D8 Advance diffractometer (Göbel-mirror monochromated Cu Kα radiation $\lambda = 1.54056$ Å). The amounts of Cu in the samples were analyzed by an ICP–OES spectroscope (Optima 7000 DV, Perkin Elmer). The samples (~2 mg) were digested in a solution mixture of nitric acid (0.5 mL), hydrochloric acid (1.5 mL) and hydrofluoric acid (0.1 mL) in 70 °C water bath for an hour. The resulting solutions were diluted with milliQ water to 10 mL before the measurement. Elemental microanalyses (EA) were performed in the Microanalytical Laboratory at the College of Chemistry, UC Berkeley using a Perkin Elmer 2400 Series II CHNS elemental analyzer. Gas adsorption analyses were performed on a Quantachrome Quadrasorb-SI automatic volumetric gas adsorption analyzer. A liquid nitrogen bath (77 K), ultra-high purity grade N_2 and He (99.999%, Praxair) were used for the measurements. The samples were prepared and measured after evacuating at 120 °C for 12 h. Thermal gravimetric analysis (TGA) was performed using a TA Instruments Q500 thermal gravimetric analyzer under nitrogen or air flow and a heating rate of 5 °C min^{-1}. Solution ^{1}H NMR spectra of digested samples were acquired on a Bruker AVB-400 (400 MHz) spectrometer at 297–300 K. Samples of MOFs (~5 mg) were digested and dissolved by sonication in a mixture of DMSO-*d6* (560 uL), hydrofluoric acid 48% (20 uL) and D_2O (20 uL). Scanning electron microscope (SEM) images were obtained using a Zeiss Gemini Ultra-55 analytical scanning electron microscope. The samples were prepared by dispersing MOF samples in acetone by sonication and the samples were drop-casted on a silicon wafer. A built-in Energy dispersive X-ray spectroscopy (EDS) detector was used for elemental analysis. Single crystal x-ray diffraction data were collected using synchrotron radiation on beamline 12.2.1 at the Advanced Light Source (ALS) at Lawrence Berkeley National Lab (LBNL). Beamline 12.2.1 is equipped with a PHOTON-II CMOS detector operating in shutterless mode, and the radiation is monochromated using silicon (111). Transmission Electron Microscopy (TEM) samples were prepared by dispersing the samples in acetone using a sonic bath followed by drop casting onto carbon film on copper grids. The images were taken using JEOL JEM-2100 LaB_6 operating at 200 kV.

Synthesis of MOFs:

Synthesis of UiO-66. UiO-66 was synthesized following the reported protocol.[9] In a 20-mL scintillation vial, 1,4-benzenedicarboxylic acid and zirconium tetrachloride were dissolved in a solution containing DMF (10 mL) and acetic acid (0.7 mL). The vial was sealed and heated in a 120 °C isothermal oven for a day. White powder was collected by centrifugation (10,000 rpm, 5 min), washed four times with DMF (5 mL × 4) over 24 h period, and four times acetone (5 mL ×

4) over 24 h period. Finally, UiO-66 was dried under dynamic vacuum overnight at room temperature.

Synthesis of Cu/UiO-66. UiO-66 (600 mg) was added to the solution containing CuCl2·2H2O (Aldrich, 99.99%, 540 mg) dissolved in DMF (9 mL). The suspension was sonicated for one minute. The vial's thread was wrapped with PTFE tape, sealed and heated in an 85 °C isothermal oven for a day. The product was collected by centrifugation (10,000 rpm, 5 min), washed three times with DMF (30 mL × 4) over 24 h period, and four times acetone (30 mL × 4) over 24 h period. Finally, Cu-UiO-66 was dried under dynamic vacuum overnight at room temperature

Single crystals of UiO-66. Following the reported procedure, zirconium oxychloride octahydrate (12 mg) was dissolved in DEF (1 mL).[10] Separately, terephthalic acid (5 mg) was dissolved in DEF (1 mL). The solutions were mixed in a 20-mL scintillation vial and formic acid (2 mL) was added. The resulting solution was shaken and placed in a 120 °C isothermal oven for 2 days. The crystals were washed with DMF 5 times (5 mL × 5) over 3 days.

Single crystals of Cu-UiO-66. Approximately 5 mg of single crystals of UiO-66 was added to a solution of $CuCl_2·2H_2O$ (Aldrich, 99.99%, 60 mg) dissolved in DMF (1 mL) in a 4-mL scintillation vial. The reaction was sealed and heated in an 85 °C isothermal oven for 5 days. The crystals were washed with DMF 5 times (5 mL × 5) over 3 days.

Catalysis:

The kinetic measurements were carried out in quartz tube micro-reactor at atmospheric pressure, using high purity gases (99.999%) under a continuous flow of reaction gases using mass flow controllers. The reaction products were analyzed by on-line gas chromatograph with a CO detection limit of <10 ppm (DANI 86.10), using hydrogen as a carrier gas. The Cu mass-normalized reaction rates were calculated from the CO conversion under differential reaction conditions (conversion < 30%).

Operando DRIFTS measurements:

Time-resolved in situ DRIFTS measurements were carried out using a commercial reaction cell (Harricks, HV-DR2). The outlet reaction gases were continuously monitored by dispersive gas phase infrared spectrometer, coupled with a hollow-waveguide. The spectra were recorded using a Magna 6700 spectrometer (Thermo-Fischer), equipped with an MCT narrow-band gap detector. The intensities of different bands were evaluated in Kubelka-Munk units, which are linearly proportional to the coverage of adsorbed surface species. Background subtraction and normalization of the spectra were performed using spectra recorded in a flow of N_2 directly after the catalyst pretreatment.

Operando XAS:

Operando XANES and EXAFS measurements were conducted in a transmission mode at the Cu K-edge at the P65 beamline of the Pettra-3 extension (DESY), using a Si(111) double crystal monochromator. The measurements were carried out under differential reaction conditions (CO conversion <5 %) using ~20 mg of diluted Cu/UiO-66 (catalyst diluted 1:1 with SiO_2) under a continuous flow of idealized CO oxidation reformate, where the conversion was recorded using on-line gas chromatography (influent and effluent gases). Background subtraction and normalization of the XANE spectra were performed using the Athena software from the IFEFFIT program package. Linear combination fitting of the XANES spectra of the reaction spectra was carried out using reference spectra of Cu foil, Cu_2O and CuO. Data reduction and evaluation of the EXAFS spectra were carried out using the XDAP software package. Theoretical references were calculated by the FEFF 8.0 code. EXAFS data were evaluated in R-space using fixed k and R ranges (k: 2.8 - 9.5 Å-1; R: 0-5.5 Å).

DFT Calculations:

The $Zr_6O_4(OH)_4(C_8H_4O_4)_{11}(OH)_1(H2O)_1$ cluster model was extracted from the single crystal structure of UiO-66 and 1,4-benzenedicarboxylate groups were replaced with acetate groups. Cu(II) was then allowed to coordinate to the defect site of the cluster. The clusters were geometrically optimized without symmetry constraint at the density functional theory (DFT) in gas phase using M06L-D3 functional as implemented in Gaussian 16 (revision A.03).[11] The 6-31G(d) basis sets were employed for C, O, Cl and H atoms while SDD basis sets were used for Cu and Zr atoms. Associated effective core potentials were used on all Cu and Zr atoms. Auto density fitting was used and numerical integrations were performed on an ultrafine grid. During geometry optimization, carbon atoms of acetate groups were frozen to simulate the rigidity of the framework. Minima of all geometry-optimized structures were verified by having no imaginary frequency found from analytical frequency calculation performed at the same level of theory.

3.3 Results and Discussion

Synthesis of Cu/UiO-66 catalyst. We synthesized UiO-66 using acetic acid as a modulator to control the size and improve the crystallinity of the MOF.[9] As commonly observed, the MOF prepared here contained missing linker defects (Figure 3.1).[10,12] From ^1H nuclear magnetic resonance (NMR) of the digested MOF, elemental analysis and thermal gravimetric analysis, we found that the MOF contained one missing linker per chemical formula and the vacancy sites are capped by acetate molecules and $^-OH/OH_2$ molecules yielding $Zr_6O_4(OH)_4(C_8H_4O_4)_5(CH_3COO)_{0.7}(H_2O)_{1.3}(OH)_{1.3}$ as the actual chemical formula for UiO-66 synthesized here.

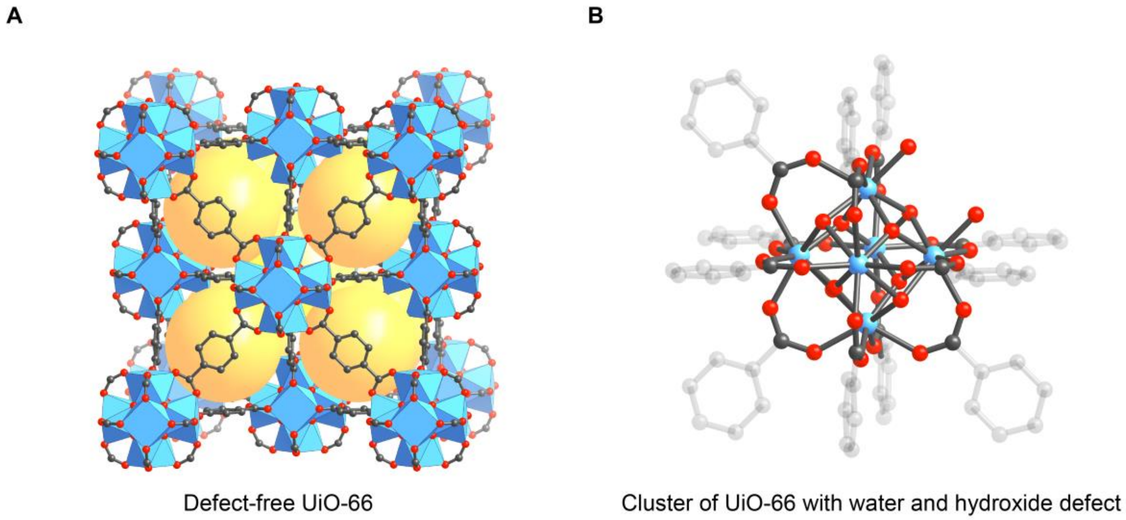

Figure 3.1. (A) Crystal structure of defect-free UiO-66 and (B) Zr oxide cluster of UiO-66 with $^{-}OH/H_2O$ and acetate molecules capping the defect sites. Atom labeling scheme: C, black; O, red; Cu, orange; Zr, blue polyhedra. H atoms are omitted for clarity. Yellow spheres represent the space in the framework.

Based on this structure, we prepared Cu/UiO-66 catalyst by heating UiO-66 in a solution of $CuCl_2 \cdot 2H_2O$ in DMF at 85 °C overnight to anchor Cu atoms on the $^{-}OH/OH_2$ defect sites. Inductively coupled plasma atomic emission spectroscopy analysis (ICP-AES) of Cu/UiO-66 shows the incorporation of Cu in Cu/UiO-66 with the Cu/Zr_6 molar ratio of 0.8. Despite the large excess of $CuCl_2 \cdot 2H_2O$ used in the synthesis, this ratio remains constant, indicating that the defect site of the MOF is the limiting reactant. Scanning electron microscopic (SEM) images of the materials before and after loading of Cu show the typical octahedral morphology of UiO-66 crystals without any impurity phase. Energy dispersive X-ray spectroscopic (EDS) analysis indicates the presence Cl with the molar ratio of Cu/Cl = ~1 suggesting that Cl^{-} may function as a ligand coordinating to Cu. From transmission electron microscopic (TEM) analysis, Cu or CuO_x nanoparticles formation was not observed. Powder X-ray diffraction (PXRD) of Cu/UiO-66 displays the diffraction lines in agreement with the simulated pattern of UiO-66 concurring the identity and phase purity of Cu/UiO-66 (Figure 3.2A).

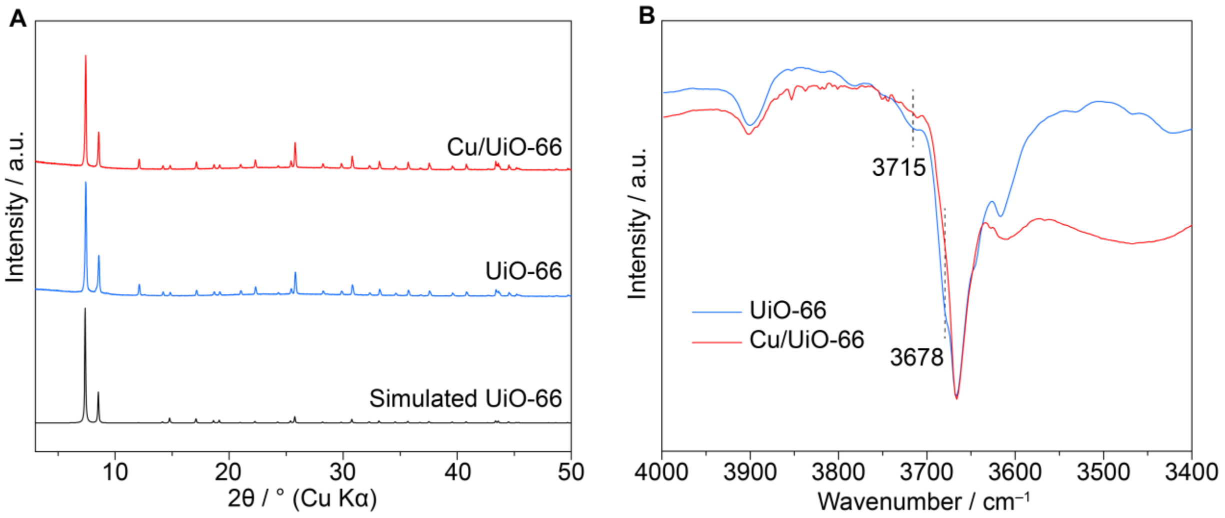

Figure 3.2. (A) Experimental PXRD pattern of UiO-66 and Cu/UiO-66 in comparison with the simulated pattern of UiO-66 and (B) DRIFTS spectra of UiO-66 overlaid with that of Cu/UiO-66.

Diffuse reflectance infrared Fourier transform spectroscopy (DRIFTS) spectra of Cu/UiO-66 in comparison to UiO-66 under continuous flow of N_2 at 250 °C show a significant decrease in intensity of the peaks at 3715 and 3678 cm^{-1}, attributable the O–H stretches of the defect sites on the Zr oxide clusters (Figure 3.2B).[13] This suggests that Cu atoms are bound to $^{-}OH/OH_2$ defect sites of UiO-66. These combined results indicate that Cu atoms are presented as atomically dispersed in the Cu/UiO-66 catalyst. To gain more information into the structure of the catalyst, we prepared single crystals of Cu/UiO-66 following the similar metalation conditions performed on microcrystalline Cu/UiO-66. Single crystal X-ray diffraction analysis reveals that Cu/UiO-66 crystallizes in the *Fm–3m* space group with a structure similar to the native UiO-66 confirming that the main portion of the framework remains unperturbed. However, the disorder and low occupancy of Cu site forbade us to obtain unambiguous characterization of the Cu sites using single crystal XRD. Instead, we performed operando X-ray absorption spectroscopy (XAS) analysis of the Cu/UiO-66 catalyst to elucidate the structure of the Cu site as discussed below.

CO oxidation and preferential CO oxidation. We pretreated the Cu/UiO-66 catalyst with 10% H_2/N_2 at 250 °C for 1 h and investigated the catalytic activity for CO oxidation in idealized reformate (1% CO, 1% O_2, 98% N_2) at 250 °C for over 2500 min. The catalyst exhibited a rather slow but steady activation phase for over 750 min until it reached its highest activity (Figure 3.3A). The activity became stable for the remaining 1500 min on stream. The temperature dependence of activity was also examined between 250 °C and 80 °C. As depicted in Figure 3.3B, the Cu mass normalized activity and the corresponding turnover frequencies (TOF) display almost an exponential dependence on the reaction temperature. The catalytic activity increases slowly for the reactions conducted at temperatures between 80 °C and 150 °C (from 3.5 to 4.8 $\mu mol_{CO}\ g_{Cu}^{-1}\ s^{-1}$, followed by a dramatic increase in the activity at the reaction temperatures between 180 and 250 °C (from 20.9 to 363 $\mu mol_{CO}\ g_{Cu}^{-1}\ s^{-1}$). Assuming all Cu atoms are accessible to the reactants, TOF values were determined to be $0.22 \times 10^{-3}\ s^{-1}$ at 80 °C and $17.5 \times 10^{-3}\ s^{-1}$ at 250 °C.

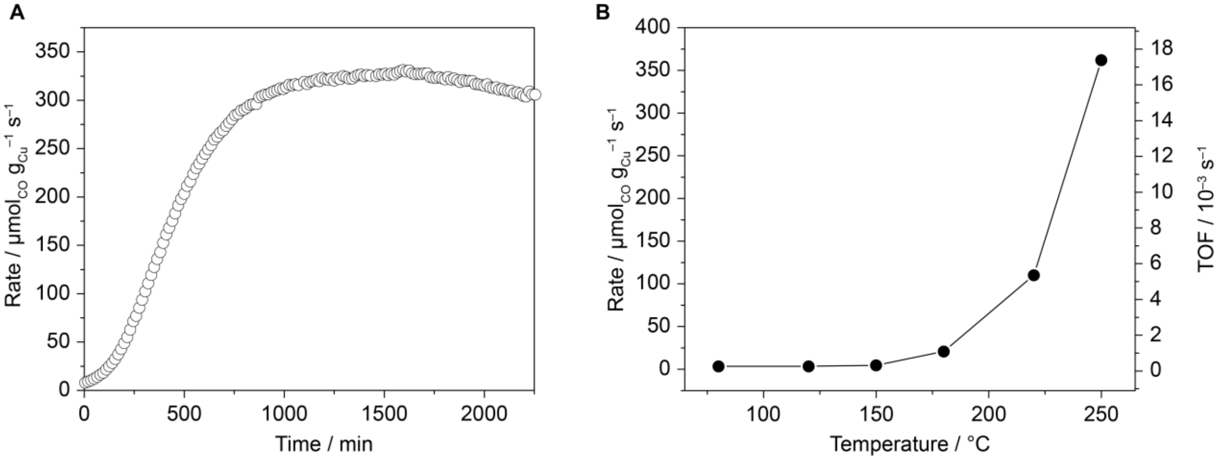

Figure 3.3. Catalytic oxidation of CO to CO_2 over Cu/UiO-66 in an idealized reformate gas mixture (1% CO, 1% O_2, 98% N_2, 30 sccm): (A) CO conversion rate as a function of time at 250 °C and (B) temperature dependent catalytic activity after reaching steady state at 250 °C.

Considering the pronounced increase of the activity as a function of temperature, we tested the catalyst under completely realistic reaction conditions at a temperature of 350 °C, a typical operating temperature for catalytic converters. Cu/UiO-66 (30 mg) was loaded into a flow reactor, activated at 250 °C, and investigated for the catalytic oxidation of 1 % CO at 350 °C in a synthetic air (21% O_2, 78% N_2) after reaching a steady state at 250 °C. The catalyst shows a steady 98% CO conversion for over 700 min at 350 °C (Figure 3.4A). To simulate a condition for the catalyst during shutdown of car engines, we removed CO from the gas feed and abruptly decreased the temperature to 25 °C under a continuous flow of synthetic air (21% O_2, 78% N_2). The reactor cell was disconnected to allow ambient air to flow through the catalyst for 2 h. Afterward, the same catalyst was loaded and tested for CO oxidation activity by rapidly increasing the temperature to 250 °C within 5 min in the synthetic air and subsequently to 350 °C. Interestingly, the catalyst exhibited the CO conversion of 70% at 250 °C and 98% at 350 °C, indicating that the catalyst restored its original activities before the shutdown step. By comparing CO oxidation activity of Cu/UiO-66 under realistic conditions to that of Cu/CeO_2 which is among the most active Cu-based catalysts for CO oxidation, Cu/UiO-66 catalyst is, at least 3 times more active than Cu/CeO_2 catalysts.[14]

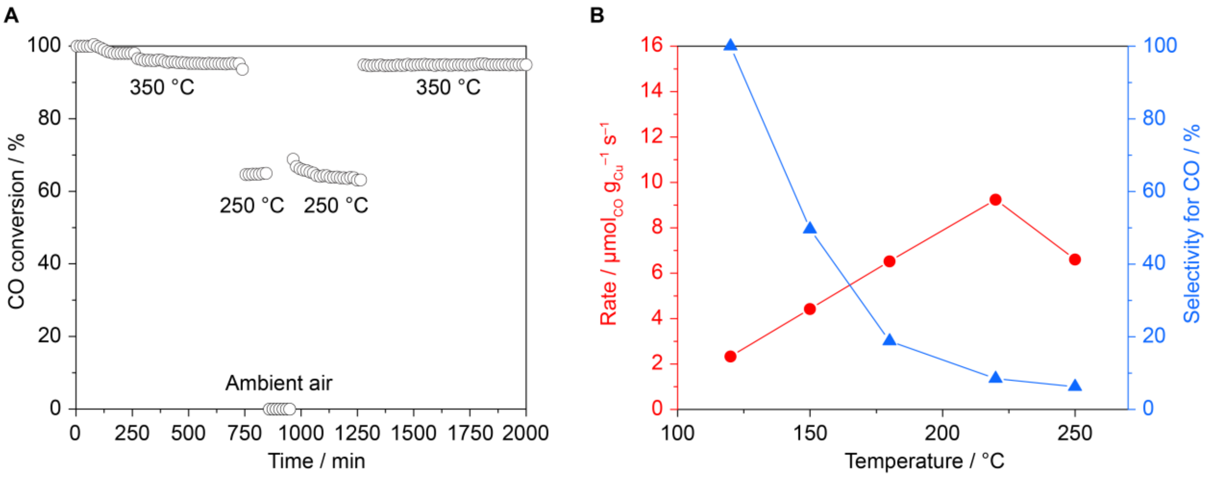

Figure 3.4. (A) Catalytic activity CO conversion in synthetic air composition (1% CO, 21% O_2, 78% N_2, 30 sccm) at different temperature and after the simulated shutdown (cooling the catalyst from 350 °C and kept in ambient air at 25 °C for 2 h) and restart again by heating in reaction gas mixture to 250 °C and subsequently to 350 °C and (B) Cu mass normalized CO oxidation rate at different temperatures (120-250 °C) in a H_2-rich preferential CO oxidation reformate (1%CO, 1% O_2, 18% N_2, 80% H_2, 30 sccm) and catalyst selectivity for CO oxidation.

We also evaluated the catalyst for preferential oxidation of CO (PROX) using a H_2-rich PROX reformate (1% CO, 1% O_2, 18% N_2 and 80% H_2) (Figure 3.4B). The catalyst displayed a 100% selectivity toward CO over H_2 at 120 °C with no measurable activity for H_2 oxidation. However, the selectivity for CO oxidation decreased gradually with increasing temperature. In contrast to the drastic increase of CO conversion with respect to temperatures observed under the flow of realistic reformate, CO conversion increased rather gradually with increasing temperature under the flow with H_2 as a mixture. This may be attributed to the change of oxidation state or competitive adsorption of H_2 on the catalytic sites required for O_2 activation or CO adsorption.

After these catalytic experiments, we examined the structural integrity of the catalyst using a combination of PXRD, TEM and DRIFTS measurements. The comparison of the PXRD patterns of the fresh and the spent Cu/UiO-66 catalysts indicates that the phase purity and crystallinity of the catalyst are retained, underlying the high stability of the catalyst.

Adsorption sites of CO during the reaction. Time-resolved operando DRIFTS measurements were performed during CO oxidation at 250 °C under a continuous flow of the idealized gas reformate. In a DRIFTS gas cell, CO oxidation rates were found to be lower than what we observed in the flow micro-reactor due to a much higher gas space velocity in DRIFTS experiments. However, the kinetics profiles are similar in that they both showed a slow activation phase. As depicted in Figure 3.5, the temporal evolution of the reaction spectra consists of two periods: from 0 to 20 min and from 30 min to 1550 min. Overall, the CO oxidation rate correlated with the evolution of the gas phase signal of CO_2 at 2348 cm^{-1}. During the first 20 min, a CO adsorption band located at 2113 cm^{-1} was observed, a characteristic stretch for CO adsorbed on Cu^{1+} (Figure 3.5A).[15] After 20 min, there is restructuring the catalyst as indicated by the change in the frequencies of CO adsorption bands and reach a constant state with the CO adsorption band centered at 2132 cm^{-1} after 1150 min.

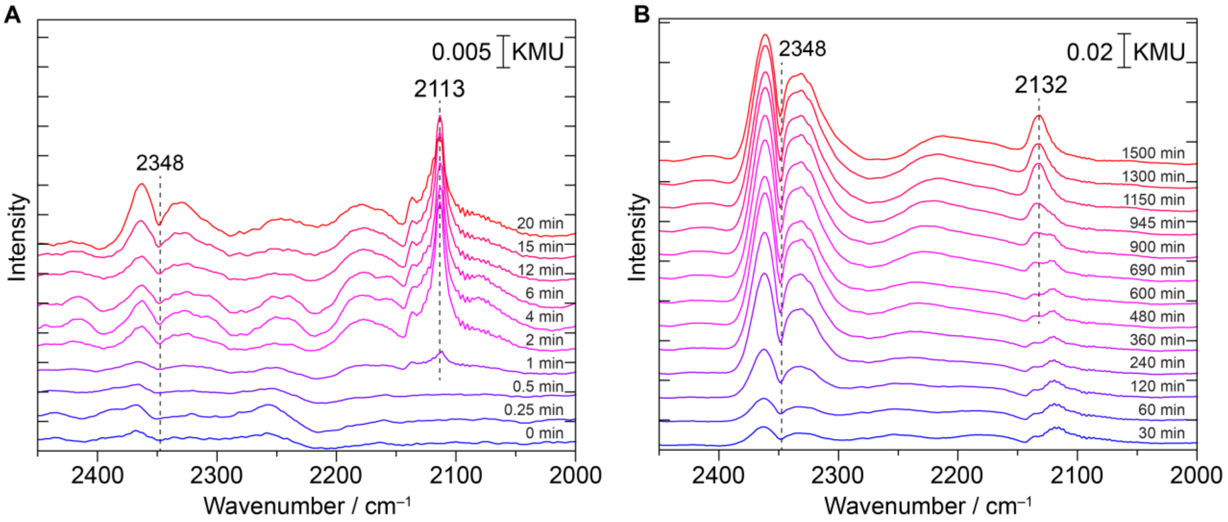

Figure 3.5. Operando time-resolved DRIFTS spectra of Cu/UiO-66 during CO oxidation (1% CO, 1% O_2, 98% N_2, 30 sccm): (A) during the first 20 min and (B) during 30 min to 1500 min.

Geometric and electronic properties of Cu site during the reactions. To investigate the change in electronic properties and the local coordination environment of Cu species during the reaction, we performed time-resolved operando Cu K-edge XAS measurements In the X-ray absorption near edge structure spectroscopy (XANES) region, we found a significant reduction of the white line intensity located at ~8982 eV after the hydrogen pretreatment of Cu/UiO-66 under the flow of 10% H_2/N_2 at 250 °C indicating the change in the oxidation state of the major species from Cu^{2+} to Cu^{1+} (Figure 3.6A).[16] During the CO oxidation, the majority of Cu sites were oxidized to Cu^{2+} within 3 min. (Figure 3.6B). Linear combination analysis of XANES spectra confirms this observation in that the oxidation state of all Cu sites is 1+ after the hydrogen pretreatment and the Cu sites were gradually oxidized during the CO oxidation. The eventual composition of the oxidation of the catalyst is determined to be 70% Cu^{2+} and 30% Cu^{1+}.

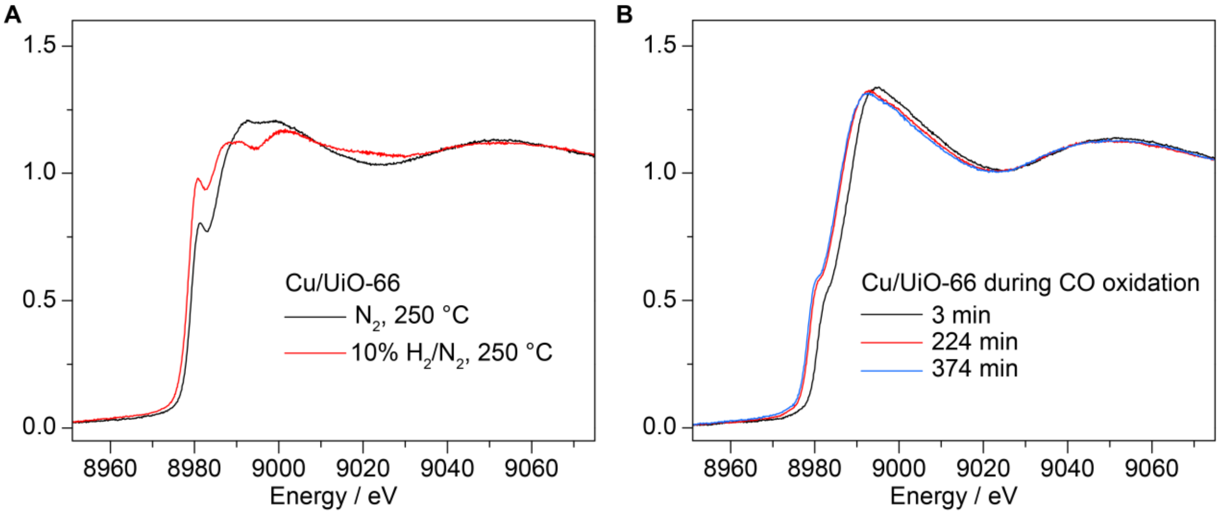

Figure 3.6. Normalized XANES spectra of Cu/UiO-66: (A) after drying in N_2 at 250 °C and after subsequent pretreatment in 10% N_2/H_2 and (B) during CO oxidation at 3 min, 224 min at 374 min.

Extend X-ray absorption fine structure (EXAFS) data analysis provides further insights into the local environment around Cu sites during the reactions. In the fresh Cu/UiO-66, the first shell is assigned to Cu–O/Cl an average coordination number (CN) of 3.2 ± 0.4 at a distance of 2.01 ± 0.02 Å (Figure 3.7A). This indicates that Cu is bound to the Zr oxide clusters of UiO-66 through the oxygen atoms, confirming the DRIFTS analysis described previously. After the hydrogen pretreatment, the main backscattering of Cu–O was observed at 1.98 ± 0.01 Å with a significant decrease of CN value to 1.15 ± 0.4 (Figure 3.7B). During CO oxidation, there is an increase in Cu–O coordination to 2.37± 0.27 which can be correlated to the change in the oxidation state of the Cu sites. This coordination number remains similar over the extended reaction time indicating the high stability of the coordination environment around Cu center atoms during CO oxidation (Figure 3.7D).

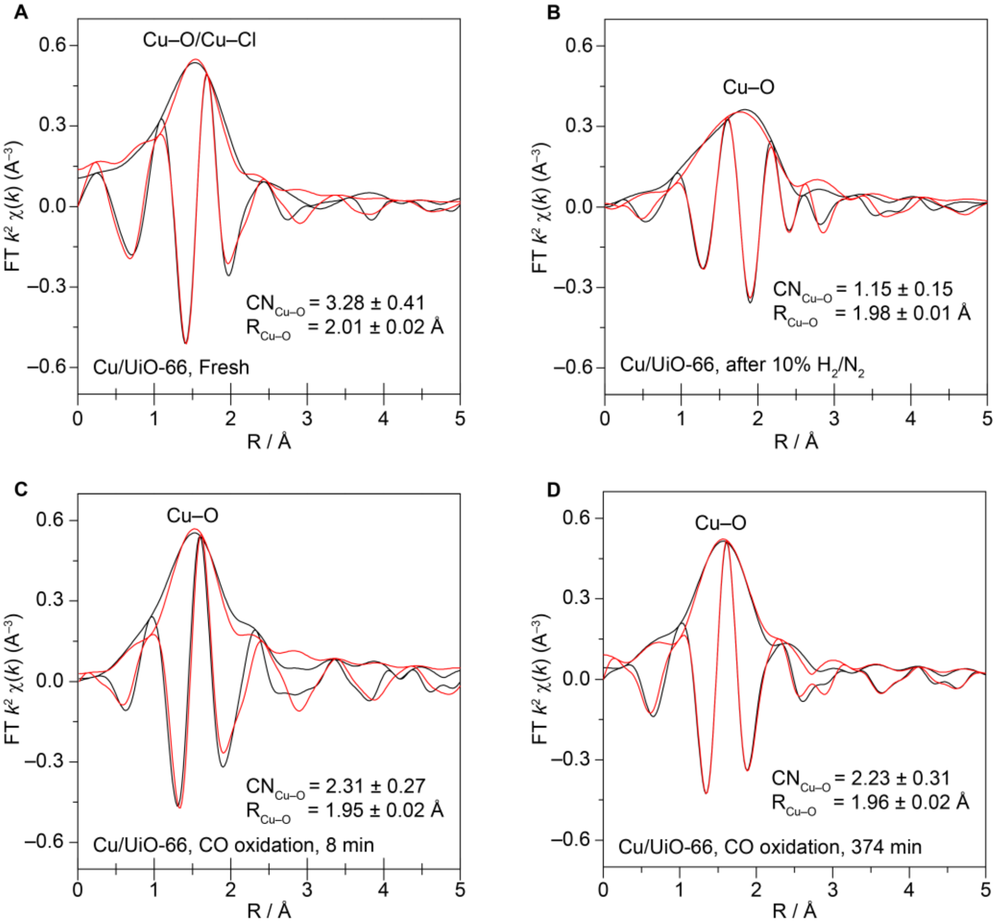

Figure 3.7. Fourier transformed EXAFS spectra of the fresh Cu/UiO-66 catalyst in N_2 at 25 °C (A), after the hydrogen pretreatment in 10% H_2/N_2 (B) and during CO oxidation in idealized reaction gas mixture (1% CO, 1% O_2, 98% N_2, 30 sccm) at 8 min (C) and at 374 min (D).

Density Functional Theory Calculations. To gain more information about the structure of the catalyst, we performed density functional theory (DFT) calculations based on experimental data. We modeled Cu/UiO-66 catalyst by anchoring Cu onto OH^-/H_2O defect site of UiO-66 with Cl^- as a ligand (Figure 3.8). The optimized structure shows that Cu is three coordinated with bond distances of Cu–O = 1.89, 1.95 Å and Cu–Cl = 2.15 Å. After the hydrogen pretreatment in the flow of H_2, the first shell coordination number is decreased to 1.2 ± 0.2 with the decrease in oxidation state from Cu(II) to Cu(I) We attribute this decrease of CN to the loss of Cl^- ligand DFT optimized structure of Cu–UiO-66 after hydrogen pretreatment indicates that Cu is two coordinated bound to OH^-/H_2O of the Zr cluster with Cu–O bond distances of 1.86 and 1.86 Å. These calculated bond distances are in close agreement with the EXAFS data.

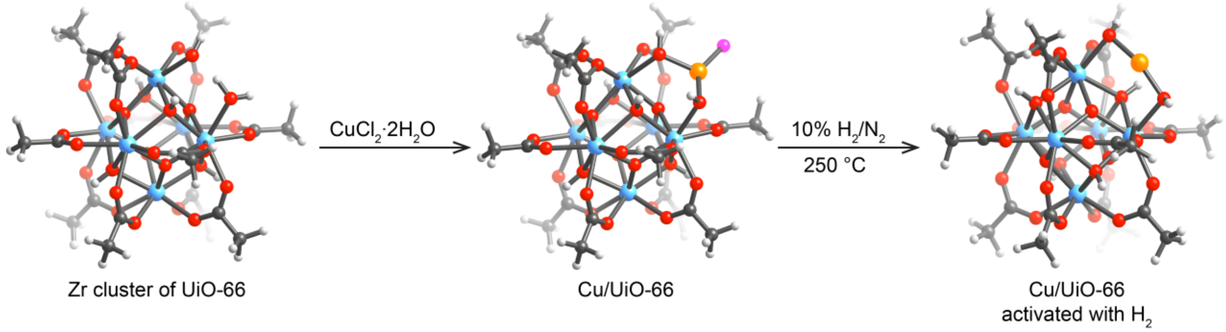

Figure 3.8. DFT calculated structures of defective UiO-66 (a), Cu-UiO-66 catalyst where Cu is coordinated to OH^-/H_2O defect site of UiO-66 (b) and Cu-UiO-66 after activation with H_2.

3.4 Conclusions

We prepared a stable atomically dispersed Cu/UiO-66 catalyst where a single atom of Cu is anchored on the Zr-oxide cluster of UiO-66. Catalytic testing revealed the high specific activity (both TOF and mass normalized) and stability of the catalyst for CO oxidation under idealized and completely realistic reaction conditions. The catalyst also shows exceptionally high selectivity (100 %) for CO oxidation in the presence of up to 80% H_2 in the gas feed at 120°C and decreased gradually with increasing reaction temperature. A combined time-resolved catalytic study and operando spectroscopic measurements reveal that the active sites responsible for the activity of these catalysts are atomically dispersed Cu species, existing as a mixed valence of Cu (70% Cu^{2+} and 30% Cu^{1+}).

3.5 Appendices

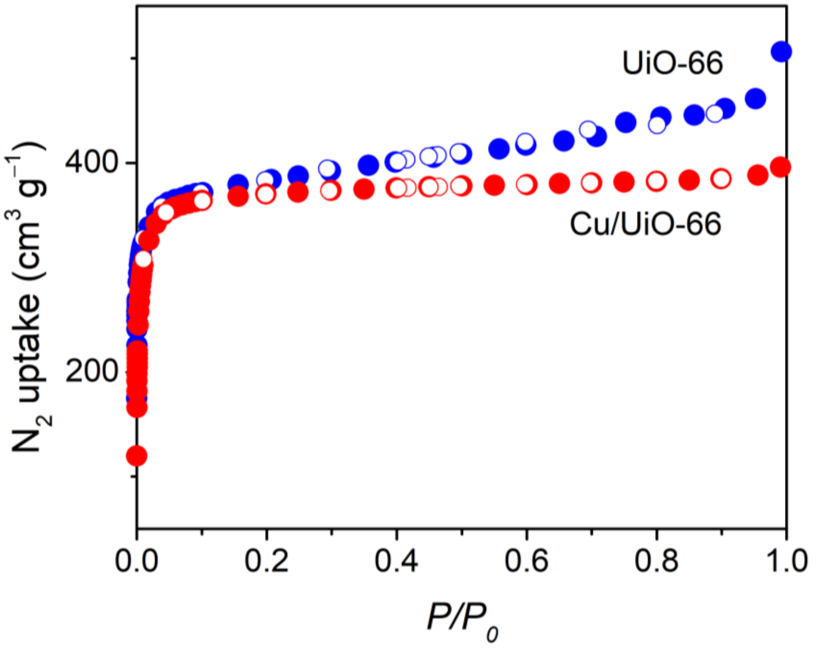

Figure A3.1. Nitrogen adsorption isotherms of UiO-66 and Cu/UiO-66.

Table A3.1. Summary of surfaces of the materials presented in the graphs shown above.

Material	Calculated BET surface area (m^2 g^{-1})
UiO-66	1140
Cu/UiO-66	1070

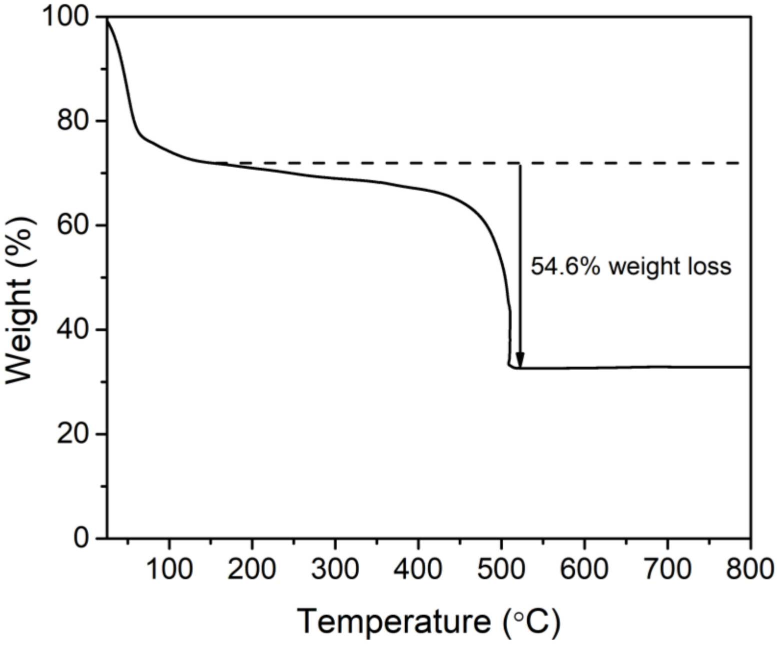

Figure A3.2. TGA trace of UiO-66 under nitrogen flow.

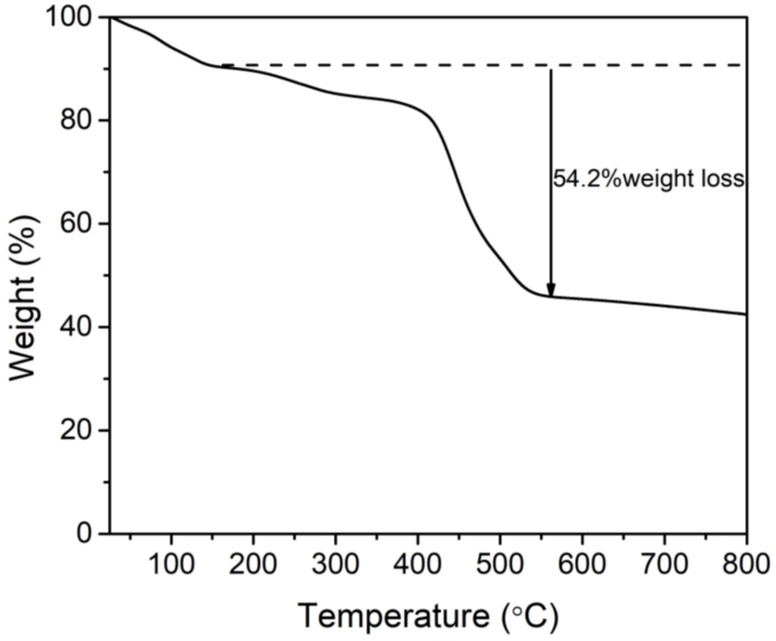

Figure A3.3. TGA trace of Cu/UiO-66 under nitrogen flow.

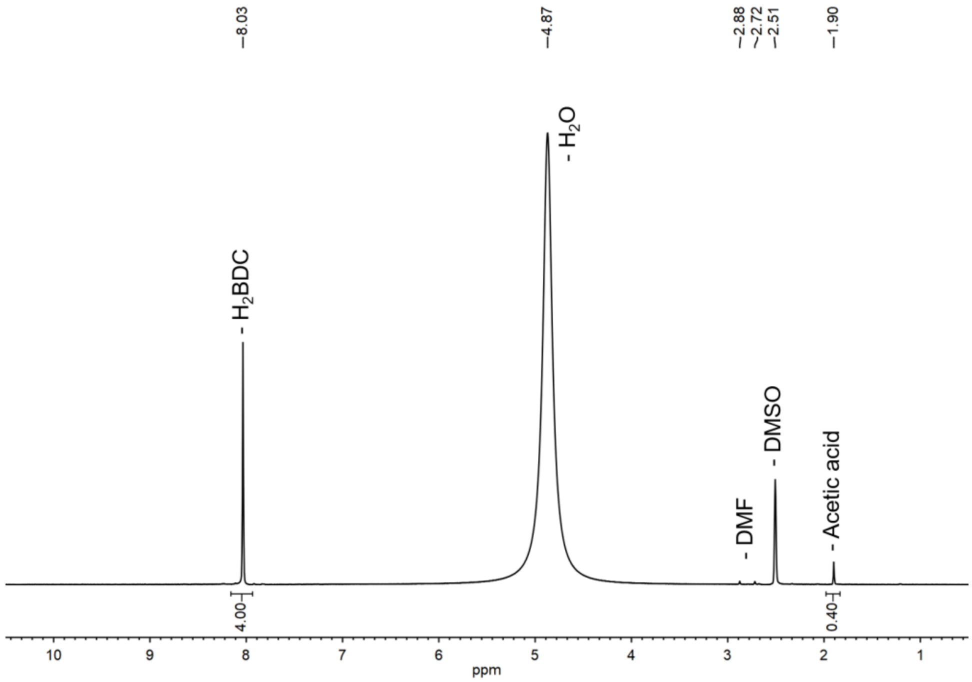

Figure A3.4. ^{1}H NMR spectrum of digested UiO-66.

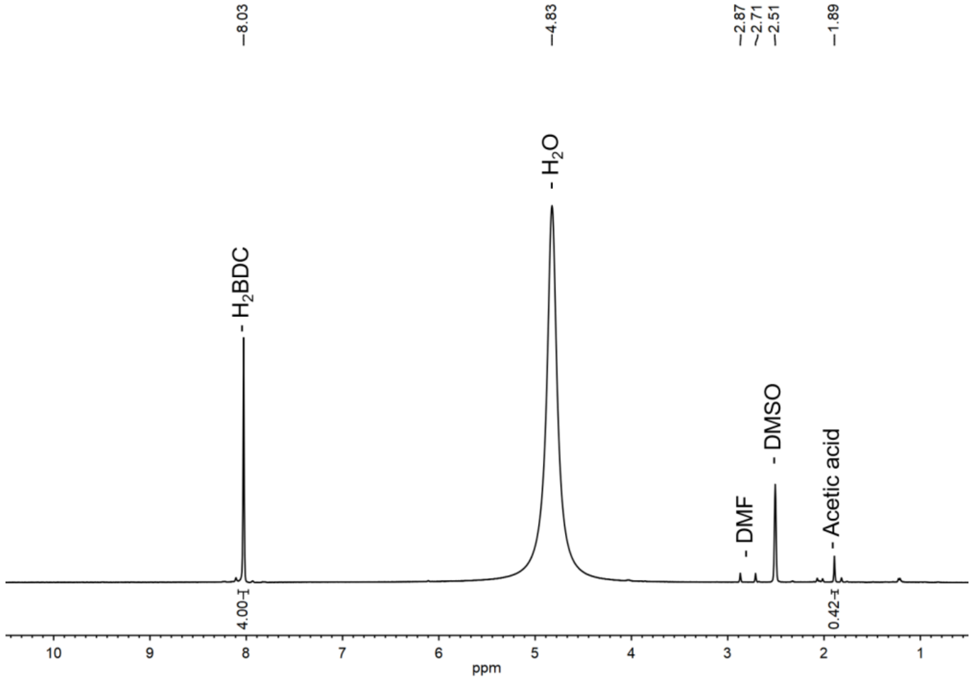

Figure A3.5. ^{1}H NMR spectrum of digested Cu/UiO-66.

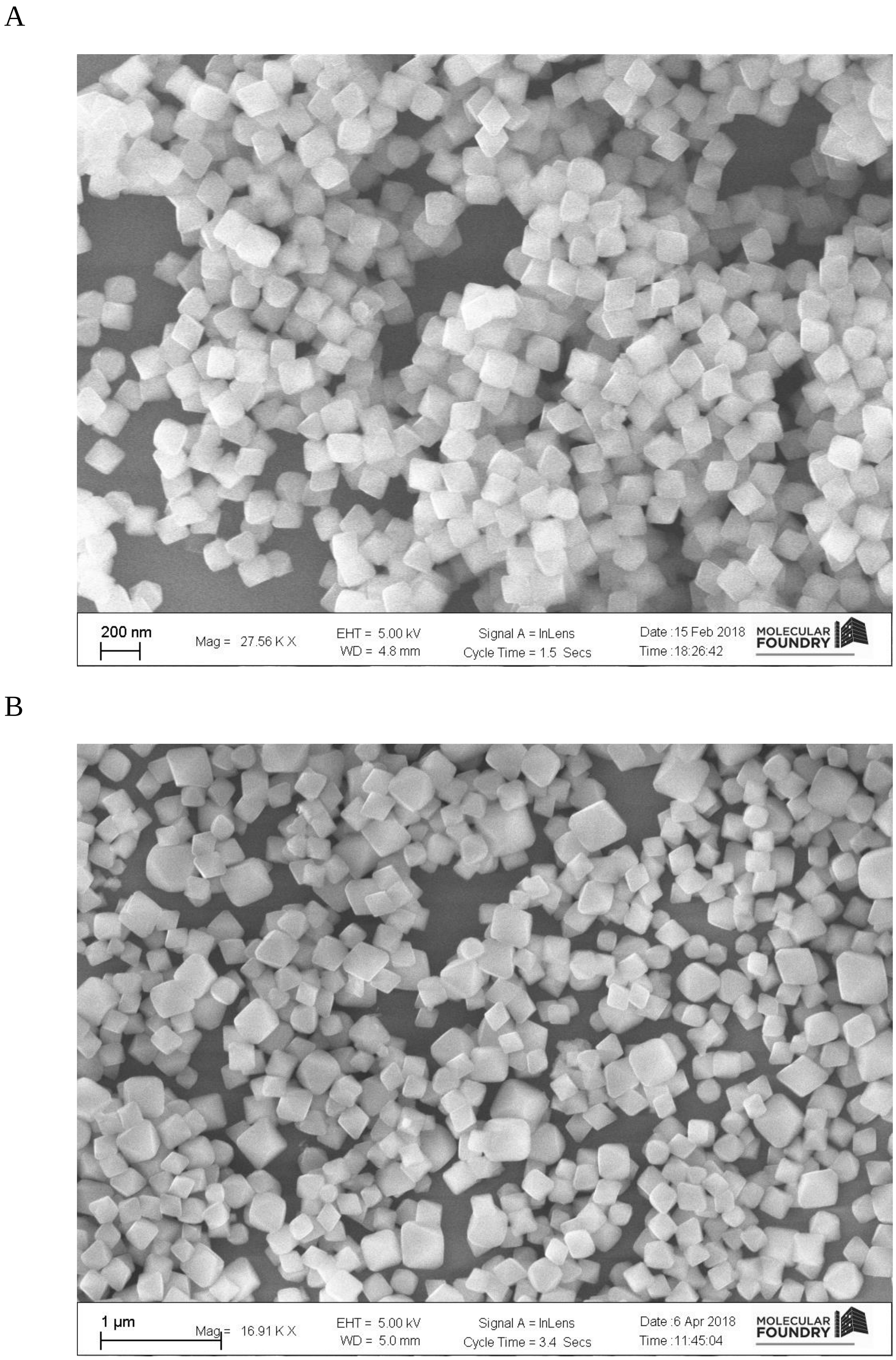

Figure A3.6. SEM images of (A) UiO-66 and (B) Cu/UiO-66.

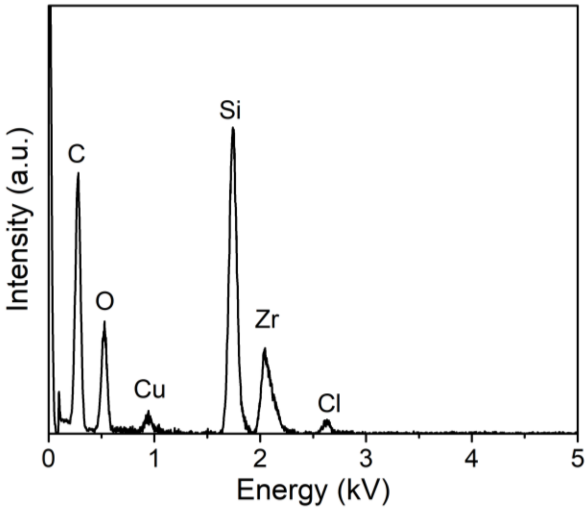

Figure A3.7. EDS spectrum of Cu-UiO-66 obtained using an accelerating voltage of 10 kV.

Table A3.2. Elemental composition of Cu/UiO-66 analyzed using EDS.

Element	Atom (%)
C	67.35±2.20
O	16.75±0.69
Cl	0.64±0.06
Cu	0.55±0.09
Zr	3.30±0.46
Si	11.42±0.49

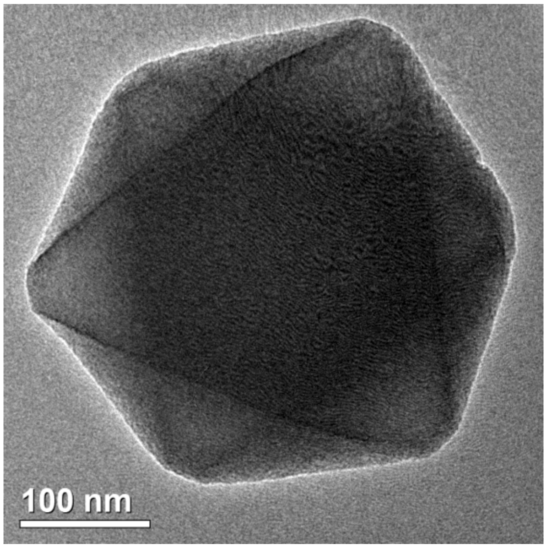

Figure A3.8. TEM image of the fresh Cu/UiO-66.

Table A3.3. Crystal data for Cu/UiO-66.

Empirical formula	$Zr_6C_{48}H_{28}O_{35.14}$
Formula weight	1714.30
Temperature/K	100
Crystal system	cubic
Space group	*Fm–3m*
a/Å	20.7102(9)
b/Å	20.7102(9)
c/Å	20.7102(9)
α/°	90
β/°	90
γ/°	90
Volume/Å^3	8882.9(12)
Z	192
ρ_{calc}g/cm^3	1.282
μ/mm^{-1}	0.797
F(000)	3348.0
Crystal size/mm^3	0.1 × 0.1 × 0.1
Radiation	Synchrotron ($\lambda = 0.7288$)
2Θ range for data collection/°	3.492 to 74.962
Index ranges	$-34 \leq h \leq 34$, $-34 \leq k \leq 34$, $-34 \leq l \leq 34$
Reflections collected	41560
Independent reflections	1150 [$R_{int} = 0.1196$, $R_{sigma} = 0.0430$]
Data/restraints/parameters	1150/0/43
Goodness-of-fit on F^2	1.268
Final R indexes [I>=2σ (I)]	$R_1 = 0.0471$, $wR_2 = 0.1286$
Final R indexes [all data]	$R_1 = 0.0488$, $wR_2 = 0.1305$
Largest diff. peak/hole / e Å^{-3}	1.52/-1.75

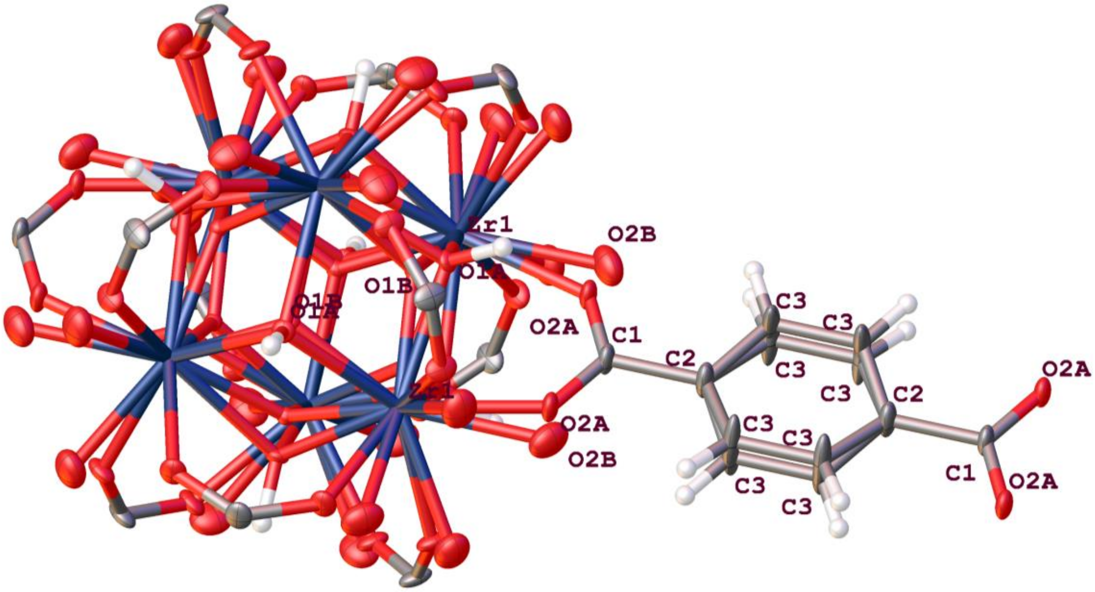

Figure A3.9. Partial structure of UiO-66 showing Zr oxide cluster and the organic linker resolved from single-crystal structure. Only one coordination site is depicted in the figure, others are omitted for clarity. Thermal ellipsoids are plotted with 50% probability.

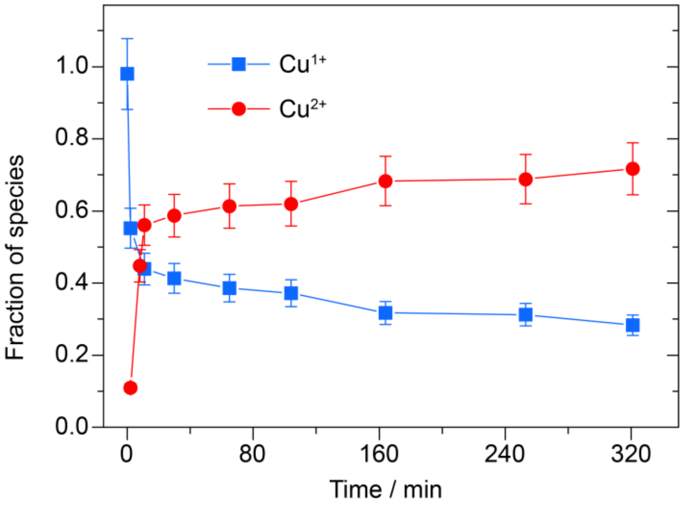

Figure A3.10. Linear combination analysis (LCA) of CO oxidation reaction spectra of Cu/UiO-66 during CO oxidation.

Table A3.4. XYZ coordinates for DFT optimized cluster model of UiO-66 with one missing linker defect.

O	19.6712	19.6959	19.6789
O	20.7120	17.1756	18.784
O	20.7160	18.7846	17.1829
C	20.7343	17.5868	17.5868
C	20.7343	16.5273	16.5273
O	22.1355	19.3296	19.3237
H	22.6947	18.7753	18.7662
O	18.7831	20.7232	17.1858
O	17.1721	20.7052	18.7829
C	17.5868	20.7343	17.5868
C	16.5273	20.7343	16.5273
O	19.2402	22.2205	19.3682
H	18.6792	22.7952	18.8292
Zr	20.7249	20.7578	18.2321
O	20.8339	24.2881	18.7720
O	22.6838	20.7618	17.1791
O	24.2886	20.7513	18.7839
O	20.6912	22.6824	17.1771
C	20.7343	23.8818	17.5868
C	20.7343	24.9413	16.5273
C	23.8818	20.7343	17.5868
C	24.9413	20.7343	16.5273
O	21.7489	21.7902	19.6828
O	17.1746	18.7836	20.7258
O	18.7827	17.1806	20.706
C	17.5868	17.5868	20.7343
C	16.5273	16.5273	20.7343
O	19.3155	19.3278	22.1383
H	18.7711	18.7624	22.6992
Zr	20.7353	18.2301	20.7281
O	24.2833	18.7852	20.7524
O	20.7480	17.1782	22.6841
O	22.6841	17.1749	20.7520
O	20.7509	18.7843	24.2880
C	23.8818	17.5868	20.7343
C	24.9413	16.5273	20.7343
C	20.7343	17.5868	23.8818
C	20.7343	16.5273	24.9413
O	21.7829	19.6786	21.7868
Zr	18.2270	20.7334	20.7269
O	17.0033	22.7050	20.8284
O	18.7787	20.7272	24.2871
O	18.8977	24.4628	20.7535
O	17.1656	20.7950	22.6853
C	17.5868	20.7343	23.8818
C	16.5273	20.7343	24.9413
O	19.6518	21.8028	21.7977
Zr	23.2203	20.7488	20.7243
Zr	20.6950	23.2988	20.7402
Zr	20.7354	20.7370	23.2228
O	24.2869	22.6835	20.7018
O	20.7210	24.3153	22.6959
O	22.6837	20.7202	24.2914
O	22.6876	24.2951	20.7331
O	24.2834	20.7203	22.6831
O	20.6992	22.6853	24.2829
C	23.8818	23.8818	20.7343
C	24.9413	24.9413	20.7343
C	20.7343	23.8818	23.8818
C	20.7343	24.9413	24.9413
C	23.8818	20.7343	23.8818
C	24.9413	20.7343	24.9413
O	22.1260	22.1545	22.1388
H	22.6956	22.6944	22.7000
H	18.8897	25.0933	21.4862
H	17.6914	23.4772	20.8303
H	16.5667	22.7291	21.6931
H	20.2334	25.8469	16.8796
H	20.2773	24.5837	15.6013
H	21.7735	25.2119	16.3035
H	24.5849	20.2600	15.6094
H	25.8568	20.2534	16.8813
H	25.1908	21.7743	16.2832
H	25.1612	25.2169	19.6955
H	25.8704	24.5770	21.1803
H	24.5960	25.8448	21.2433
H	16.2096	19.6998	16.3479
H	16.9061	21.1355	15.5843
H	15.6444	21.2893	16.8556
H	19.6964	25.2258	25.1560
H	21.2535	25.8407	24.6002
H	21.1706	24.5766	25.8748
H	25.8702	21.1780	24.5745
H	25.1591	19.6962	25.2211
H	24.5972	21.2471	25.8433
H	20.2372	15.6185	24.5924
H	20.2756	16.8893	25.8649
H	21.7734	16.2618	25.1723
H	16.8590	20.1927	25.8310
H	15.5869	20.3207	24.5685
H	16.3368	21.7698	25.2505
H	16.8842	15.6089	21.2075
H	16.2765	16.2833	19.6946
H	15.6121	16.8806	21.2162
H	25.8743	16.8973	20.3021
H	24.6018	15.6296	20.2109
H	25.1486	16.2383	21.7720
H	21.1851	16.8915	15.6008
H	19.6952	16.2555	16.3040
H	21.2391	15.6215	16.8732

Table A3.5. XYZ coordinates for DFT optimized cluster model of Cu/UiO-66.

Zr	13.2461	8.3042	21.4237
Zr	10.5684	12.1716	19.6419
Zr	13.3995	11.8417	21.7400
Zr	10.4096	8.6472	19.3224
Zr	10.3839	10.1442	22.5594
Zr	13.4025	10.3721	18.5205
O	14.9995	8.7711	22.697
O	8.8438	11.7341	18.3183
O	11.1569	14.2272	20.2227
O	12.6558	6.2690	20.8313
O	12.8721	12.414	23.8032
O	10.9419	8.0895	17.2342
O	8.6029	7.9125	20.3506
O	15.2024	12.6067	20.6841
O	10.4657	8.7458	24.2783
O	12.9722	11.9114	16.9774
O	15.0831	8.9436	18.3693
O	8.7351	11.5813	22.6902
O	15.0687	11.0270	22.9237
O	8.7570	9.4793	18.0915
O	10.8196	6.4921	19.5135
O	12.9699	14.0193	21.5708
O	14.9902	7.6364	20.2206
O	8.8632	12.9009	20.8474
O	11.1535	13.0617	17.6948
O	12.6954	7.2021	23.3358
O	15.2054	11.6557	18.6247
O	8.6736	8.7521	22.4589
O	10.9183	11.3751	24.3067
O	12.8564	9.1927	16.7249
C	15.4744	9.8523	23.1509
C	16.6750	9.7171	24.0372
C	8.3410	10.6553	17.8858
C	7.1403	10.7904	16.9996
C	12.1003	14.6815	20.9326
C	12.1652	16.1720	21.0720
C	11.7151	5.8261	20.1040
C	11.6500	4.3356	19.9647
C	11.9091	12.1128	24.5628
C	11.9097	12.7385	25.9243
C	11.9061	8.3948	16.4740
C	11.9056	7.7691	15.1125
C	8.1497	8.0868	21.5160
C	6.8849	7.3569	21.8518
C	15.6654	12.421	19.5208
C	16.9304	13.1506	19.1850
C	12.0988	12.8225	16.8882
C	12.1631	13.6872	15.6662
C	15.4728	7.9933	19.1066
C	16.6729	7.2324	18.6313
C	8.3425	12.5143	21.9303
C	7.1424	13.2752	22.4054
O	12.6237	9.9039	22.8954
H	12.9816	9.7688	23.7820
O	9.4721	10.3611	20.4845
H	8.5088	10.3923	20.4353
O	12.8330	12.2980	19.5822
H	13.1990	13.1102	19.2117
O	12.6560	8.3429	19.2292
H	12.9385	7.5757	18.7162
O	13.7087	10.1597	20.5810
O	11.3440	10.4322	18.8134
O	11.1808	8.6554	21.2912
O	11.3508	11.6667	21.5195
H	12.9669	6.2729	23.2483
H	11.1608	8.9404	24.9219
H	11.7717	16.6703	20.1823
H	13.1831	16.5074	21.2853
H	11.5352	16.4718	21.9185
H	11.3741	13.6943	25.8696
H	12.9256	12.9540	26.2658
H	11.3826	12.1132	26.6493
H	12.9207	7.6780	14.7180
H	11.3447	8.4175	14.4282
H	11.4057	6.7973	15.1242
H	6.2815	7.1726	20.9598
H	6.3077	7.8874	22.6136
H	7.1705	6.3827	22.2702
H	17.0132	14.0826	19.7496
H	17.0057	13.3403	18.1112
H	17.7826	12.5196	19.4661
H	11.5566	13.2244	14.8780
H	13.1857	13.7645	15.2882
H	11.7455	14.6785	15.8595
H	16.7452	7.2461	17.5409
H	16.6651	6.2056	19.0055
H	17.5739	7.7182	19.0257
H	6.4540	12.6236	22.9500
H	6.6309	13.7733	21.5783
H	7.4751	14.0495	23.1076
H	17.5571	9.5314	23.4126
H	16.5718	8.8538	24.7009
H	16.8522	10.6266	24.6156
H	6.4872	9.9180	17.0841
H	7.4780	10.8443	15.9573
H	6.5891	11.7092	17.2145
H	12.6408	3.8851	20.0672
H	11.1900	4.0467	19.0160
H	11.0187	3.9504	20.7738
Cu	10.7461	7.0894	23.4066
Cl	9.8965	5.1890	22.8773

Table A3.6. XYZ coordinates for DFT optimized cluster model of Cu/UiO-66 after hydrogen pretreatment.

Zr	13.1644	10.9700	21.0961
Zr	8.6228	9.0231	20.0296
Zr	9.7947	11.6958	22.0080
Zr	11.9453	8.2758	19.1073
Zr	11.0859	8.3982	22.5590
Zr	10.6637	11.5293	18.5931
O	13.1911	12.7778	22.3593
O	8.5149	7.2858	18.6433
O	6.8242	9.9403	20.9428
O	14.9231	10.0295	20.1573
O	9.4997	11.2363	24.1432
O	12.2294	8.7427	16.9418
O	12.596	6.3720	20.0118
O	9.1848	13.6381	21.0882
O	12.5583	7.9665	24.1954
O	8.8326	11.4073	17.3312
O	12.3092	12.9488	18.1886
O	9.3816	7.0539	22.9343
O	11.0703	13.1477	23.0668
O	10.6498	6.8018	18.0501
O	14.1503	8.2933	18.9093
O	7.5700	11.6620	22.2172
O	13.8987	12.5717	19.7643
O	7.8178	7.4324	21.3330
O	7.5215	9.8018	18.2517
O	14.6890	10.5369	22.6862
O	9.7421	13.5219	18.8924
O	11.9765	6.4357	22.1950
O	10.2323	9.1151	24.4765
O	11.4102	10.8323	16.6174
C	12.3167	13.3714	23.0421
C	12.8077	14.5093	23.8839
C	9.3985	6.6091	18.0410
C	8.9073	5.4709	17.1993
C	6.6674	10.9344	21.7096
C	5.2569	11.2523	22.1028
C	15.0475	9.0456	19.3737
C	16.4581	8.7278	18.9804
C	9.7441	10.2174	24.8454
C	9.3695	10.2942	26.2941
C	11.9707	9.7626	16.2380
C	12.3456	9.6860	14.7892
C	12.4754	5.8923	21.1766
C	13.0199	4.5128	21.3905
C	9.2397	14.0880	19.9065
C	8.6952	15.4674	19.6927
C	7.7807	10.7069	17.4059
C	6.7450	10.9482	16.3504
C	13.4300	13.1435	18.7384
C	14.2958	14.2052	18.1315
C	8.2852	6.8365	22.3446
C	7.4193	5.7750	22.9517
O	11.7715	10.5714	22.8532
H	11.9995	10.9199	23.7259
O	10.3294	7.6126	20.5447
H	10.1215	6.6707	20.5155
O	8.8807	11.2737	19.9692
H	8.0926	11.7820	19.7429
O	12.6303	10.4314	18.9409
H	13.3183	10.5925	18.2837
O	11.2797	11.7510	20.5828
O	10.2926	9.5059	18.8892
O	12.3987	9.0092	21.0347
O	9.5795	9.6556	21.7853
H	15.5153	10.2676	22.2574
H	12.2175	8.2905	25.0427
H	4.5522	10.9636	21.3187
H	5.1433	12.3096	22.3550
H	5.0045	10.6712	22.9983
H	8.3777	9.8439	26.4234
H	9.3128	11.3286	26.6423
H	10.0625	9.7194	26.9148
H	12.5796	10.676	14.3892
H	11.4882	9.3010	14.2235
H	13.1794	8.9975	14.6313
H	13.1715	3.9851	20.4461
H	12.3658	3.9378	22.0523
H	13.9881	4.5923	21.8998
H	7.9063	15.6989	20.4127
H	8.3351	15.5971	18.6689
H	9.5049	16.1908	19.8486
H	6.9554	10.2927	15.4963
H	6.7815	11.9786	15.9876
H	5.7442	10.7007	16.7132
H	14.0678	14.3493	17.0725
H	15.3557	13.9774	18.2716
H	14.0982	15.1541	18.6452
H	8.0239	4.9882	23.4104
H	6.7289	5.3535	22.2169
H	6.8185	6.2278	23.7501
H	12.9133	15.3963	23.2475
H	13.7973	14.2907	24.2943
H	12.1035	14.7522	24.6834
H	9.6548	4.6760	17.1352
H	8.7320	5.8368	16.1801
H	7.9584	5.0806	17.5753
H	17.0676	9.6341	18.9318
H	16.4972	8.1873	18.0314
H	16.9011	8.0779	19.7457
Cu	13.8757	9.1157	23.5633

3.6. References

(1) (a) Liang, S.; Hao, C.; Shi, Y., *ChemCatChem* **2015,** *7*, 2559; (b) Dhiman, M.; Polshettiwar, V., *ChemCatChem*.

(2) (a) Hackett, S. F.; Brydson, R. M.; Gass, M. H.; Harvey, I.; Newman, A. D.; Wilson, K.; Lee, A. F., *Angew. Chem.* **2007,** *119*, 8747; (b) Qiao, B.; Wang, A.; Yang, X.; Allard, L. F.; Jiang, Z.; Cui, Y.; Liu, J.; Li, J.; Zhang, T., *Nat. Chem.* **2011,** *3*, 634.

(3) Liu, J., *ACS Catal.* **2016,** *7*, 34.

(4) (a) Li, Z.; Peters, A. W.; Bernales, V.; Ortuño, M. A.; Schweitzer, N. M.; DeStefano, M. R.; Gallington, L. C.; Platero-Prats, A. E.; Chapman, K. W.; Cramer, C. J., *ACS Cent. Sci.* **2016,** *3*, 31; (b) Li, Z.; Schweitzer, N. M.; League, A. B.; Bernales, V.; Peters, A. W.; Getsoian, A. B.; Wang, T. C.; Miller, J. T.; Vjunov, A.; Fulton, J. L., *J. Am. Chem. Soc.* **2016,** *138*, 1977.

(5) (a) Furukawa, H.; Cordova, K. E.; O'Keeffe, M.; Yaghi, O. M., *Science* **2013,** *341*, 1230444; (b) Rungtaweevoranit, B.; Baek, J.; Araujo, J. R.; Archanjo, B. S.; Choi, K. M.; Yaghi, O. M.; Somorjai, G. A., *Nano Lett.* **2016,** *16*, 7645.

(6) (a) An, K.; Alayoglu, S.; Musselwhite, N.; Plamthottam, S.; Melaet, G. r. m.; Lindeman, A. E.; Somorjai, G. A., *J. Am. Chem. Soc.* **2013,** *135*, 16689; (b) Jernigan, G.; Somorjai, G., *J. Catal.* **1994,** *147*, 567.

(7) Saavedra, J.; Whittaker, T.; Chen, Z.; Pursell, C. J.; Rioux, R. M.; Chandler, B. D., *Nat. Chem.* **2016,** *8*, 584.

(8) Cavka, J. H.; Jakobsen, S.; Olsbye, U.; Guillou, N.; Lamberti, C.; Bordiga, S.; Lillerud, K. P., *J. Am. Chem. Soc.* **2008,** *130*, 13850.

(9) Na, K.; Choi, K. M.; Yaghi, O. M.; Somorjai, G. A., *Nano Lett.* **2014,** *14*, 5979.

(10) Trickett, C. A.; Gagnon, K. J.; Lee, S.; Gándara, F.; Bürgi, H. B.; Yaghi, O. M., *Angew. Chem. Int. Ed.* **2015,** *54*, 11162.

(11) Frisch, M. J.; Trucks, G. W.; Schlegel, H. B.; Scuseria, G. E.; Robb, M. A.; Cheeseman, J. R.; Scalmani, G.; Barone, V.; Petersson, G. A.; Nakatsuji, H.; Li, X.; Caricato, M.; Marenich, A. V.; Bloino, J.; Janesko, B. G.; Gomperts, R.; Mennucci, B.; Hratchian, H. P.; Ortiz, J. V.; Izmaylov, A. F.; Sonnenberg, J. L.; Williams; Ding, F.; Lipparini, F.; Egidi, F.; Goings, J.; Peng, B.; Petrone, A.; Henderson, T.; Ranasinghe, D.; Zakrzewski, V. G.; Gao, J.; Rega, N.; Zheng, G.; Liang, W.; Hada, M.; Ehara, M.; Toyota, K.; Fukuda, R.; Hasegawa, J.; Ishida, M.; Nakajima, T.; Honda, Y.; Kitao, O.; Nakai, H.; Vreven, T.; Throssell, K.; Montgomery Jr., J. A.; Peralta, J. E.; Ogliaro, F.; Bearpark, M. J.; Heyd, J. J.; Brothers, E. N.; Kudin, K. N.; Staroverov, V. N.; Keith, T. A.; Kobayashi, R.; Normand, J.; Raghavachari, K.; Rendell, A. P.; Burant, J. C.; Iyengar, S. S.; Tomasi, J.; Cossi, M.; Millam, J. M.; Klene, M.; Adamo, C.; Cammi, R.; Ochterski, J. W.; Martin, R. L.; Morokuma, K.; Farkas, O.; Foresman, J. B.; Fox, D. J. *Gaussian 16 Rev. A.03*, Wallingford, CT, 2016.

(12) (a) Valenzano, L.; Civalleri, B.; Chavan, S.; Bordiga, S.; Nilsen, M. H.; Jakobsen, S.; Lillerud, K. P.; Lamberti, C., *Chem. Mater.* **2011,** *23*, 1700; (b) Taddei, M., *Coord. Chem. Rev.* **2017,** *343*, 1.

(13) Yang, D.; Ortuño, M. A.; Bernales, V.; Cramer, C. J.; Gagliardi, L.; Gates, B. C., *J. Am. Chem. Soc.* **2018,** *140*, 3751.

(14) Avgouropoulos, G.; Ioannides, T., *Appl. Catal., A* **2003,** *244*, 155.

(15) (a) Xu, F.; Mudiyanselage, K.; Baber, A. E.; Soldemo, M.; Weissenrieder, J.; White, M. G.; Stacchiola, D. J., *J. Phys. Chem. C* **2014,** *118*, 15902; (b) Gamarra, D.; Munuera, G.; Hungría, A.; Fernández-García, M.; Conesa, J.; Midgley, P.; Wang, X.; Hanson, J.; Rodríguez, J.; Martínez-Arias, A., *J. Phys. Chem. C* **2007,** *111*, 11026.

(16) Groothaert, M. H.; van Bokhoven, J. A.; Battiston, A. A.; Weckhuysen, B. M.; Schoonheydt, R. A., *J. Am. Chem. Soc.* **2003,** *125*, 7629.

Chapter 4

Bioinspired Metal–Organic Framework Catalyst for Selective Methane Oxidation to Methanol

4.1 Introduction

Selective methane oxidation to methanol represents an important challenge in catalysis due to the difficulty in the activation of the strong C–H bond of methane (bond dissociation energy = 104 kcal mol^{-1}), which gives rise to both selectivity and activity problems.[1] Finding a solution to this impediment will be a key toward the direct synthesis of methanol from methane, which is the major component of a highly abundant natural gas.[2] In nature, particulate methane monooxygenase (pMMO) is an effective catalyst for the oxidation of methane to methanol.[3] Extensive studies on the pMMO suggest that the active sites are composed of copper complexes coordinated to histidines although the nuclearity and the definitive structures remain debated.[3-4]

Inspired by pMMO, molecular complexes have utilized the tunability of ligand design in pursuit of duplicating the structure and reactivity in a synthetic system. A library of compounds with various copper–oxygen complexes have been discovered including but not limited to Cu_2O_2 [*trans*-1,2-peroxo, μ-η^2:η^2-peroxo and bis(μ-oxo)dicopper cores] and Cu_2O [mono(μ-oxo) dicopper core] along with their spectroscopic fingerprints.[5] Despite such vast library of compounds, the reactivity of this class of catalysts is generally limited to substrates with weak C–H bonds due to the limited thermal stability.[6] At elevated temperatures, these compounds are susceptible to decomposition via ligand oxidation and thus the loss of catalytically active copper–oxygen cores.[7] Although there exist synthetic catalysts capable of partial methane oxidation which is Cu-exchanged zeolites, the diversity of the active sites are limited to mono(μ-oxo)dicopper and tris(μ-oxo)tricopper cores.[1c,1e,8] These catalysts typically operate in step-wise treatments for partial methane oxidation: (1) catalyst oxidation, (2) methane activation and (3) methanol extraction, proceeding at different reaction temperatures which can be troublesome for a streamlined catalytic process.

The active sites of metalloenzymes are typically enclosed in a pocket for environmental control, hydrogen bonding, ion transport or controlling the reaction to prevent self-destruction.[9] We envisaged that metal–organic frameworks (MOFs)[10] can serve as a scaffold akin to the polypeptide chains in enzymes whose arrangement of secondary and tertiary structures can be accomplished by judicious choice of structure and topology of MOFs.[11] The metal binding ligands bearing an imidazole unit in the copper active site of pMMO can be mirrored in a synthetic system by post-synthetic modification of MOFs.[12] Once these metal-binding ligands are in place, metalation with the desired configuration can be accomplished.[13]

Here, we demonstrate how a MOF can be used as a backbone for the creation of a mimic of an enzyme active site by installing biologically relevant imidazole moieties, then subsequently metalating these ligands to incorporate reactive copper–oxygen complexes within the framework.

From the structural analysis of a number of MOFs, MOF-808, $Zr_6O_4(OH)_4(BTC)_2(HCOO)_5(H_2O)_1(OH)_1$,[14] was selected as this MOF possesses the chemical and geometric parameters for post-synthetic modifications to create the active sites approximating pMMO. The resulting catalysts are capable of highly selective oxidation of methane to methanol under isothermal conditions. We identified the structure of the active sites using a combination of spectroscopies and density functional theory (DFT) calculations.

4.2 Experimental Section

Chemicals. All chemicals unless noted were obtained from Sigma-Aldrich. Acetone and acetonitrile (HPLC) were purchased from Fischer Scientific. Formic acid (98%) was obtained from EMD Millipore Chemicals. These chemicals were used without further purification.

Analytical techniques. Powder X-ray diffraction patterns (PXRD) were recorded using a Bruker D8 Advance diffractometer (Göbel-mirror monochromated Cu Kα radiation $\lambda = 1.54056$ Å). Single crystal X-ray diffraction data were collected using synchrotron radiation on beamline 11.3.1 (currently 12.2.1) at the Advanced Light Source (ALS) at Lawrence Berkeley National Lab (LBNL). Beamline 11.3.1 is equipped with a PHOTON-II CMOS detector operating in shutterless mode, and the radiation is monochromated using silicon (111). The amounts of Cu in the samples were analyzed by an ICP–OES spectroscope (Optima 7000 DV, Perkin Elmer). The samples (~5 mg) were digested in a solution mixture of nitric acid (0.5 mL), hydrochloric acid (1.5 mL) and hydrofluoric acid (0.1 mL) in 70 °C water bath for an hour. The resulting solutions were diluted with milliQ water to 10 mL before the measurement. Elemental microanalyses (EA) were performed in the Microanalytical Laboratory at the College of Chemistry, UC Berkeley using a Perkin Elmer 2400 Series II CHNS elemental analyzer. Solution ^1H NMR spectra of digested samples were acquired on a Bruker AVB-400 (400 MHz) spectrometer at 297–300 K. Samples of MOFs (~5 mg) were digested and dissolved by sonication in a mixture of DMSO-d_6 (560 μL), hydrofluoric acid 48% (20 μL) and D_2O (20 μL). Samples of MOFs containing Cu (~5 mg) were digested and dissolved by sonication in a mixture of DMSO-*d6* (500 μL), hydrofluoric acid 48 wt. % (20 μL), deuterium chloride (50 μL) and D_2O (20 μL). We note that the quantification of samples containing Cu can be inaccurate due to the paramagnetic nature of Cu(II). Gas adsorption analyses were performed on a Quantachrome Quadrasorb-SI automatic volumetric gas adsorption analyzer. A liquid nitrogen bath (77 K), ultra-high purity grade N_2 and He (99.999%, Praxair) were used for the measurements. The samples were prepared and measured after evacuating at 150 °C for 12 h. Pore size distribution histograms were calculated using the DFT method in the QuadraWin software using a carbon slit/cylindr./sphere pore QSDFT model on the adsorption branch of the N_2 adsorption isotherm at 77 K. Thermal gravimetric analysis (TGA) was performed using a TA Instruments Q500 thermal gravimetric analyzer under nitrogen flow and a heating rate of 5 °C min^{-1}. Scanning electron microscope (SEM) images were obtained using a Zeiss Gemini Ultra-55 analytical scanning electron microscope. The samples were prepared by dispersing MOF samples in acetone by sonication and the samples were drop-casted on a silicon wafer.

Synthesis of MOFs:

MOF-808. MOF-808 was synthesized following the reported protocol.[15] In a 100-mL media bottle, 1,3,5-benzenetricarboxylic acid (210 mg) and $ZrOCl_2·8H_2O$ (970 mg) were dissolved in a solution containing DMF (30 mL) and formic acid (30 mL). The bottle was sealed and heated in a 100 °C isothermal oven for a day. White powder was collected by centrifugation (8,000 rpm, 3 min), washed with DMF 3 times (60 mL × 3) over a 24 h period and with acetone 3 times (60 mL × 3) over a 24 h period. Finally, MOF-808 was dried under dynamic vacuum overnight at room temperature. EA of activated sample: Calcd for $Zr_6O_4(OH)_4(C_9H_3O_6)_2(HCOO)_5(H_2O)_1(OH)_1$ $(C_3H_7NO)_{0.5}$: C, 21.17; H, 1.56; N, 0.50; Found: C, 21.18; H, 1.37; N, 0.44.

MOF-808-His. A saturated solution of l-histidine was prepared by dissolving *l*-histidine (93 mg) in water (8 mL) in 20 mL vial in an 85 °C isothermal oven. MOF-808 (160 mg) was suspended by sonication in the saturation solution of *l*-histidine and the suspension was heated in an 85 °C isothermal oven overnight. The reaction was allowed to cool to about 50 °C while the supernatant was carefully removed prior to the recrystallization of *l*-histidine. White powder was collected by centrifugation (8,000 rpm, 3 min), washed 5 times with water (10 mL × 5) over 3 days and with acetone 5 times (10 mL × 5) over 3 days. Finally, MOF-808-His was dried under dynamic vacuum overnight at room temperature. EA of activated sample: Calcd for $Zr_6O_4(OH)_4(C_9H_3O_6)_2(C_6H_8N_3O_2)_{3.5}(OH)_{2.5}(H_2O)_{2.5}$: C, 27.22; H, 2.67; N, 8.55; Found: C, 28.03; H, 3.05; N, 8.27.

MOF-808-Iza. A solution of 4-imidazole acrylic acid was prepared by dissolving 4-imidazole acrylic acid (6 g) in DMSO (70 mL) in a 100-mL bottle in a 100 °C isothermal oven. MOF-808 (1 g) was suspended by sonication in the solution of 4-imidazole acrylic acid and the suspension was heated in a 100 °C isothermal oven overnight. The reaction was allowed to cool to room temperature. White powder was collected by centrifugation (8,000 rpm, 3 min), washed with DMSO 5 times (80 mL × 5) over 3 days and with acetone (80 mL × 5) over 3 days. Finally, MOF-808-Iza was dried under dynamic vacuum overnight at room temperature. EA of activated sample: Calcd for $Zr_6O_4(OH)_4(C_9H_3O_6)_2(C_6H_5N_2O_2)_{3.7}(HCOO)_{1.6}(OH)_{0.7}(H_2O)_{0.7}$: C, 29.58; H, 1.91; N, 6.11; Found: C, 27.92; H, 2.35; N, 5.40.

MOF-808-Bzz. A solution of 5-benzimidazolecarboxylic acid was prepared by dissolving 5-benzimidazolecarboxylic acid (3 g) in DMSO (100 mL) in a 250 mL bottle in a 100 °C isothermal oven. MOF-808 (0.5 g) was suspended by sonication in the solution of 5-benzimidazolecarboxylic acid and the suspension was heated in a 100 °C isothermal oven overnight. The reaction was cooled down naturally to room temperature. Brown powder was collected by centrifugation (8,000 rpm, 3 min), washed with DMSO 5 times (80 mL × 5) over 3 days and with acetone 5 times (80 mL × 5) over 3 days. Finally, MOF-808-Bzz was dried under dynamic vacuum overnight at room temperature. EA of activated sample: Cald for $Zr_6O_4(OH)_4(C_9H_3O_6)_2(C_8H_5N_2O_2)_{3.4}(HCOO)_{1.6}(OH)_1(H_2O)_1$: C, 32.15; H, 1.82; N, 5.45; O, 29.28; Zr, 31.30; Found: C, 31.07; H, 2.61; N, 5.30.

MOF-808-His-Cu. A solution of CuI (99.999% metals basis, 47.8 mg) in ACN (7.5 mL) was added to a suspension of MOF-808-His (75 mg) in ACN (1.9 mL) in a 20 mL vial while stirring (500 rpm) at room temperature under ambient conditions. The vial was sealed and the mixture was stirred 3 for days at room temperature. Green powder was collected by centrifugation (8,000 rpm, 3 min) and washed with ACN 5 times (15 mL × 5) over 3 days. Finally, MOF-808-His-Cu was dried under dynamic vacuum overnight at room temperature. ICP analysis: Cu/Zr molar ratio = 0.8.

MOF-808-Iza-Cu. A solution of CuI (99.999% metals basis, 76.5 mg) in ACN (12 mL) was added to a suspension of MOF-808-Iza (75 mg) in ACN (1.9 mL) in a 20 mL vial while stirring (500 rpm) at room temperature under ambient conditions. The vial was sealed and the mixture was stirred for 3 days at room temperature. Green powder was collected by centrifugation (8,000 rpm, 3 min) and washed with ACN 5 times (15 mL × 5) over 3 days. Finally, MOF-808-Iza-Cu was dried under dynamic vacuum overnight at room temperature. ICP analysis: Cu/Zr molar ratio = 1.0.

MOF-808-Bzz-Cu. A solution of CuI (99.999% metals basis, 81.6 mg) in ACN (12.8 mL) was added to a suspension of MOF-808-Bzz (75 mg) in ACN (1.9 mL) in a 20 mL vial while stirring (500 rpm) at room temperature under ambient conditions. The vial was sealed and the mixture was stirred for 3 days at room temperature. Brown powder was collected by centrifugation (8,000 rpm, 3 min) and washed with ACN 5 times (15 mL × 5) over 3 days. Finally, MOF-808-Bzz-Cu was dried under dynamic vacuum overnight at room temperature. ICP analysis: Cu/Zr molar ratio = 1.2.

MOF-808-Cu (control). A solution of CuI (99.999% metals basis, 81.6 mg) in ACN (12.8 mL) was added to a suspension of MOF-808 (75 mg) in ACN (1.9 mL) in a 20 mL vial while stirring (500 rpm) at room temperature under ambient conditions. The vial was sealed and the reaction was stirred for 3 days at room temperature. Brown powder was collected by centrifugation (8,000 rpm, 3 min) and washed with ACN 5 times (15 mL × 5) over 3 days. Finally, MOF-808-Bzz-Cu was dried under dynamic vacuum overnight at room temperature. ICP analysis: Cu/Zr molar ratio = 1.2.

Single crystals of MOF-808. To reduce nucleation of MOF single-crystals on vial surface, the inner surface of glass vials was rinsed with Sigmacote® siliconizing reagent, washed three times with acetone, and dried in a drying oven before use. Single crystals of MOF-808 was prepared following the reported procedure.[14] $ZrOCl_2 \cdot 8H_2O$ (0.032 g, 0.10 mmol) and H_3BTC (0.022 g, 0.10 mmol) were dissolved separately in 2 ml DMF, then both solutions were combined in a 20 mL scintillation vial and 4 ml formic acid was added. This mixture was then placed in a 100 °C isothermal oven for three days. The crystals were washed with DMF 5 times (10 mL × 5) over 3 days.

Single crystals of MOF-808-His. Approximately 5 mg of single crystals of MOF-808 was washed with DI H_2O 5 times (2 mL × 5) in a 4 mL scintillation vial. After which, a saturated solution of *l*-histidine prepared by dissolving *l*-histidine (23.25 mg) in water (2 mL) was added to the crystals. This mixture was heated in an 85 °C isothermal oven overnight. The reaction was allowed to cool to about 50 °C while the supernatant was carefully removed prior to recrystallization of *l*-histidine. The crystals were washed 5 times with water (2 mL × 5) over 3 days.

Single crystals of MOF-808-Iza. Approximately 5 mg of single crystals of MOF-808 was washed with DMSO 5 times (2 mL × 5) in a 4 mL scintillation vial. After which, a saturated solution of 4-imidazoleacrylic acid prepared by dissolving 4-imidazoleacrylic acid (171 mg) in DMSO (2 mL) was added to the crystals. This mixture was heated in a 100 °C isothermal oven overnight. The reaction was allowed to cool to room temperature. The crystals were washed 5 times with DMSO (2 mL × 5) over 3 days.

Single crystals of MOF-808-Bzz. Approximately 5 mg of single crystals of MOF-808 was washed with DMSO 5 times (2 mL × 5) in a 4 mL scintillation vial. After which, a saturated solution of 5-benzimidazolecarboxylic acid prepared by dissolving 5-benzimidazolecarboxylic acid (60 mg) in DMSO (2 mL) was added to the crystals. This mixture was heated in a 100 °C isothermal oven overnight. The reaction was allowed to cool to room temperature. The crystals were washed 5 times with DMSO (2 mL × 5) over 3 days.

Catalysis:

The catalytic testing was performed using a custom-designed continuous flow tubular reactor (Parr Instrument Co.). Mass flow controllers were calibrated using ADM 1000 flow meter (Agilent Technologies) and ultrahigh purity He, CH_4 (Research 5.0 Grade, Airgas), and 3% N_2O/He (Primary Standard Grade, Praxair) were flowed into the 30 cm long quarter inch 316 stainless steel reactor. Catalysts (100 mg) were used after sieving in the range of 100-250 µm. The catalyst was placed in the middle of the reactor tube, delimited by a layer of purified glass wool and a layer of quartz sand (50-70 mesh) at each end. Pretreatment of catalysts was conducted under 30 sccm He at 150 °C (3 °C/min) for 1 h. For the oxidation of catalysts, we changed the gas to 3% N_2O/He flow (30 sccm) and kept it for 2 h. After purging with 30 sccm of He for 30 min, CH_4 (30 sccm) was flowed for 1 h. After purging with 50 sccm of He for 1 h, we open the valve and flowed He through to the water saturator cooled and kept the temperature at 24 °C using water bath (3% steam/He, 30 sccm). All lines are heated at 120 °C to prevent condensation. The outstream was analyzed by gas chromatograph (Model: GC-2014, Shimadzu Co.). The measurement starts 3 min after opening the valve to the water saturator. The reactants and products were separated using HayeSep R 80/100 stainless steel packed column (12 ft, 1/8 in OD, 2mm ID). The water and CO_2 were monitored using a thermal conductivity detector and methanol was monitored using a flame ionization detector.

UV-Vis diffuse reflectance spectroscopy (DRS) spectroscopy:

The UV-Vis diffuse reflectance spectroscopy (DRS) spectra of MOF-808-L, MOF-808-L-Cu and MOF-808-L-Cu were collected using Shimadzu model UV-2450 spectrometer equipped with an integrating sphere model ISR-2200. The MOF-808-L-Cu samples treated under 3% N_2O/He at 150 °C for 1 h in a 316 stainless steel reactor was cooled down with He purge and is closed with Swagelok valve, moved to an argon-filled glovebox, and transferred into the home-built stainless steel vacuum cell for UV-Vis diffuse reflectance experiments.[16] To illustrate the effect of metalation with Cu in the presence of dioxygen and reaction with N_2O, the spectra of MOF-808-L-Cu and MOF-808-L-Cu were subtracted using their corresponding MOF-808-L spectra.

Resonance Raman spectroscopy:

In an argon-filled glovebox, a solution of CuI dissolved in anhydrous ACN was added to a suspension of MOF-808-L in anhydrous ACN in a 1.5-mL GC autosampler vial equipped with PTFE/rubber septum. Specific stoichiometries are described below. The vial was sealed and removed from the glovebox. Either $^{16}O_2$ (Praxair, 99.999%) or $^{18}O_2$ (Aldrich, 99 atom%) was bubbled through the solution using a needle pierced through the septum at a rate of ca. 30 mL min^{-1} for 10 min. The suspension was allowed to react at room temperature for 3 days. The solid was collected by centrifugation, dried overnight, transferred to an Argon-filled glovebox and washed with anhydrous ACN 5 times (2 mL × 5) over 3 days. The sample was dried under dynamic vacuum overnight at room temperature and the dried solid was transferred to the glovebox. The sample was loaded into a thin-wall quartz capillary tube and sealed with epoxy glue.

MOF-808-His-Cu: a solution of CuI (3.70 mg) in anhydrous ACN (0.58 mL) was added to a suspension of MOF-808-His (5.77 mg) in anhydrous ACN (0.14 mL).

MOF-808-Iza-Cu: a solution of CuI (5.90 mg) in anhydrous ACN (0.92 mL) was added to a suspension of MOF-808-Iza (5.77 mg) in anhydrous ACN (0.14 mL).

MOF-808-Bzz-Cu: a solution of CuI (6.25 mg) in anhydrous ACN (0.98 mL) was added to a suspension of MOF-808-Bzz (5.77 mg) in anhydrous ACN (0.14 mL).

All spectra were collected using the 407 nm light with the power density of 3.1 W/cm^2. The Raman scattering was collected using a Spex 1401 double grating spectrograph and liquid nitrogen cooled Roper Scientific LN/CCD 1100 controlled by a ST133 controller. The measured Raman shifts were calibrated by using Raman peaks of cyclohexane.

Density Functional Theory Calculations:

Single crystal structure of MOF-808 was used as a model and formate molecules were replaced with either *l*-histidine, 4-imidazoleacrylic acid or 5-benzimidazolecarboxylic acid. Cu atoms were allowed to coordinate to N atoms of metal binding ligand and dioxygen to form Cu-O complexes. We assumed that Cu is 4-coordinated as they are the most common among bis(μ-oxo) dicopper complexes.[5b] From ^1H NMR analysis, we observed the resonance peaks of DMF but not that of acetonitrile which was used during the synthesis. Thus, the fourth neutral ligand is likely to be terminal water or DMF. We used water in our model for simplicity. To reduce computational cost, the Cu-O complexes along with their metal-binding ligands were extracted from the models and carboxylate groups of metal-binding ligands were neutralized with protons. The clusters were geometrically optimized at the density functional theory (DFT) in gas phase using spin-unrestricted B3LYP functional[17] as implemented in Gaussian 16 (revision A03) without symmetry constraints.[18] The 6-31G basis sets were employed for C and H atoms while 6-311G(d) basis sets were used for Cu, N and O atoms. Numerical integrations were performed on an ultrafine grid. During geometry optimization, O atoms of carboxylate groups of the metal binding ligands were frozen to simulate the rigidity of the framework. Minima of all geometry-optimized structures were verified by having no imaginary frequency found from analytical frequency calculation performed at the same level of theory.

X-ray Absorption Spectroscopy (XAS):

N K-edge X-ray absorption spectra were collected at beamline 8.0.1 which is an undulator beamline with energy ranges of 80-1200 eV of the Advanced Light Source (ALS) at Lawrence Berkeley National Laboratory (LBNL). Its spherical gratings monochromator delivers 1012 photons/second with linear polarization with a resolving power up to 6000. The experimental energy resolution is better than 0.15 eV. Experiments were performed at room temperature. All the spectra were collected in both total-electron-yield (TEY) and total-fluorescence-yield (TFY) modes simultaneously, corresponding to a probe depth of about 10 nm and 100 nm, respectively. We present spectra of TFY modes in this work as bulk measurements are preferred for our samples. The MOF-808-L-Cu samples was cooled down with He purge after each gas treatment in a 316-stainless steel reactor. The reactor containing the sample was sealed with a Swagelok valve and moved to an argon-filled glovebox (H_2O and O_2 levels <1 ppm). The sample was unloaded and pressed onto an indium foil using a hand press. Thereafter these samples were transferred into an ultrahigh vacuum XAS end station with low 10^{-9} torr through our dedicated sample transfer kit to avoid air exposure. Energies are aligned by periodically collecting Ti L-edge spectra of a TiO_2 (anatase) reference for N K-edge. The XAS spectra were recorded over a wide energy range covering energies well below and above sample absorptions. The normalization was performed following the established procedure: 1) I_0-normalization: the sample signal is divided by the incident intensity measured from the sample drain current from a freshly coated gold mesh inserted into the beam path before the X-rays can impinge on the sample. 2) A linear, sloping background is removed by fitting a line to the flat low energy region of the XAS spectrum, i.e., at energies below any absorption peaks. 3) The spectrum is normalized by setting the flat low energy region to zero and the post edge to unity (unit edge jump).

Cu K-edge X-ray absorption spectroscopy data were collected at the Advanced Light Source (ALS) bending-magnet beamline 10.3.2 (2.4−17 keV) with the storage ring operating at 500 mA and 1.9 GeV using a two Si(111) crystal monochromator and adjustable pre-monochromator slits.[19] All data were collected at room temperature (22 °C) in fluorescence mode at the Cu K edge (8980.48 eV). A bulk Cu foil was measured in transmission mode every 24 hours for calibration purposes. The incoming X-ray intensity (I_o) was measured in an ion chamber and the fluorescence emission with a seven element LN_2 cooled Ge solid-state detector (Canberra) using XIA electronics. The MOF-808-L-Cu samples were cooled down with He purge after each gas treatment in a 316-stainless steel reactor. The reactor containing the sample was sealed with a Swagelok valve and moved to an argon-filled glovebox (H_2O and O_2 levels <1 ppm). The sample was unloaded and sealed with Kapton tape for ex-situ measurement. Cu K-edge XANES spectra were recorded in fluorescence mode by continuously scanning the Si (1 1 1) monochromator (Quick XAS mode) from 8,880 to 9,020 eV, with 0.3 eV steps in the XANES region. All data were processed using the LabVIEW custom BL 10.3.2 software to perform dead time correction, energy calibration, and glitch removal which detail procedure is described elsewhere.[20] XANES spectra were processed with Athena software to find first derivative peak (E_0), post-edge normalization, align data, and merge normalized (E). EXAFS spectra were recorded up to 565 eV above the edge (8,880−9,545 eV, i.e., up to $k \approx 12$ Å^{-1}) at least 11 times and are merged. EXAFS spectra of samples were reduced with k^1-, k^2-, and k^3-weighting, out to $k = 10$ Å^{-1}, and analyzed via shell-by-shell fitting using the FEFF6l code and the Artemis software where it yields minima invariances.[21]

4.3 Results and Discussion

Synthesis of the catalysts. MOF-808 is composed of 12-connected cuboctahedron $Zr_6O_4(OH)_4(\text{-}COO)_{12}$ secondary building units (SBUs) connected to the other SBUs through six benzenetricarboxylates (H_3BTC) with three above and three below the ring of formates to form tetrahedral cages. These cages are linked up to form an adamantane-shaped pore with formate, water and hydroxide molecules completing the coordination spheres of Zr residing the pseudohexagonal pore openings (Figure 4.1). Replacement of these formate molecules, water or hydroxide molecules with imidazole-based ligands bearing carboxylic acid functionality will result in imidazole units localizing in the center of the pores. These ligands are spatially positioned suitably for stabilizing copper–oxygen species in the framework (Figure 4.2).

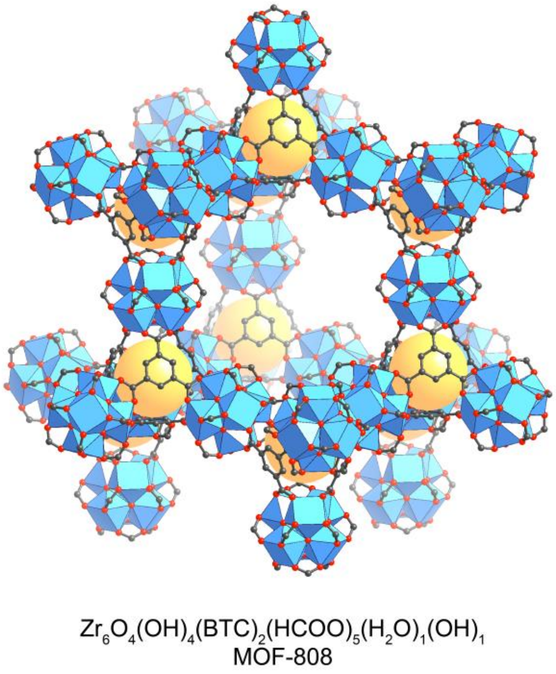

Figure 4.1. Structure of MOF-808. Atom labeling scheme: C, black; O, red; N, green; Cu, orange; Zr, blue polyhedra. H atoms are omitted for clarity.

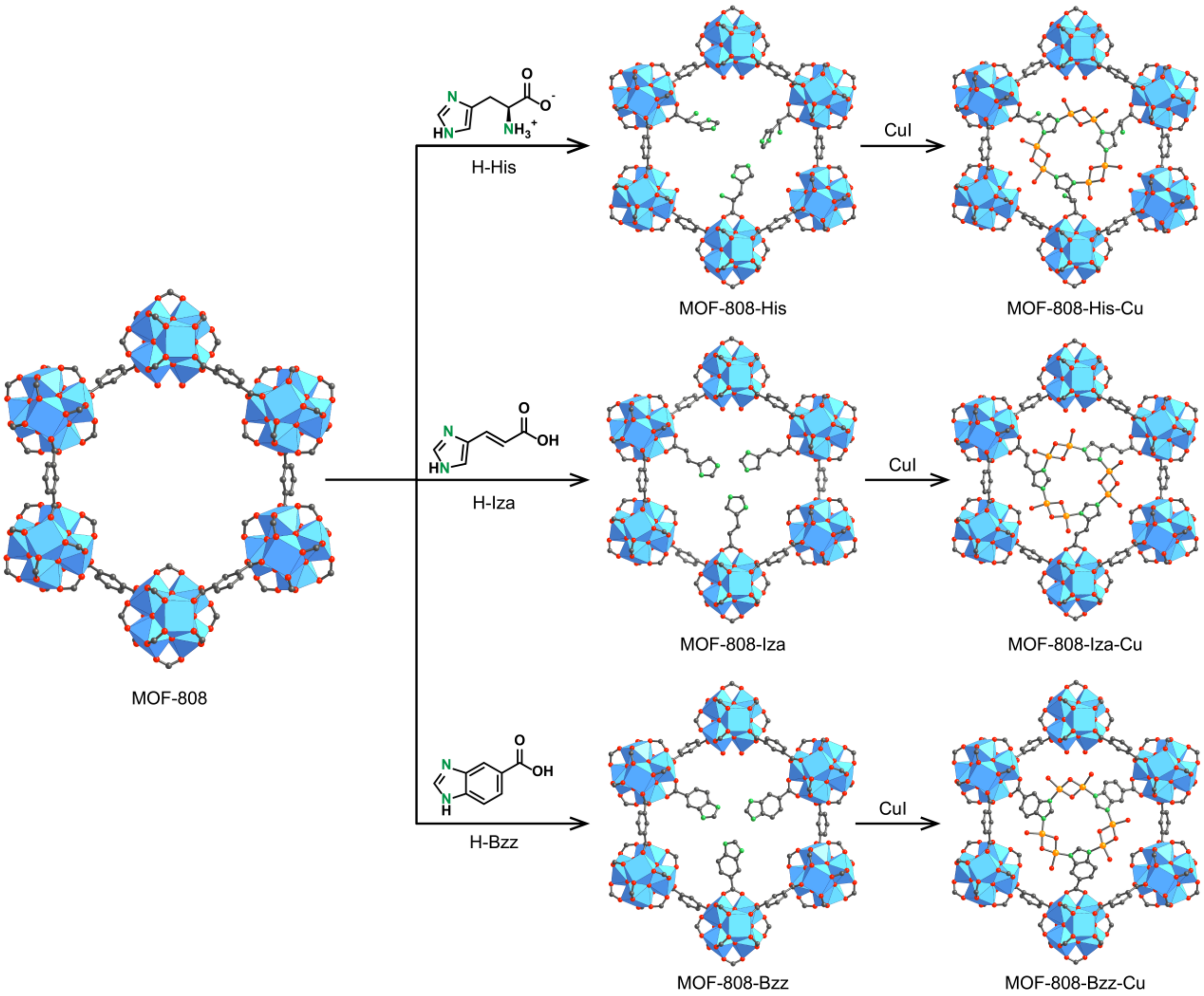

Figure 4.2. Synthesis of the catalysts comprising the replacement of formate with imidazole-containing ligands and metalation with Cu(I). Atom labeling scheme: C, black; O, red; N, green; Cu, orange; Zr, blue polyhedra. H atoms are omitted for clarity.

Specifically, we synthesized microcrystalline MOF-808 to allow for a facile diffusion of substrates during post-synthetic modifications and catalysis.[15] We selected three different metal-binding ligands comprising biologically relevant imidazole units for incorporation into the framework to demonstrate the modularity of our system and to study the effect of how ligand rigidity influences the catalytic properties. Metal binding ligands including L-histidine (His), 4-imidazoleacrylic acid (Iza) and 5-benzimidazole acrylic acid (Bzz) were incorporated into the framework by heating MOF-808 in saturated solutions of these metal-binding ligands to produce MOF-808-L with -L being -His, -Iza and -Bzz, respectively. The successful substitution of formate with these ligands in the MOF was confirmed by ^{1}H nuclear magnetic resonance (NMR) of the digested samples. Of six available sites per chemical formula, approximately half of these were successfully exchanged with the metal binding ligands to produce MOF-808-His

$[Zr_6O_4(OH)_4(BTC)_2(His)_{3.5}(OH)_{2.5}(H_2O)_{2.5}]$, MOF-808-Iza $[Zr_6O_4(OH)_4(BTC)_2 (Iza)_{3.7}(HCOO)_{1.6} (OH)_{0.7}(H_2O)_{0.7}]$ and MOF-808-Bzz $[Zr_6O_4(OH)_4(BTC)_2(Bzz)_{3.4}(HCOO)_{1.6} (OH)_1(H_2O)_1]$. Similar procedures were performed on single crystals of MOF-808 for structural elucidation of these functionalized MOFs. Single crystal X-ray diffraction (SXRD) analysis reveals that these ligands bind to the Zr clusters in a bridging fashion with carboxylate group coordinating to Zr atoms and thus placing imidazole units in the center of the pseudohexagonal window. Metalation of these MOFs with CuI in MeCN under air at room temperature provides the catalysts, namely MOF-808-His-Cu, MOF-808-Iza-Cu and MOF-808-Bzz-Cu. Inductively coupled plasma atomic emission spectroscopy (ICP-AES) analysis performed on these catalysts indicates the Cu/Zr_6 molar ratios of 4.9, 6.0 and 7.1 for MOF-808-His-Cu, MOF-808-Iza-Cu and MOF-808-Bzz-Cu, respectively (Table 1). A control experiment was performed by metalation of MOF-808 under similar condition. Negligible incorporation of copper was observed (Cu/Zr_6 molar ratio = 0.3) suggesting the role of imidazole ligands in ligating to copper atoms. The phase purity and crystallinity of the materials after post-synthetic modifications were preserved as confirmed by powder X-ray diffraction (PXRD) analysis (Figure 4.3). The porosity of these materials was verified by N_2 adsorption-desorption isotherm measurements at 77 K with BET surface area of 385, 580, and 580 $m^2\ g^{-1}$ for MOF-808-His-Cu, MOF-808-Iza-Cu, and MOF-808-Bzz-Cu, respectively.

Table 4.1. Summary of catalysts composition.

Catalyst	L/Zr_6 molar ratio	Cu/Zr_6 molar ratio	Cu/L molar ratio
MOF-808-His-Cu	3.5	4.9	1.4
MOF-808-Iza-Cu	3.7	6	1.6
MOF-808-Bzz-Cu	3.4	7.1	2.1
MOF-808-Cu	-	0.3	-

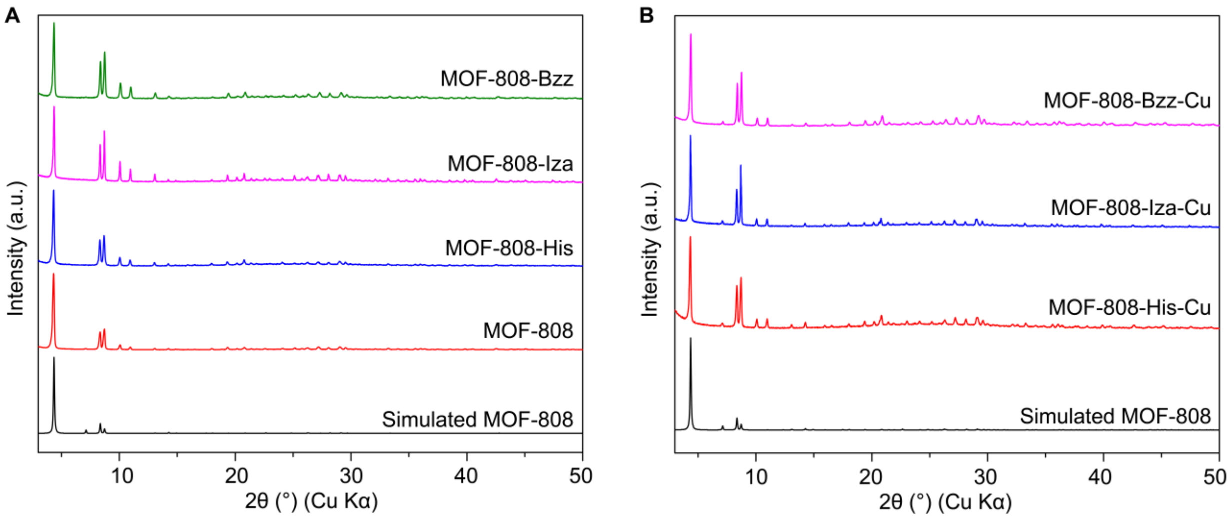

Figure 4.3. PXRD patterns of MOF-808 after the incorporation of metal-binding ligands (A) and metalation (B).

Methane oxidation. Methane oxidation was conducted with an isothermal series of treatments at 150 °C. First, 100 mg of MOF-808-L-Cu catalyst was pretreated in He flow to remove residual solvents (i.e., MeCN and water) at temperatures starting from room temperature to 150 °C at a ramping rate of 3 °C min^{-1}. After a clean background was achieved by monitoring the signals from a gas chromatograph, the catalyst was treated with 3% N_2O/He for 2 h at 150 °C followed by purging the catalyst with He for 30 min. The catalyst was subsequently exposed to a flow of CH_4 for 1 h at 150 °C for methane activation. After He purge, water was introduced in the form of 3% steam in He at 150 °C to desorb methanol. As shown in Figure 4.4, the average methanol productivity corresponds to 31.7, 61.8, and 71.8 μmol/g$_{\text{MOF-808-L-Cu}}$ for MOF-808-His-Cu, MOF-808-Iza-Cu, and MOF-808-Bzz-Cu, respectively indicating that the MOF-808-Bzz-Cu has the highest methanol productivity among three catalysts. In terms of the turnover numbers (methanol productivity per mole of copper), MOF-808-His-Cu exhibited lower activity which is more likely due to lower number of catalytically active copper–oxygen species (~43% lower turnover number), attributed to the flexibility of histidine ligand. Notably, only methanol and water were observed as products during methanol desorption at a temperature below or equal to 150 °C which is confirmed by gas chromatographs equipped with flame ionization and thermal conductivity detectors and a mass analyzer. Above this temperature, we observed increased methanol production with temperature, which is expected due to improved methanol extraction efficiency. However, CO_2 was also observed as a byproduct from the overoxidation of the methanol generated. For control experiments, we did not observe any products in the experiments performed on MOF-808-L and CuI which is Cu(I) precursor in this study.

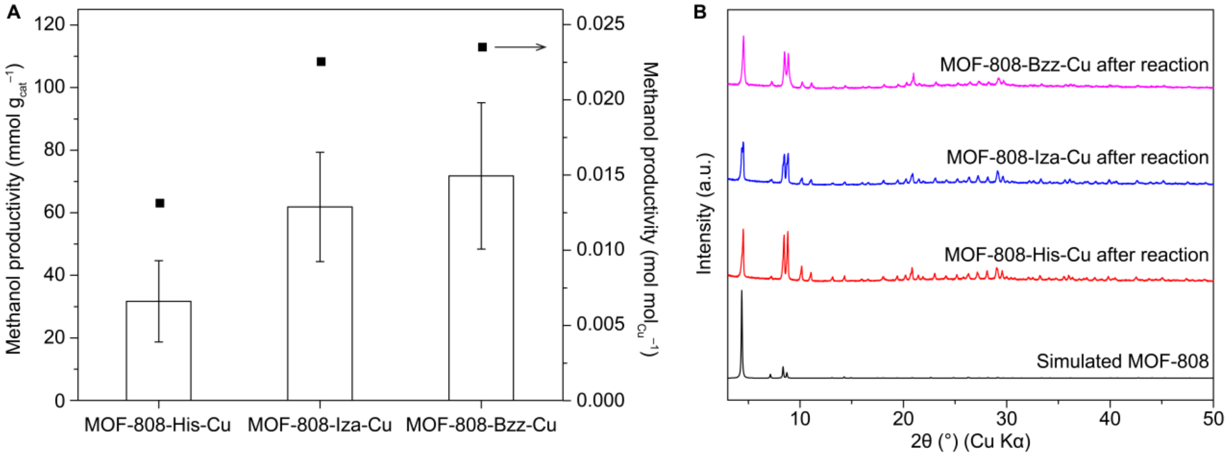

Figure 4.4. Average methanol productivities with standard errors of MOF-808-His-Cu, MOF-808-Iza-Cu and MOF-808-Bzz-Cu (A). PXRD patterns of the catalysts after the reactions (B).

We examined the structural integrity of the catalysts after the reactions. The crystallinity of the catalysts was maintained as evidenced by PXRD (Figure 4.4B). Interestingly, unlike molecular copper–oxygen complexes,[6] ligand hydroxylation was not observed from digested ^{1}H NMR of the catalysts even at 150 °C highlighting the significantly enhanced stability imposed by covalent attachment of the complexes that are geometrically constrained in the MOF.

We performed recyclability test on MOF-808-Bzz-Cu with an isothermal series of treatment at 150 °C. A drastic deactivation was observed in the second and third cycle giving 7.5 μmol/g and 0.1 μmol/g methanol productivity, respectively. After the third cycle, MOF-808-Bzz-Cu was subjected to a flow of He by increasing temperature from 150 °C to 250 °C at a ramping rate of 3 °C min^{-1} and hold for 10 min. Desorbed water was observed during this He treatment until the temperature reaches 250 °C. We then proceeded with the isothermal series of treatment at 150 °C; the catalyst showed methanol productivity of 5.4 μmol g^{-1} which is similar to the productivity obtained from the second cycle. This result indicates that the catalyst deactivation is due to water molecules strongly bound to the active site. We also performed the recyclability test of MOF-808-His-Cu. There is a 77% decrease in methanol productivity from 28 μmol g^{-1} in the first cycle to 6.3 μmol g^{-1} in the second cycle. Unlike MOF-808-Bzz-Cu, the histidine-derived catalyst still exhibits methanol productivity in the third and fourth cycle with 17% and 12% decrease per cycle. Even though there is a recyclability problem in MOF-808-L-Cu catalysts, it is noteworthy that this catalyst shows the highest reported methanol productivity at 71.8 μmol g^{-1} with an isothermal series of treatments at 150 °C with high selectivity to methanol.[22] Thanks to the modularity in our catalysts, we expect that the recyclability can be improved by varying the coordination sphere around the active sites.

Identification of the active site in MOF-808-L-Cu. To elucidate the identity of the active site of the catalysts, we synthesized single crystals of MOF-808-L-Cu catalysts following similar procedures employed for microcrystalline samples. However, the active sites of the catalysts are crystallographically disordered prohibiting an unambiguous structural characterization using SXRD analysis. We therefore employed an element- and structure-specific techniques to determine the structures of the active sites. Energy-dispersive X-ray spectroscopy (EDS) analysis of the catalysts shows a uniform distribution of Zr, N and Cu atoms throughout the crystals, thus precluding the localization of the active sites on the surface of the MOF crystals.

We carried out N K-edge X-ray absorption near edge structure (XANES), Cu K-edge X-X-ray absorption spectroscopy (XAS), UV-Vis diffuse reflectance spectroscopy (DRS) and resonance Raman spectroscopy measurements on three MOF-808-L-Cu catalysts. These catalysts show similar trends in the spectroscopic features unless otherwise noted. We therefore use MOF-808-Bzz-Cu as a representative in the following discussion. Comparison of N K-edge XANES spectra of MOF-808-Bzz and MOF-808-Bzz-Cu provides insight into the location of copper in the MOF catalysts (Figure 4.5A–4.7A). Two absorption bands at 398.8 and 400.6 eV are observed assignable to the 1s → π* transitions of the nitrogen atoms in C-NH-C and C-N-C of imidazole ring, respectively.[23] After the metalation, two absorption peaks are shifted and changed in intensity indicating that Cu atoms are coordinated to N atoms that are part of the imidazole units. Ex-situ N K-edge XANES measurements of the samples after each step of the series of treatments show that two absorption bands remain similar. This indicates that the Cu atoms are coordinated to N atoms throughout the catalytic process.

Ex-situ Cu K-edge XANES measurements were performed to probe the oxidation states of copper during catalysis (Figure 4.5B–4.7B). Four characteristic peaks located at 8979, 8984, 8989, and 8998 eV are observed. In the pre-edge region (inset of Figure 4.5B), we observed a weak absorption peak around 8979 eV corresponding to a dipole-forbidden Cu(II) 1s → 3d electronic transition.[24] The shoulder peak at 8989 eV is attributable to Cu(II) 1s → 4p + L shakedown transition.[25] Cu(I) 1s → 4p + L shakedown feature is observed at 8984 eV.[26] This data suggests that the catalysts are composed of a mixture of Cu(I) and Cu(II) species. The spectrum recorded after 3% N_2O/He at 150 °C exhibits oxidation of Cu(I) to Cu(II) which is indicative of the formation of the active copper–oxygen species. After the reaction with methane at 150 °C, the peak intensity of Cu(I) at 8984 eV increased while white line intensity decreased suggesting the reduction of Cu(II) to Cu(I). This reduction can be described by the formation of oxidation product (i.e., methoxy) where oxygen atoms of the active copper-oxygen species reacted with methane.[1g] After methanol desorption was performed by flowing 3% steam/He at 150 °C into the catalyst, the white line intensity increased accompanied by decreasing intensity of the peak of Cu(I) at 8984 eV. This redox behavior of copper observed from Cu K-edge XANES further proves that the copper active site in our catalysts participates in methane oxidation to methanol. MOF-808-Iza-Cu also shows distinctive changes in the oxidation state of copper following the same trend through the course of the catalytic process as described for MOF-808-Bzz-Cu. MOF-808-His-Cu, however, shows minor intensity changes, consistent with the lower methanol productivity as previously described.

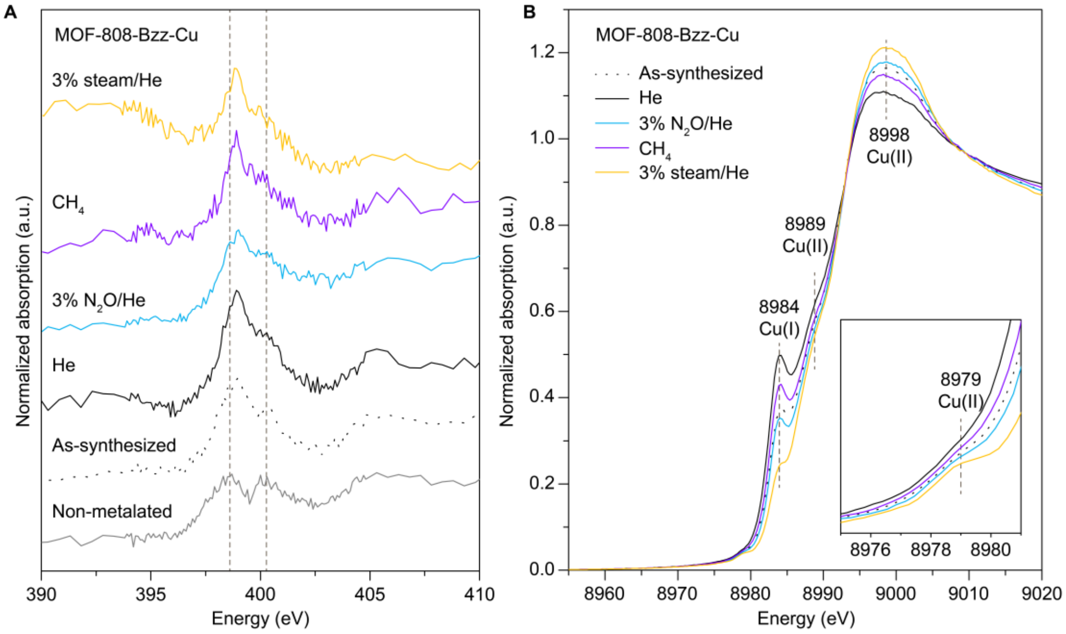

Figure 4.5. (A) Ex-situ N K-edge XANES spectra of MOF-808-Bzz, as-synthesized MOF-808-Bzz-Cu and MOF-808-Bzz-Cu after the reactions with He, 3% N_2O/He, CH_4 and 3% steam/He. (B) Ex-situ Cu K-edge XANES spectra of MOF-808-Bzz-Cu after the reactions with He, 3%N_2O/He, CH_4 and 3% steam/He.

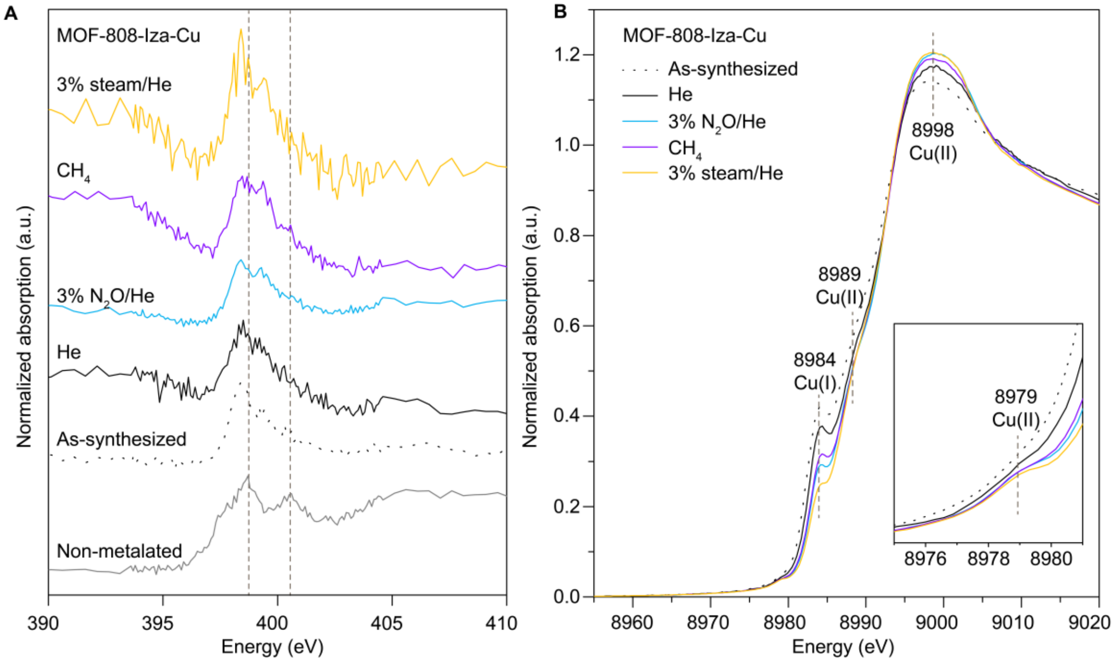

Figure 4.6. (A) Ex-situ N K-edge XANES spectra of MOF-808-Iza, as-synthesized MOF-808-Iza-Cu and MOF-808-Iza-Cu after the reactions with He, 3% N_2O/He, CH_4 and 3% steam/He. (B) Ex-situ Cu K-edge XANES spectra of MOF-808-Iza-Cu after the reactions with He, 3%N_2O/He, CH_4 and 3% steam/He.

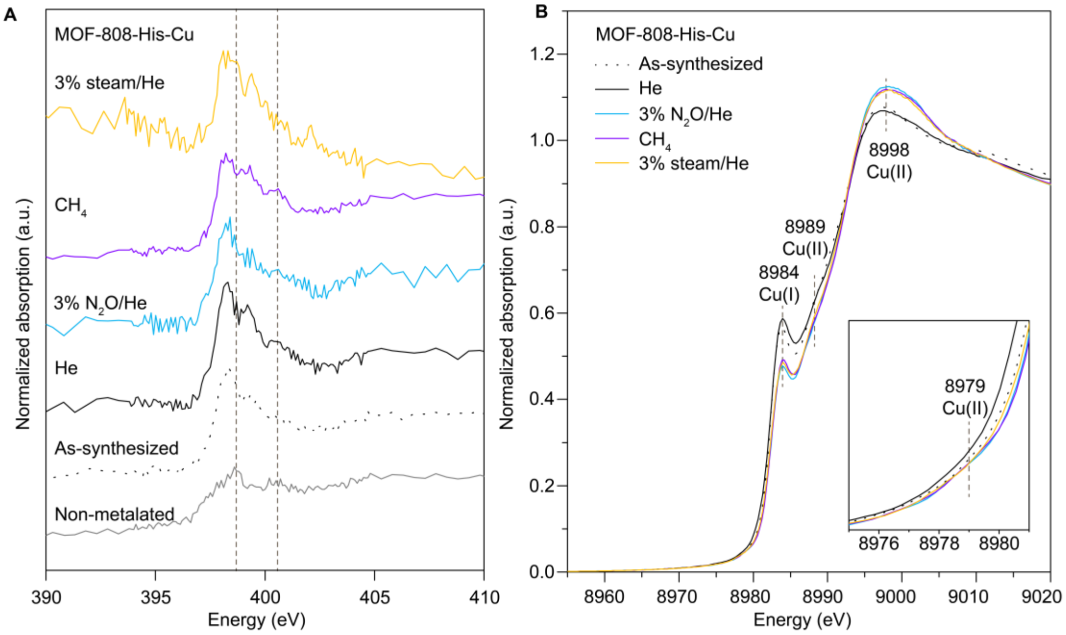

Figure 4.7. (A) Ex-situ N K-edge XANES spectra of MOF-808-His, as-synthesized MOF-808-His-Cu and MOF-808-His-Cu after the reactions with He, 3% N_2O/He, CH_4 and 3% steam/He. (B) Ex-situ Cu K-edge XANES spectra of MOF-808-His-Cu after the reactions with He, 3%N_2O/He, CH_4 and 3% steam/He.

To gain more information about the active copper–oxygen species, UV-Vis DRS and resonance Raman spectroscopy measurements were performed. Background subtracted UV-Vis DRS spectra of the as-synthesized samples show the absorption band centered at ~400 nm. After 3% N_2O/He treatment at 150 °C, we observed the increase of this absorption band which corresponds to oxygen-to-metal charge-transfer transition.[27]

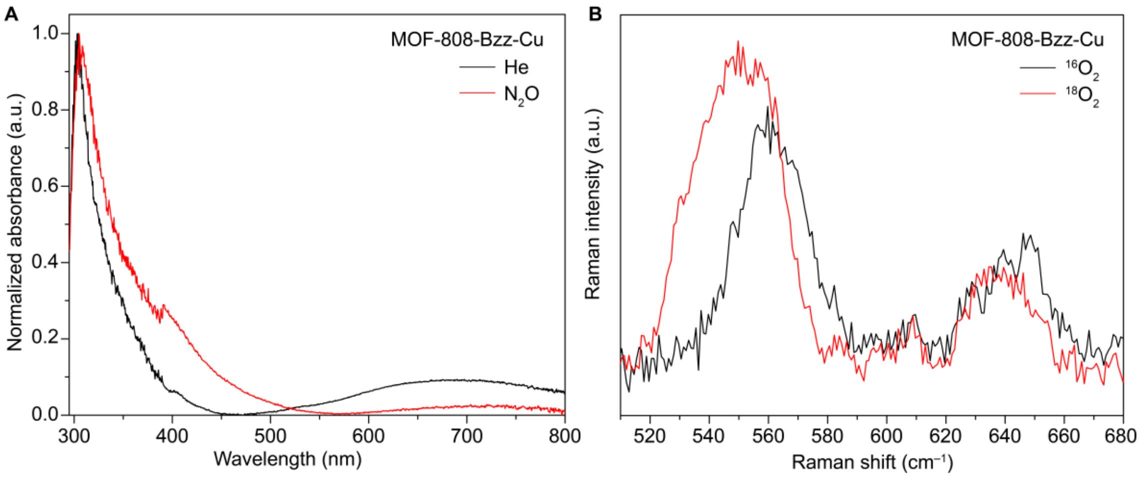

Figure 4.8. UV-Vis DRS spectra after He pretreatment and after reaction with N_2O (A) and (B) Resonance Raman spectra excited at 407 nm of MOF-808-Bzz-Cu.

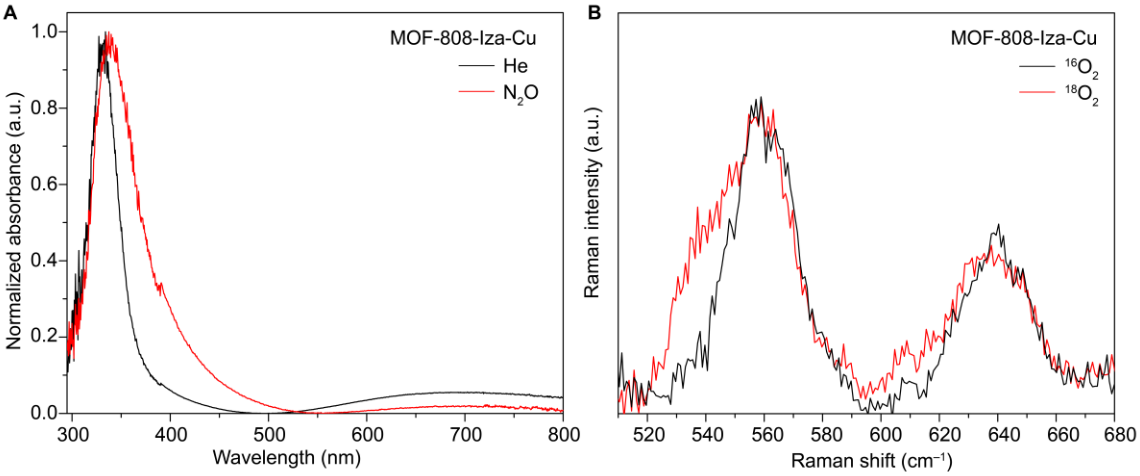

Figure 4.9. UV-Vis DRS spectra after He pretreatment and after reaction with N_2O (A) and (B) Resonance Raman spectra excited at 407 nm of MOF-808-Iza-Cu.

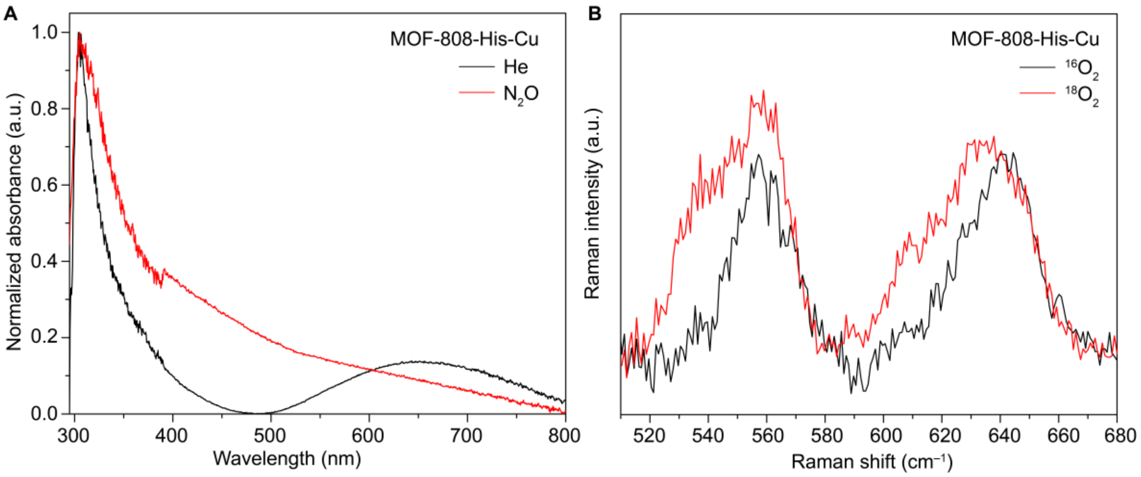

Figure 4.10. UV-Vis DRS spectra after He pretreatment and after reaction with N_2O (A) and (B) Resonance Raman spectra excited at 407 nm of MOF-808-His-Cu.

To definitively characterize this copper–oxygen species, we turned into resonance Raman spectroscopy measurement because each copper–oxygen species have characteristic Raman shifts.[5a,5b] We prepared the samples by synthesizing MOF-808-L-Cu in an argon-filled glovebox and oxygenating the samples with either $^{16}O_2$ or $^{18}O_2$ gas at room temperature. Resonance Raman spectra excited at 407 nm show two $^{18}O_2$-isotope-sensitive Raman peaks at 560 and 640 cm^{-1} which exhibit a 20 cm^{-1} red shift in the $^{18}O_2$ samples for all three MOF-808-L-Cu (Figure 4.8B–4.10B). These two intense vibrational peaks can be ascribed to the core breathing mode of bis(μ-oxo) dicopper species. Ex-situ resonance Raman spectroscopy of the samples after the treatments in He and 3% N_2O/He displays similar Raman peaks indicating that bis(μ-oxo) dicopper species are preserved prior to the methane activation. The deviation (~20 cm^{-1}) in the vibrational energy from the reported values[5b] can be ascribed to the variation in the geometric parameters of the dicopper species due to the framework constraints.

With the information of the location of the ligands and the identity of active copper–oxygen sites, we modeled the active sites using the framework as a constraint and geometrically optimized the models using density functional theory (DFT) calculations. Following the digested ^1H NMR data where ~3 ligand molecules were incorporated per chemical formula, these ligands were placed on the Zr cluster on the pseudohexagonal window in a way such that these ligands pose a minimal steric hindrance to each other. Cu atoms were then allowed to coordinate to N atoms of imidazole units and the Cu atoms were further coordinated to O_2 to form N-Cu_2O_2-N species. From ICP, ^1H NMR, and N K-edge XANES examinations, each N atoms of the ligands is coordinated to one copper atoms. However, copper in bis(μ-oxo) dicopper is known to be four-coordinated.[5b] We propose that the fourth ligand coordinating to copper is a neutral ligand such as water or *N,N*-dimethylformamide molecules as we observed the latter molecule in the ^1H NMR spectra of the digested samples after activation. Geometrical optimization indicates that bis(μ-oxo) dicopper species can reside in the framework in all MOF-808-L-Cu structures. Of particular note, the resonance Raman shifts relevant to O_2 are in close agreement with the experimental data confirming the presence of bis(μ-oxo) dicopper species in the catalysts.

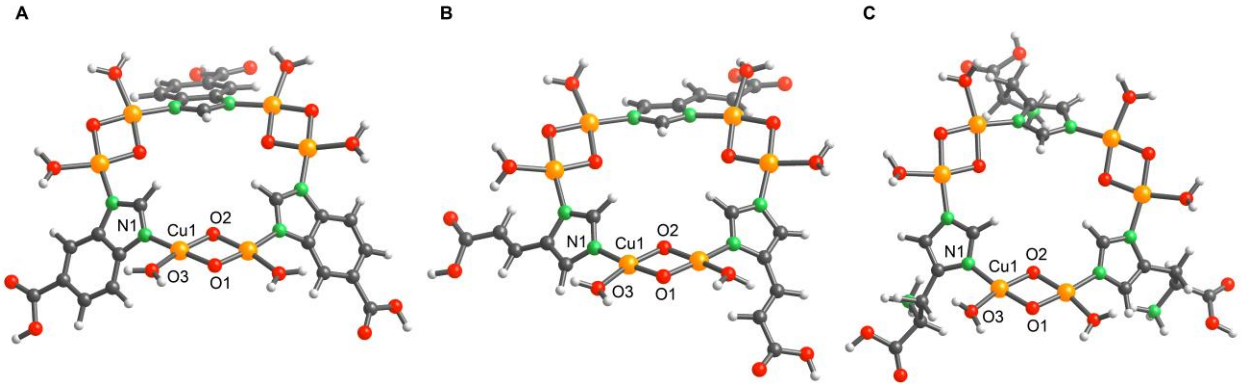

Figure 4.11. DFT optimized structures. (A) MOF-808-Bzz-Cu. Selected geometric parameters (Å): Cu–O1 = 1.784, Cu–O2 = 1.790, Cu–O3 = 1.938, Cu–N = 1.901 and Cu···Cu = 2.812. (B) MOF-808-Iza-Cu. Selected geometric parameters (Å): Cu–O1 = 1.783, Cu–O2 = 1.791, Cu–O3 = 1.940, Cu–N = 1.898 and Cu···Cu = 2.813. (C) MOF-808-His-Cu. Selected geometric parameters (Å): Cu–O1 = 1.781, Cu–O2 = 1.801, Cu–O3 = 1.957, Cu–N = 1.927 and Cu···Cu = 2.855. Atom labeling scheme: C, black; O, red; N, green; H, white; Cu, orange.

Figure 4.12–4.14 depicts the k^2-weighted and Fourier transforms without phase correction of the extended X-ray absorption fine structure (EXAFS) data measured at the Cu K-edge of MOF-808-Bzz-Cu, MOF-808-Iza-Cu and MOF-808-His-Cu. The spectra were recorded after the successive treatment with (a) He, (b) 3% N_2O/He, (c) CH_4 and, (d) 3% steam/He at 150 °C. We used the DFT-optimized cluster as a model to fit the experimental Cu EXAFS spectra. The full EXAFS data were analyzed in k- and R-space using a combined k^1-k^2-k^3 fitting procedure for reliable analysis.[28] The best fits are presented in the figures and the respective fitted parameters are reported in Table 2. In the He treated sample, the first shell is assigned to Cu-N/(O) coordination with the coordination number of 2.9 at distance of 1.94 Å. It should be noted that N and O atoms are indistinguishable from EXAFS analysis as they have similar atomic scattering factors. For the second shell, we identified the scatterer by fitting the EXAFS data with Cu, C, N and O and only Cu could be fitted with reasonable fitting statistics. Copper was found at distance of 2.51 Å with the coordination number of 0.6. This result suggests that copper site is presented as dinuclear and a short distance of Cu···Cu supports the presence of bis(μ-oxo) dicopper species. On the contrary to a formal Cu(III) oxidation state typically assigned for bis(μ-oxo) dicopper species,[29] the oxidation state of active copper in our catalysts appears to be Cu(II). This discrepancy can be ascribed to the high electron density provided by the imidazole ligand to the Cu centers. Oxidation of the catalyst in 3% N_2O/He at 150 °C leads to 0.8 increase of the Cu-N/(O) coordination while its distance remains at 1.94 Å indicating the additional formation of bis(μ-oxo) dicopper species. After methane treatment, there is a slight decrease in Cu-N/(O) coordination and after methanol extraction, Cu-N/(O) coordination increases by 0.6. However, Cu-N/(O) coordination in MOF-808-His-Cu and MOF-808-Iza-Cu remains similar after treatment with methane and steam.

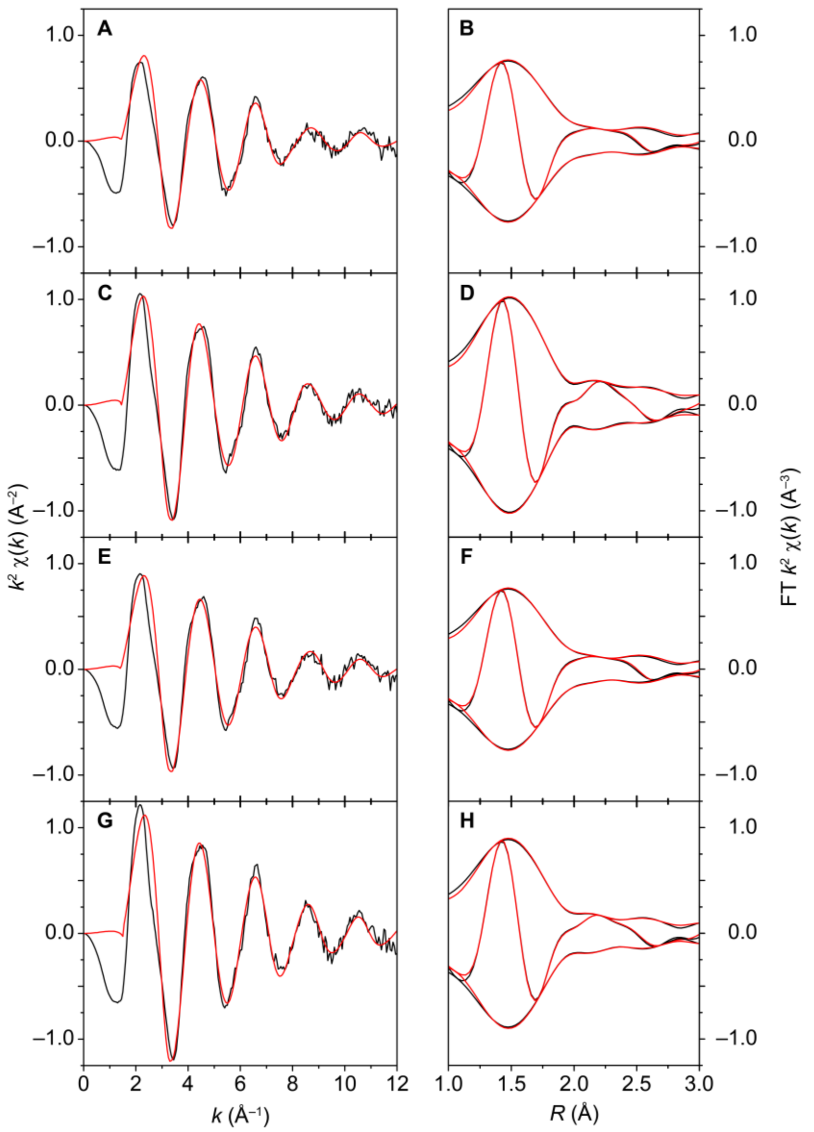

Figure 4.12. The series of k^2-weighted Cu-EXAFS spectra of MOF-808-Bzz-Cu (black line) and best fit (red line) in k-space (left) and R-space (right) without phase correction after the reactions with **A, B** He; **C, D** 3% N_2O/He; **E, F** CH_4 and **G, H** 3% steam/He at 150 °C.

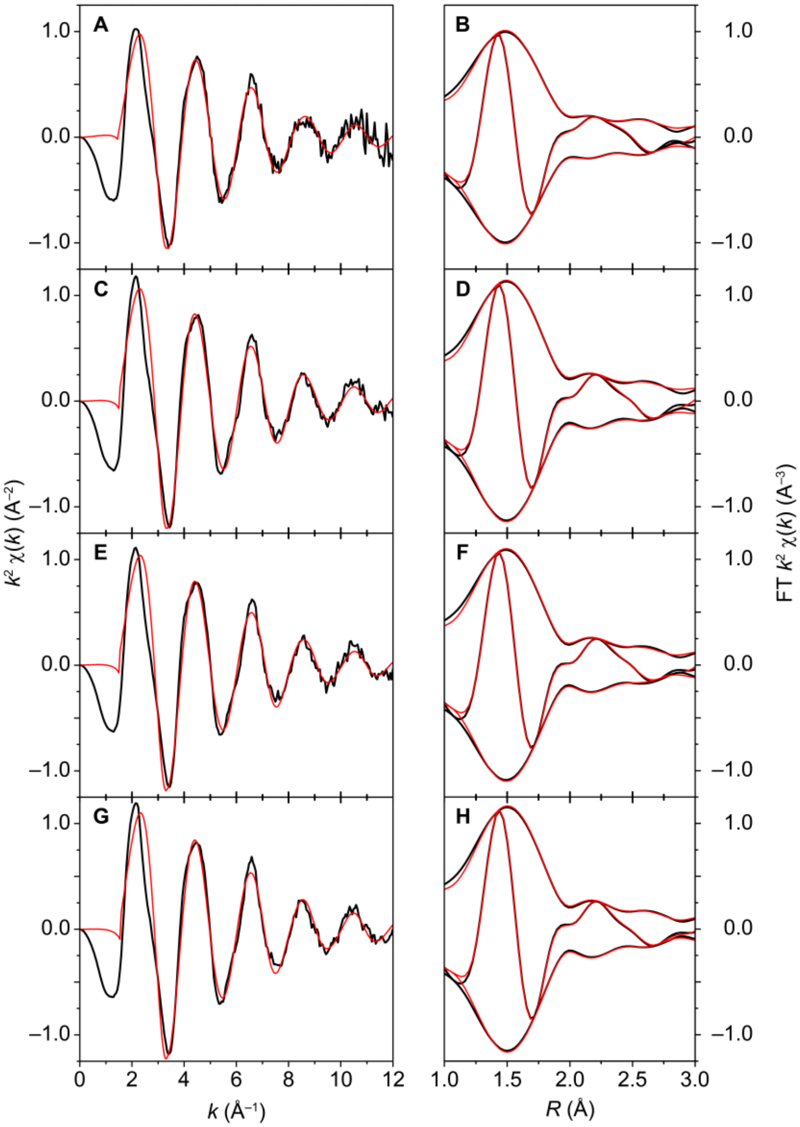

Figure 4.13. The series of k^2-weighted Cu-EXAFS spectra of MOF-808-Iza-Cu (black line) and best fit (red line) in *k*-space (left) and *R*-space (right) without phase correction after the reactions with **A, B** He; **C, D** 3% N_2O/He; **E, F** CH_4 and **G, H** 3% steam/He at 150 °C.

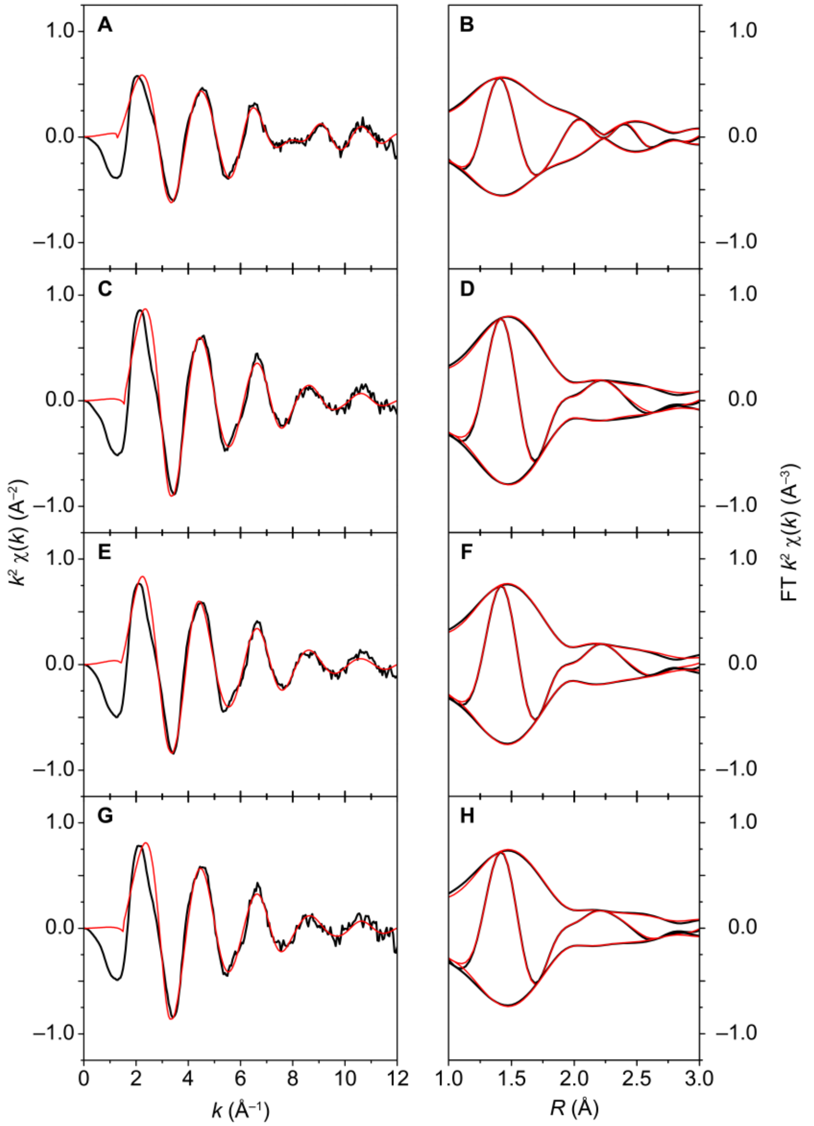

Figure 4.14. The series of k^2-weighted Cu-EXAFS spectra of MOF-808-His-Cu (black line) and best fit (red line) in *k*-space (left) and *R*-space (right) without phase correction after the reactions with **A, B** He; **C, D** 3% N_2O/He; **E, F** CH_4 and **G, H** 3% steam/He at 150 °C.

Table 4.2. Cu EXAFS fitting result of MOF-808-Bzz-Cu, MOF-808-Iza-Cu and MOF-808-His-Cu with a series of treatments.

Ab-Sc pair[a]	N[b]	R[c]	DWF[d]	R-factor
MOF-808-Bzz-Cu, He treated at 150 °C				
Cu-N/(O) SS[g]	2.9	1.94±0.02	0.0080±0.0025	0.019
Cu···Cu SS	0.6	2.51±0.04	0.0146±0.0065	
MOF-808-Bzz-Cu, N_2O treated at 150 °C				
Cu-N/(O) SS	3.7	1.94±0.02	0.0070±0.0025	0.021
Cu···Cu SS	0.4	2.49±0.10	0.0156±0.0149	
MOF-808-Bzz-Cu, CH_4 treated at 150 °C				
Cu-N/(O) SS	3.3	1.94±0.02	0.0072±0.0025	0.020
Cu···Cu SS	0.5	2.51±0.07	0.0151±0.0102	
MOF-808-Bzz-Cu, Steam treated at 150 °C				
Cu-N/(O) SS	3.9	1.95±0.01	0.0058±0.0022	0.018
Cu···Cu SS	0.5	2.53±0.10	0.0169±0.0151	
MOF-808-Iza-Cu, He treated at 150 °C				
Cu-N/(O) SS[g]	3.5	1.94±0.02	0.0070±0.0023	0.017
Cu···Cu SS	2	2.52±0.07	0.0302±0.0104	
MOF-808-Iza-Cu, N_2O treated at 150 °C				
Cu-N/(O) SS	3.9	1.95±0.02	0.0060±0.0023	0.022
Cu···Cu SS	0.6	2.51±0.11	0.0188±0.0158	
MOF-808-Iza-Cu, CH_4 treated at 150 °C				
Cu-N/(O) SS	3.8	1.95±0.01	0.0062±0.0024	0.021
Cu···Cu SS	0.4	2.49±0.13	0.0173±0.0190	
MOF-808-Iza-Cu, Steam treated at 150 °C				
Cu-N/(O) SS	3.8	1.96±0.01	0.0056±0.0022	0.021
Cu···Cu SS	0.5	2.52±0.12	0.0184±0.0178	
MOF-808-His-Cu, He treated at 150 °C				
Cu-N/(O) SS[g]	2.5	1.92±0.01	0.0090±0.0022	0.013
Cu···Cu SS	0.5	2.50±0.02	0.0063±0.0022	
MOF-808-His-Cu, N_2O treated at 150 °C				
Cu-N/(O) SS	3.1	1.94±0.01	0.0082±0.0023	0.017
Cu···Cu SS	0.3	2.46±0.10	0.0159±0.0131	
MOF-808-His-Cu, CH_4 treated at 150 °C				
Cu-N/(O) SS	3	1.94±0.01	0.0081±0.0024	0.019
Cu···Cu SS	0.2	2.43±0.16	0.0168±0.0219	
MOF-808-His-Cu, Steam treated at 150 °C				
Cu-N/(O) SS	3.1	1.94±0.02	0.0087±0.0026	0.020
Cu···Cu SS	0.2	2.48±0.09	0.0082±0.0115	

[a]Ab = absorber; Sc = scatterer. [b] Coordination number. [c] Distance (Å). [d] Debye-Waller factor (Å^2). [e] Bond Valence Sums; Calculated using r_0 value Cu(II)-N = 1.719 Å. [f] Calculated using r_0 value Cu(III)-N = 1.753 Å. [g] Fitting was conducted using N scatter. Fit: $3 < k < 10$ Å^{-1}; $1 < R < 4$ Å.

4.4 Conclusions

In this chapter, the design and synthesis of metal-organic framework (MOF) catalysts inspired by pMMO for selective methane oxidation to methanol has been described. The catalysts show high selectivity for methane oxidation to methanol under isothermal conditions at 150 °C. Combined spectroscopies and density functional theory calculations reveal bis(μ-oxo) dicopper species as the active site of the catalysts.

4.5 Appendices

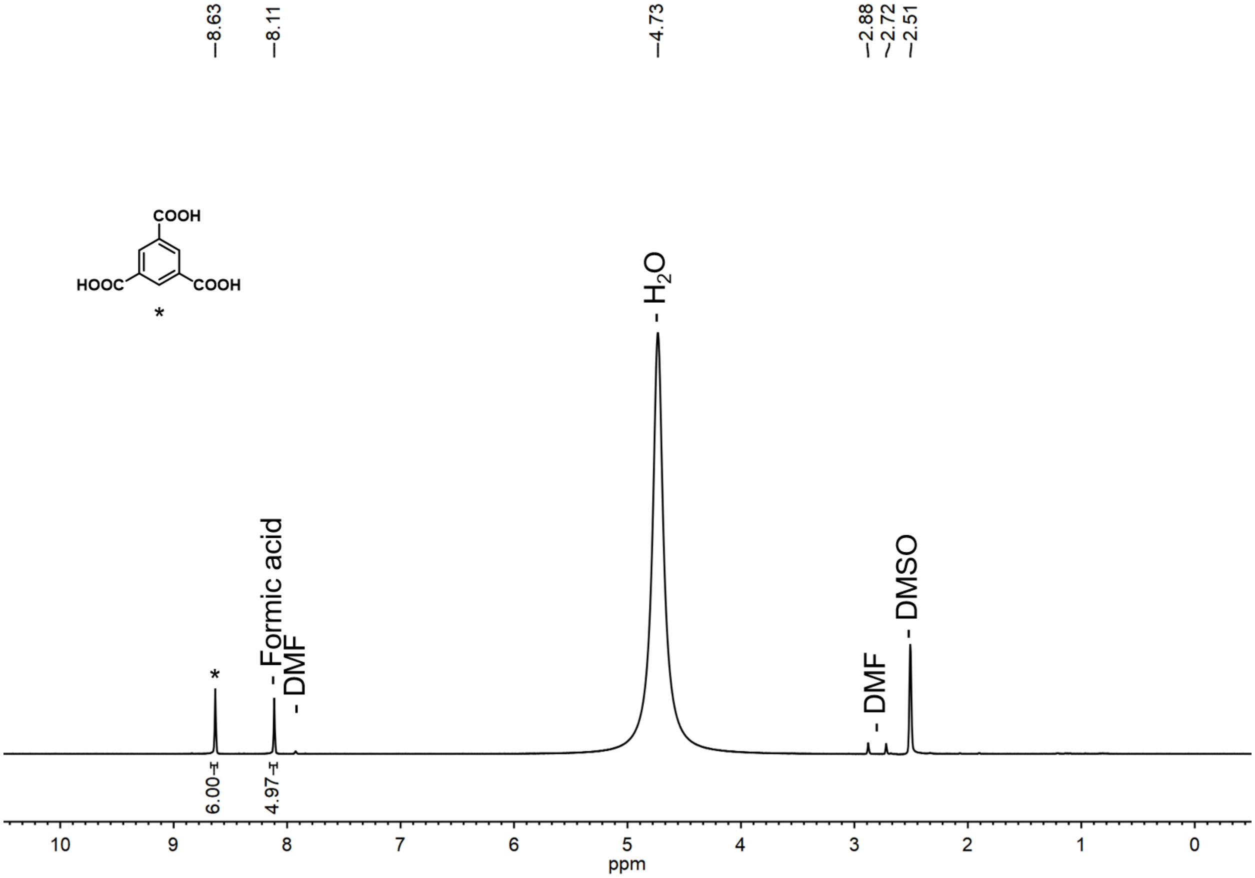

Figure A4.1. ^{1}H NMR spectrum of digested MOF-808.

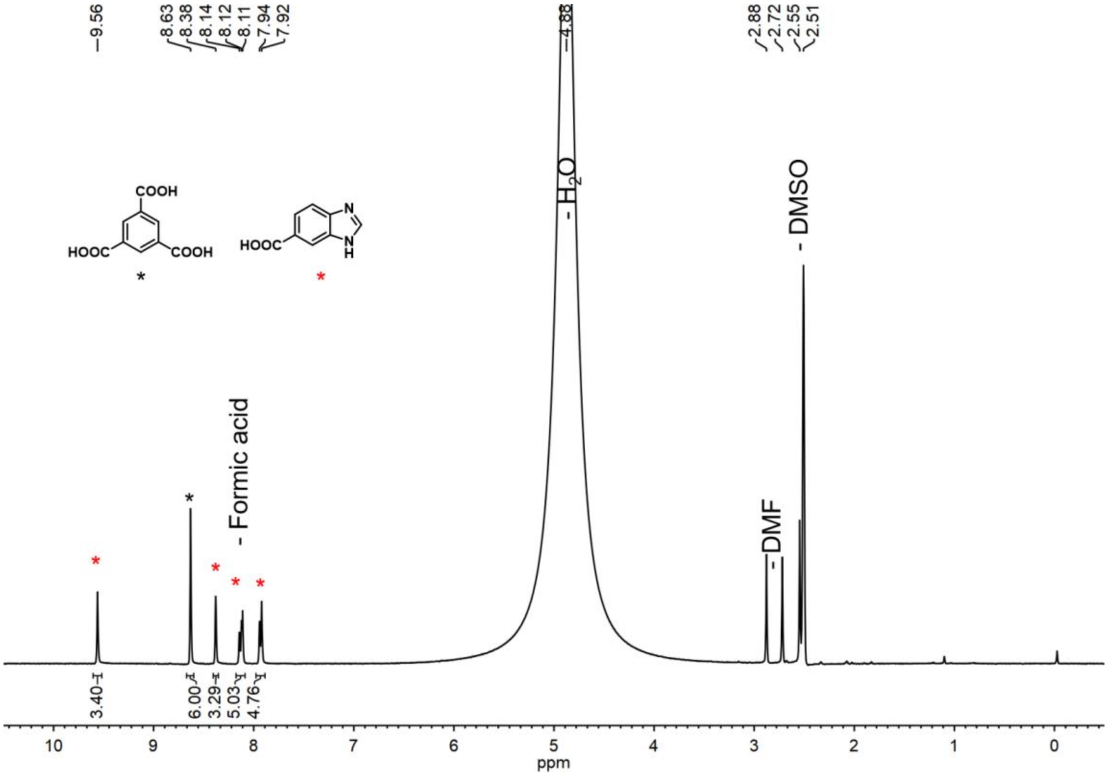

Figure A4.2. ^{1}H NMR spectrum of digested MOF-808-Bzz.

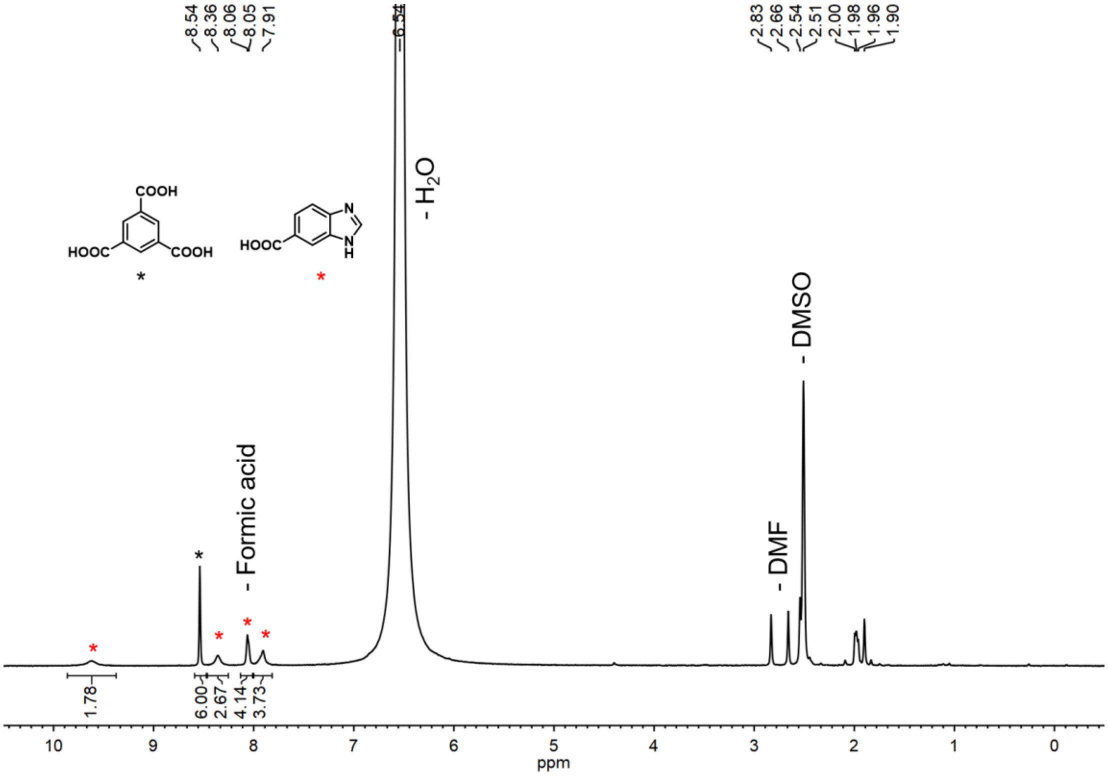

Figure A4.3. ^{1}H NMR spectrum of digested MOF-808-Bzz-Cu.

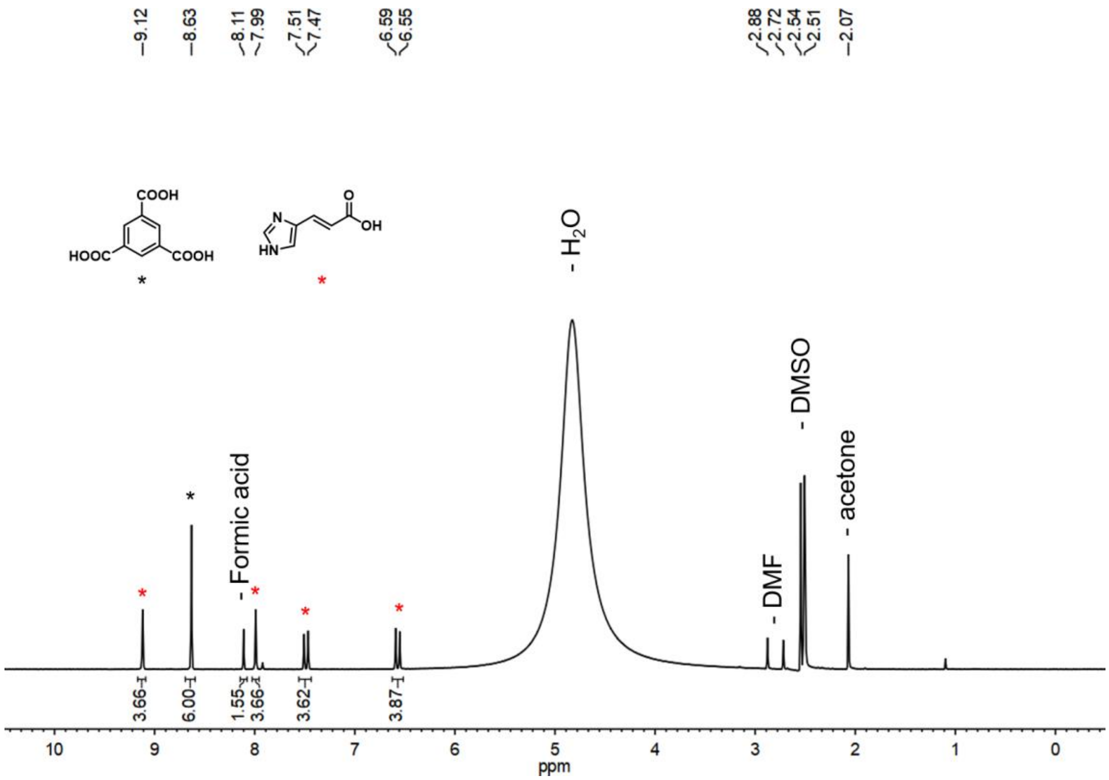

Figure A4.4. ^{1}H NMR spectrum of digested MOF-808-Iza.

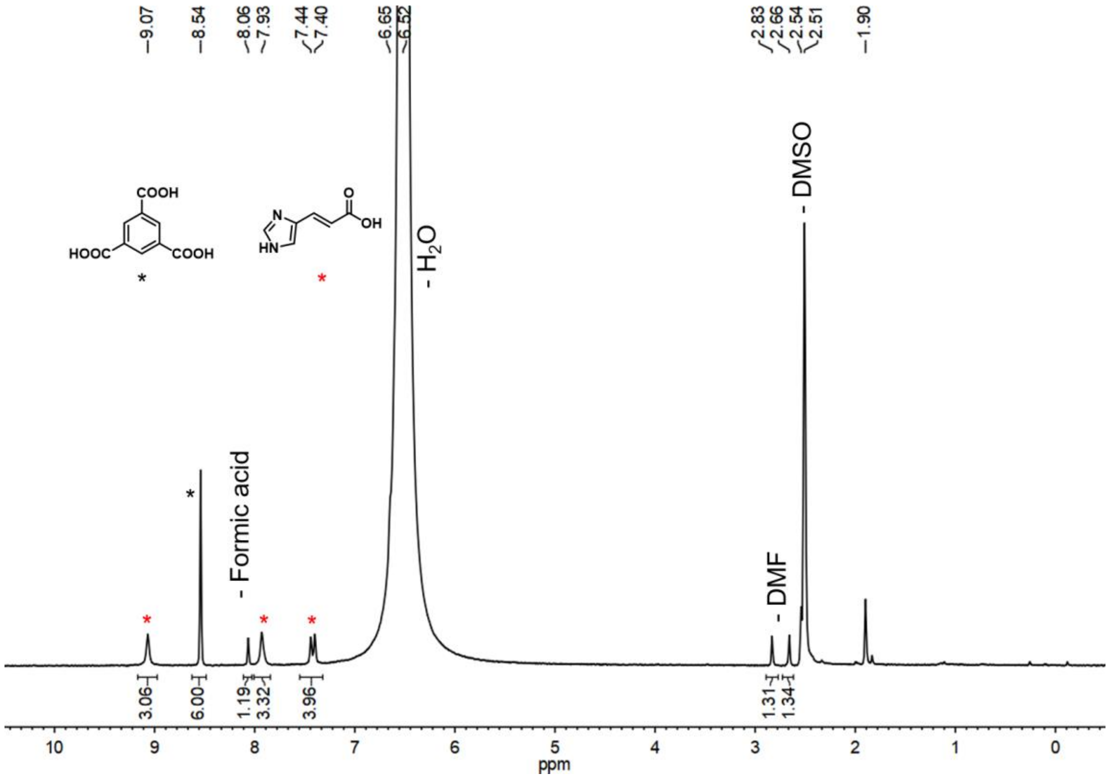

Figure A4.5. ^{1}H NMR spectrum of digested MOF-808-Iza-Cu.

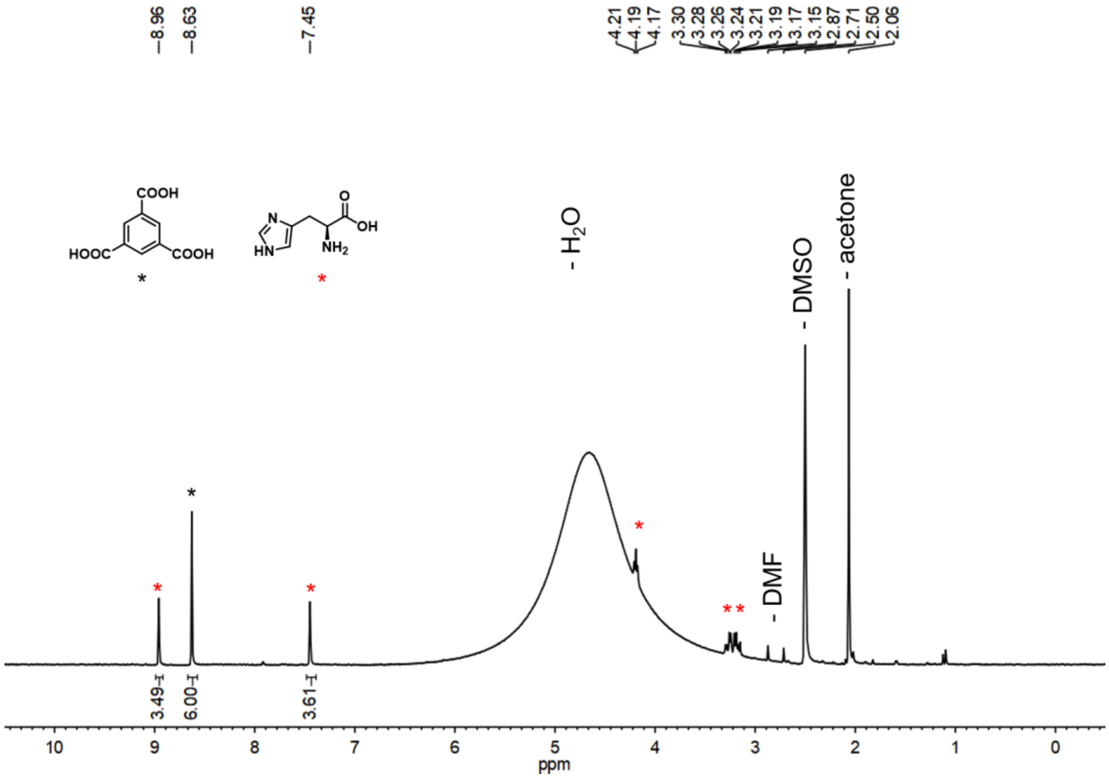

Figure A4.6. ^{1}H NMR spectrum of digested MOF-808-His.

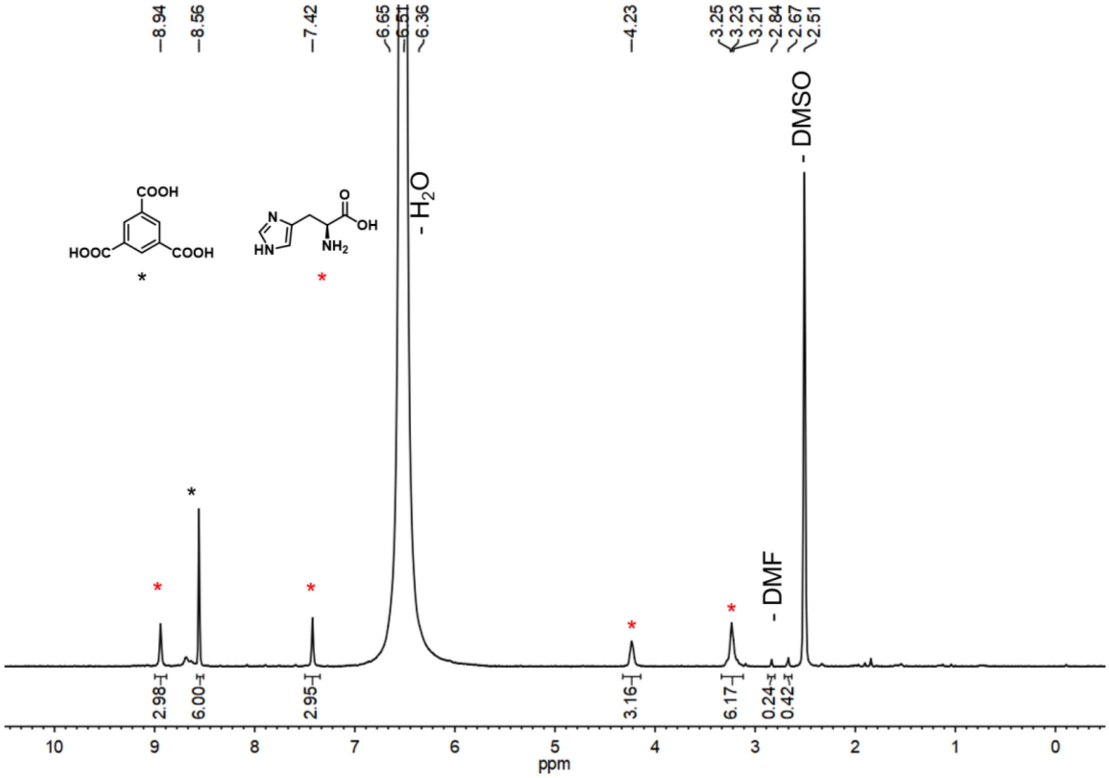

Figure A4.7. ^{1}H NMR spectrum of digested MOF-808-His-Cu.

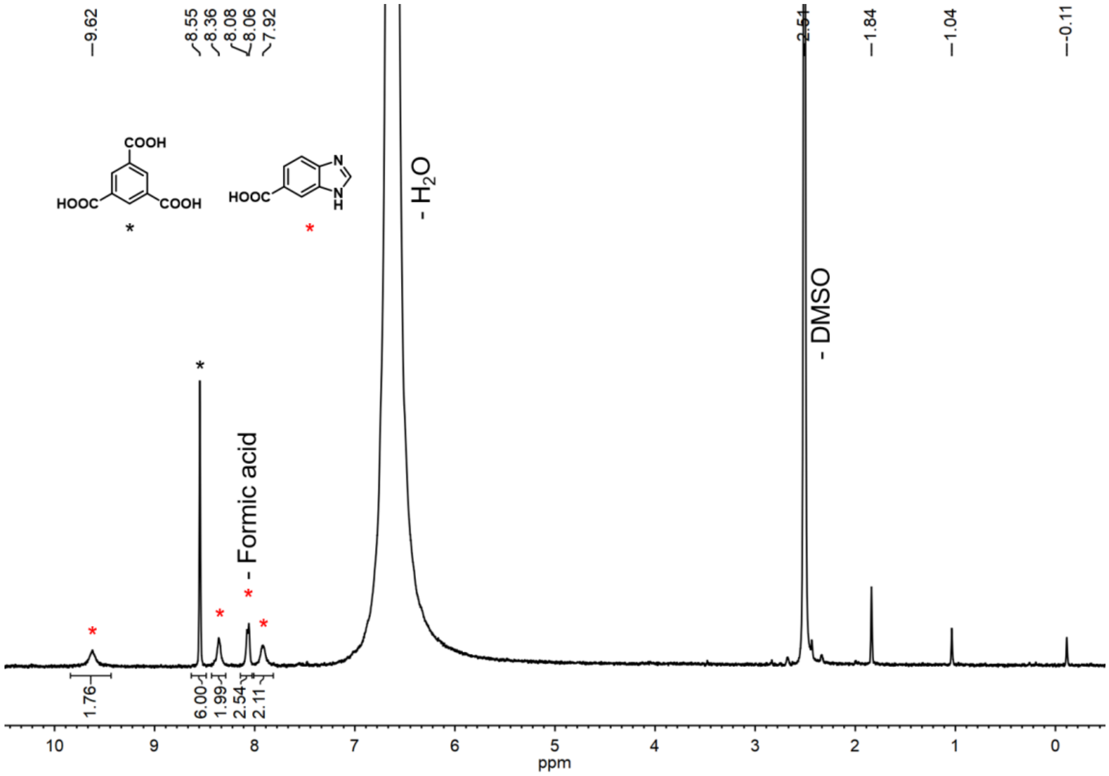

Figure A4.8. ^{1}H NMR spectrum of digested MOF-808-Bzz-Cu after reaction.

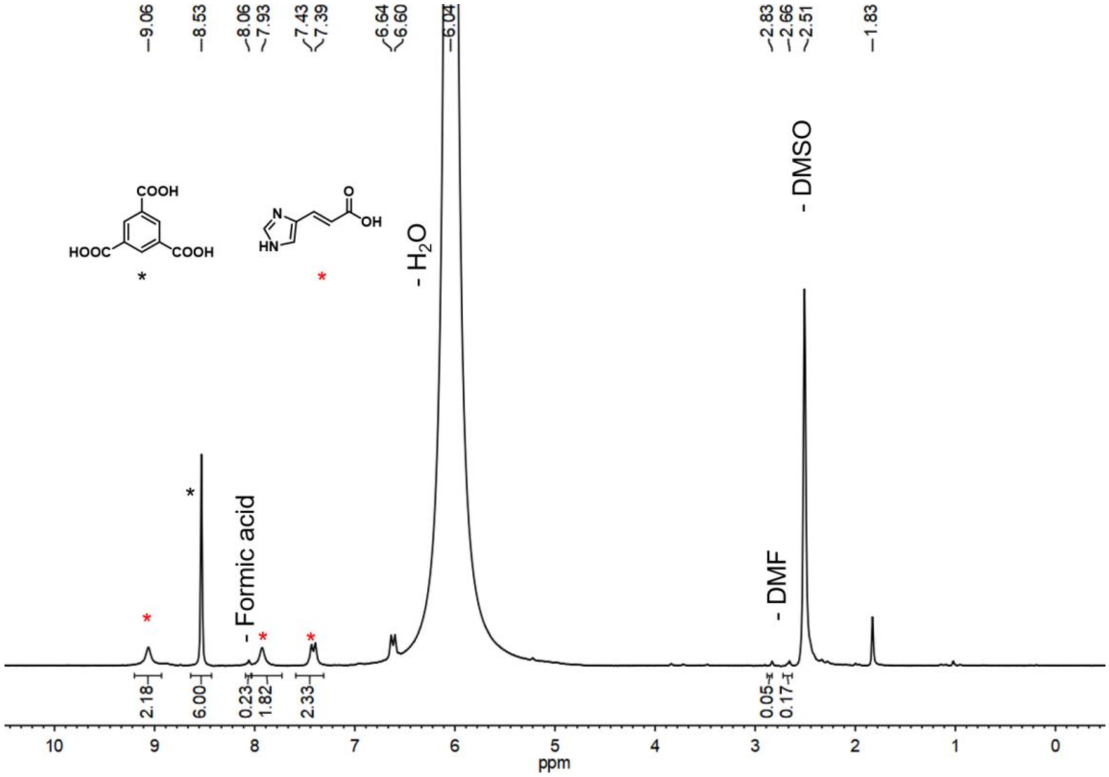

Figure A4.9. ^{1}H NMR spectrum of digested MOF-808-Iza-Cu after reaction.

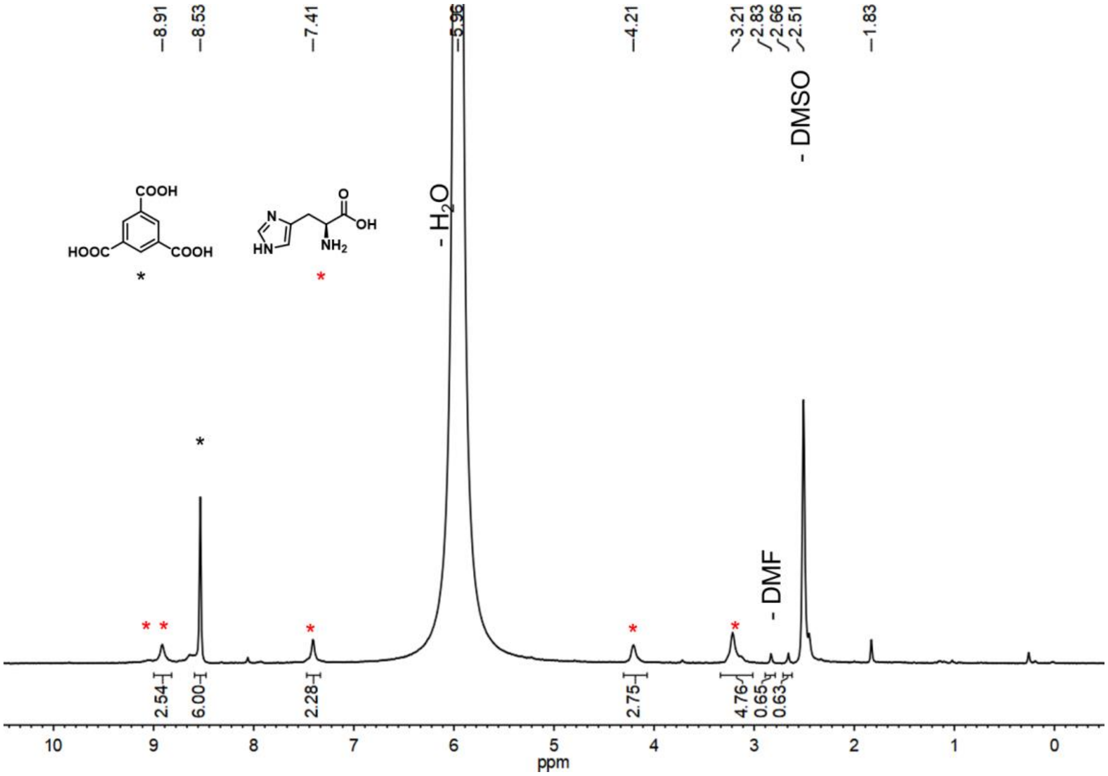

Figure A4.10. ^{1}H NMR spectrum of digested MOF-808-His-Cu after reaction.

(a)

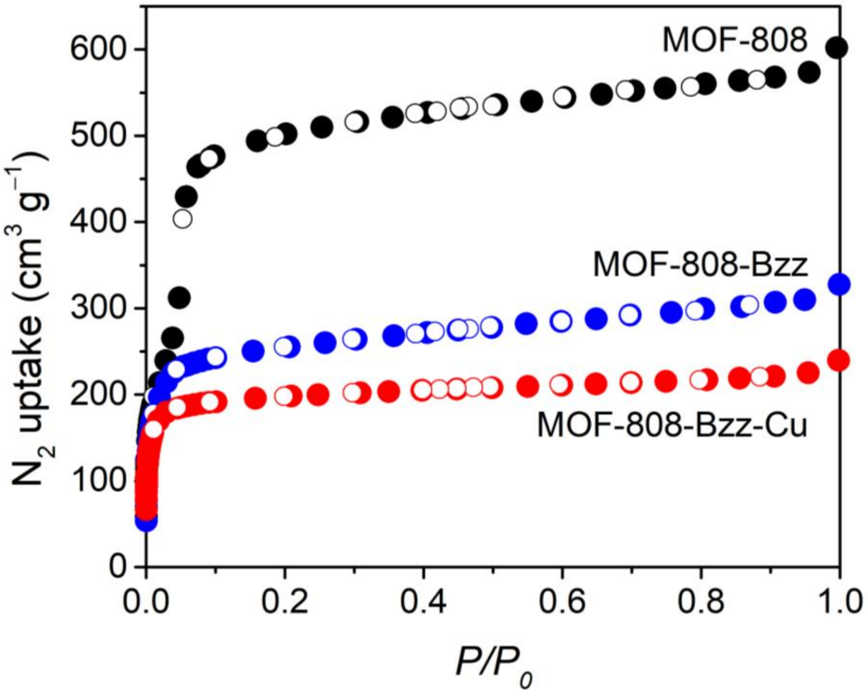

(b)

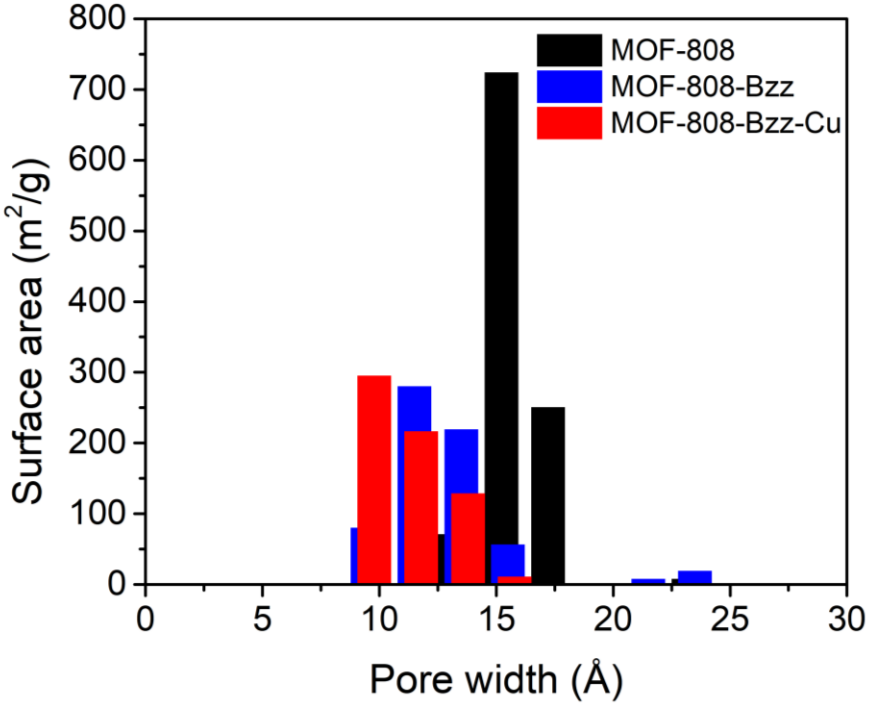

Figure A4.11. Nitrogen adsorption isotherms of MOF-808, MOF-808-Bzz and MOF-808-Bzz-Cu (a) and their calculated pore size distribution histograms (b).

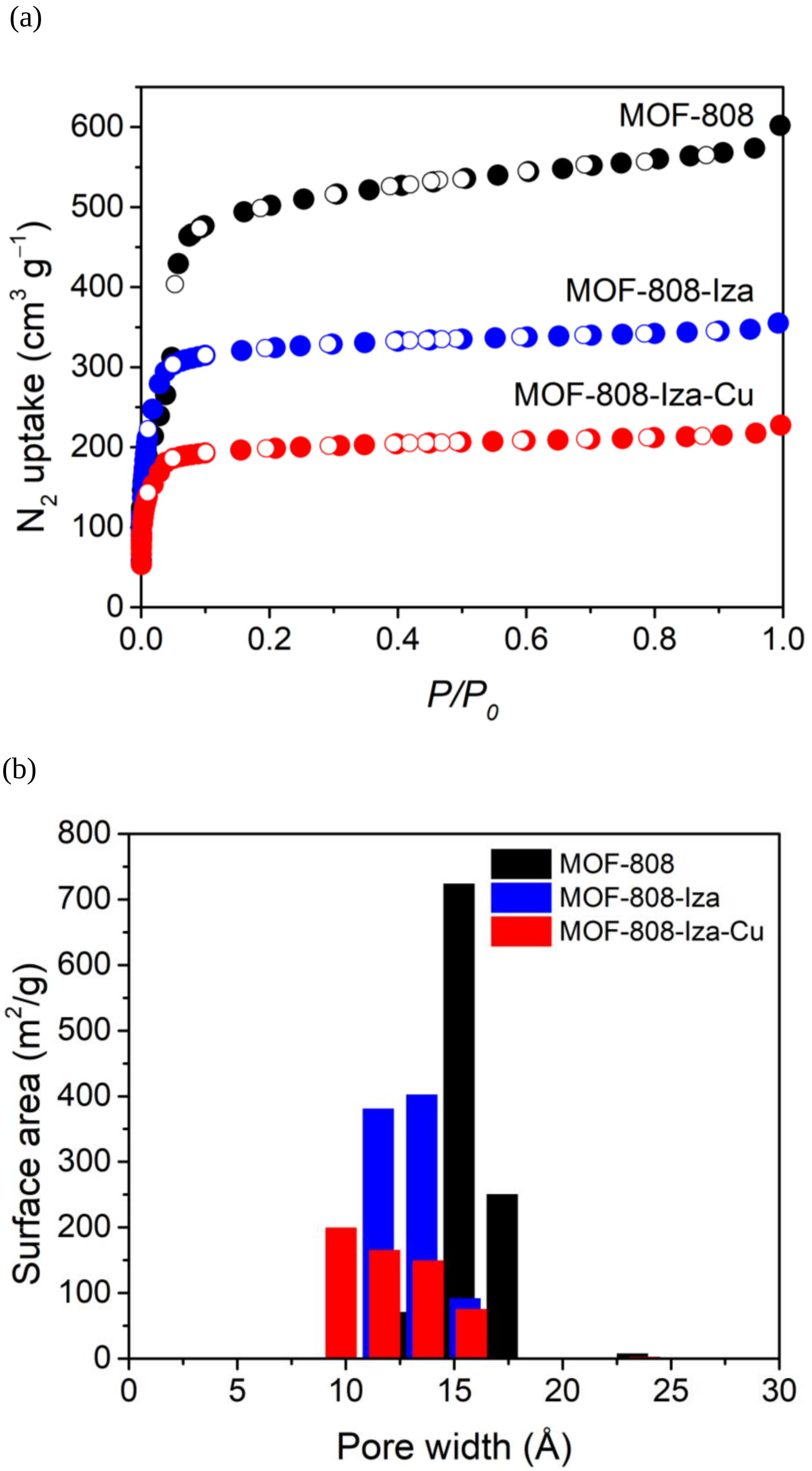

Figure A4.12. Nitrogen adsorption isotherms of MOF-808, MOF-808-Iza and MOF-808-Iza-Cu (a) and their calculated pore size distribution histograms (b).

(a)

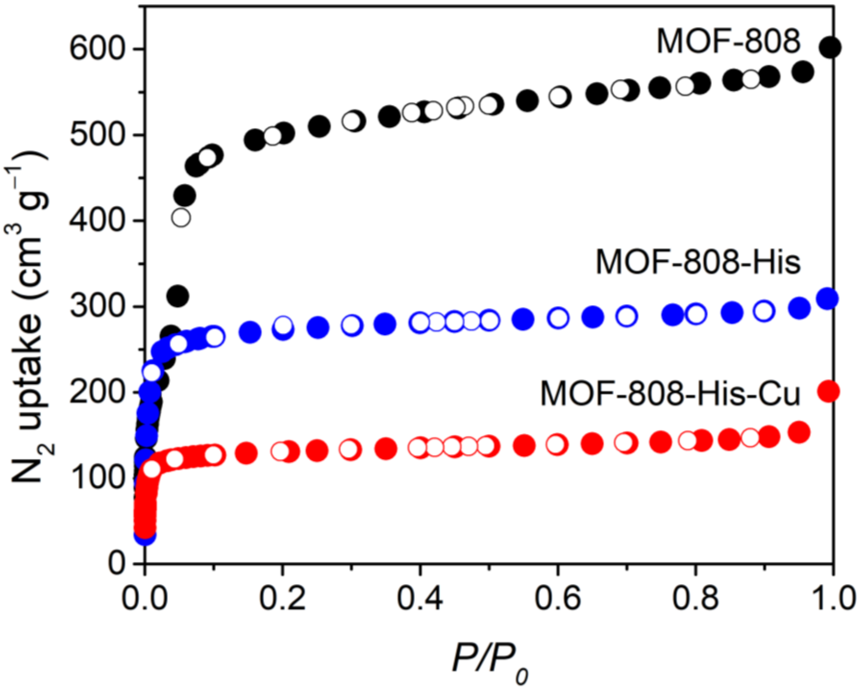

(b)

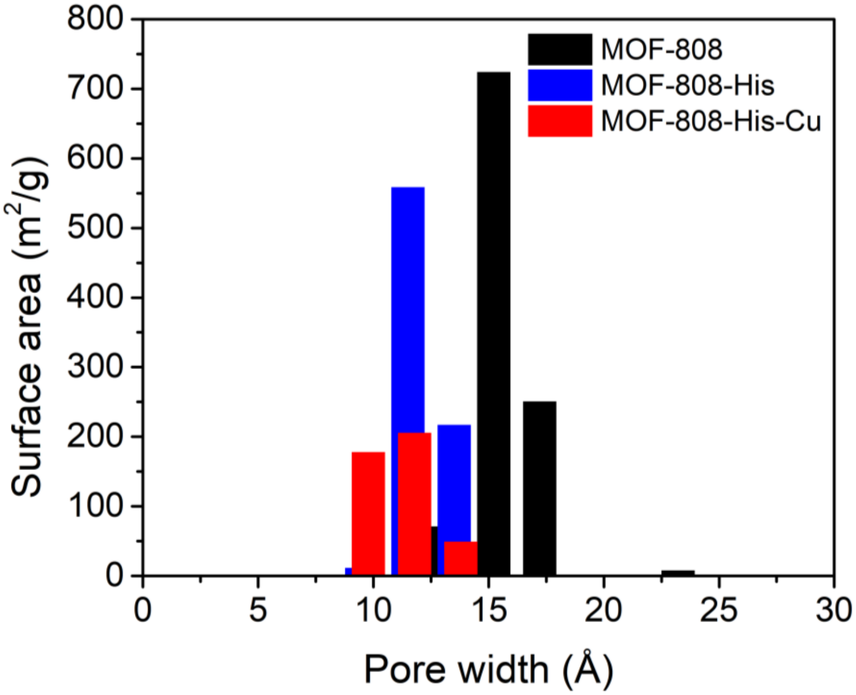

Figure A4.13. Nitrogen adsorption isotherms of MOF-808, MOF-808-His and MOF-808-His-Cu (a) and their calculated pore size distribution histograms (b).

Table A4.1. Summary of surfaces of the materials presented in the graphs shown above.

Material	Calculated BET surface area (m^2 g^{-1})
MOF-808	1490
MOF-808-His	800
MOF-808-His-Cu	390
MOF-808-Iza	950
MOF-808-Iza-Cu	580
MOF-808-Bzz	765
MOF-808-Bzz-Cu	580

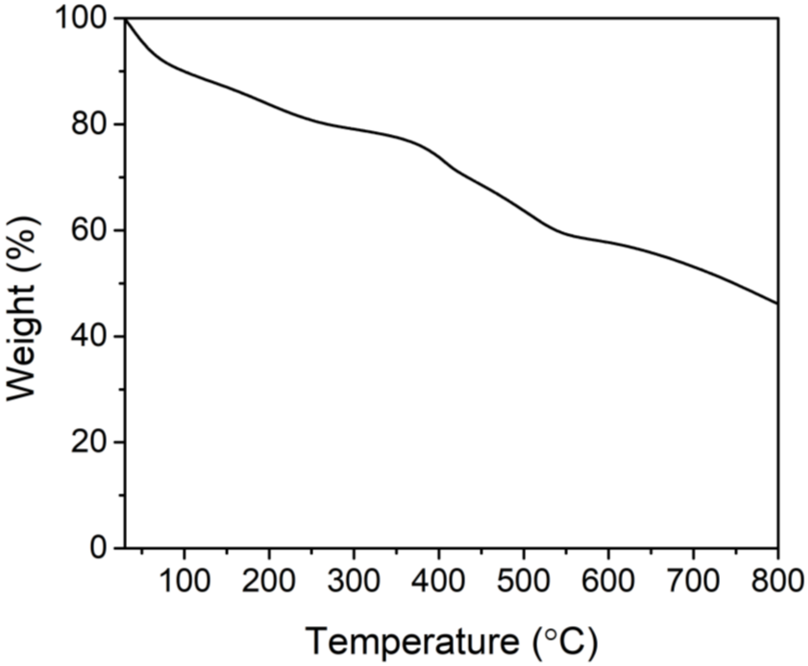

Figure A4.14. TGA trace of MOF-808-Bzz-Cu.

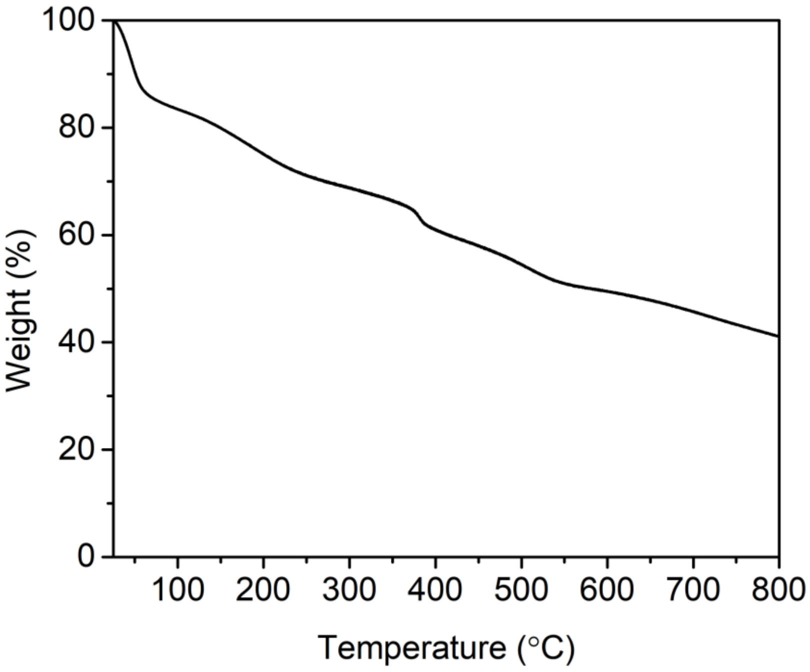

Figure A4.15. TGA trace of MOF-808-Iza-Cu.

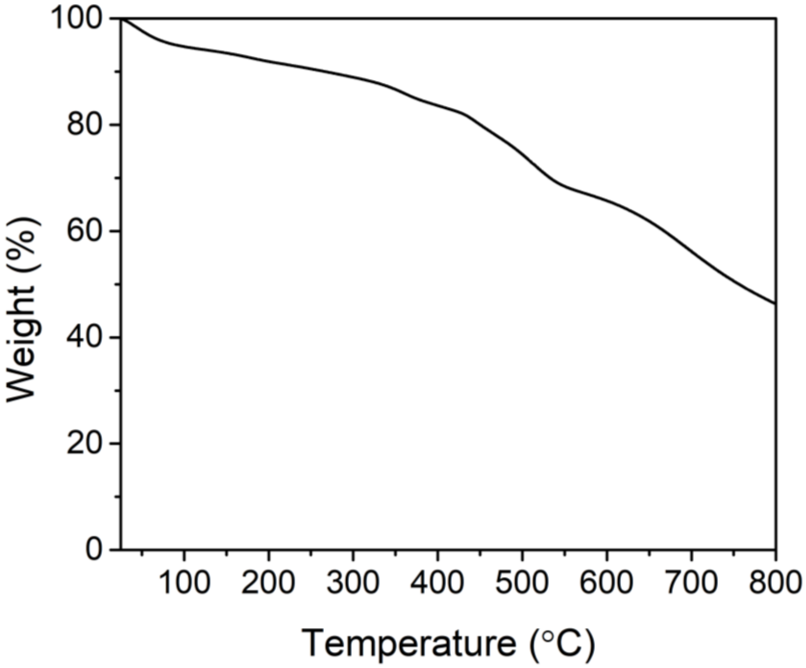

Figure A4.16. TGA trace of MOF-808-His-Cu.

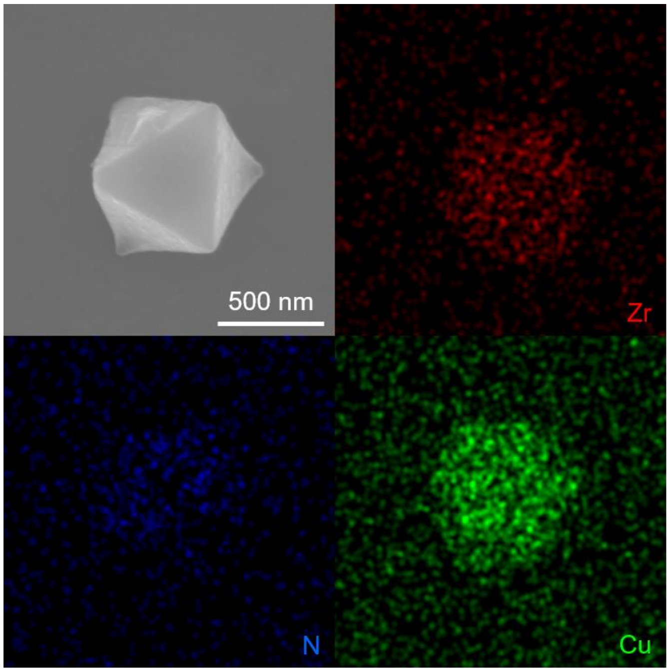

Figure A4.17. Elemental mapping using energy-dispersive X-ray spectroscopy of MOF-808-Bzz-Cu shows a uniform distribution of nitrogen and copper.

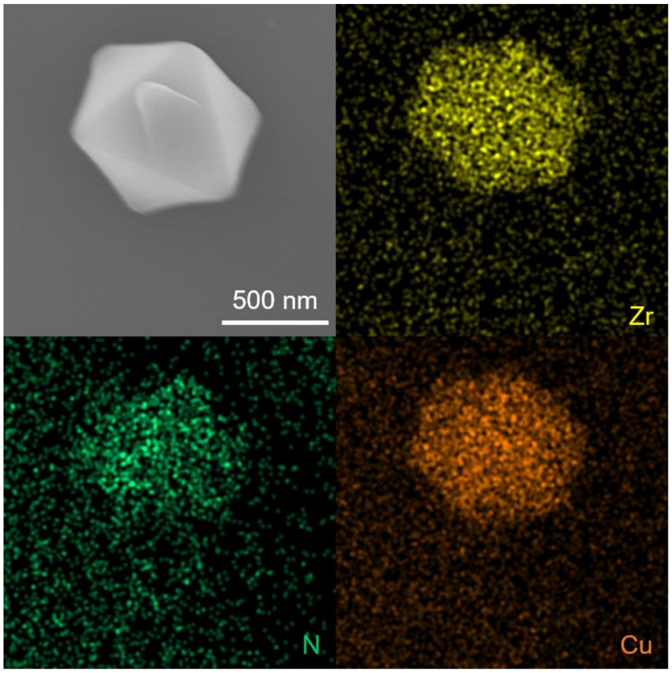

Figure A4.18. Elemental mapping using energy-dispersive X-ray spectroscopy of MOF-808-Iza-Cu shows a uniform distribution of nitrogen and copper.

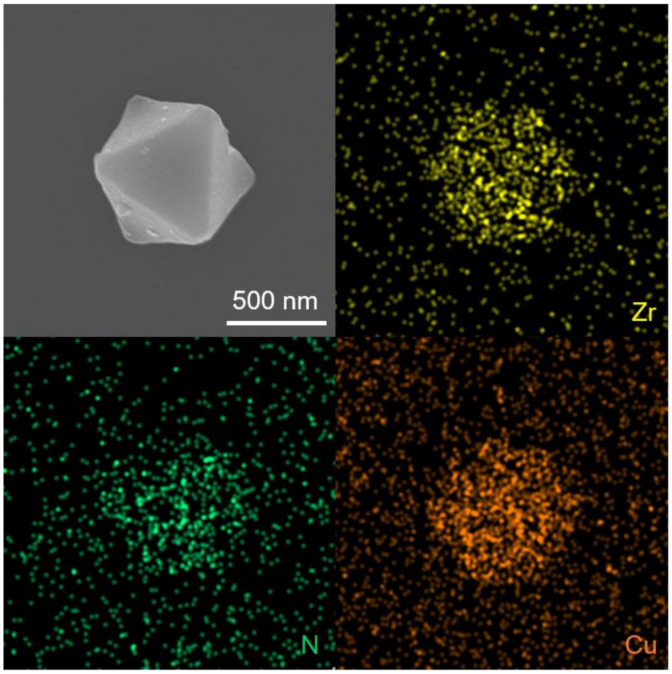

Figure A4.19. Elemental mapping using energy-dispersive X-ray spectroscopy of MOF-808-His-Cu shows a uniform distribution of nitrogen and copper.

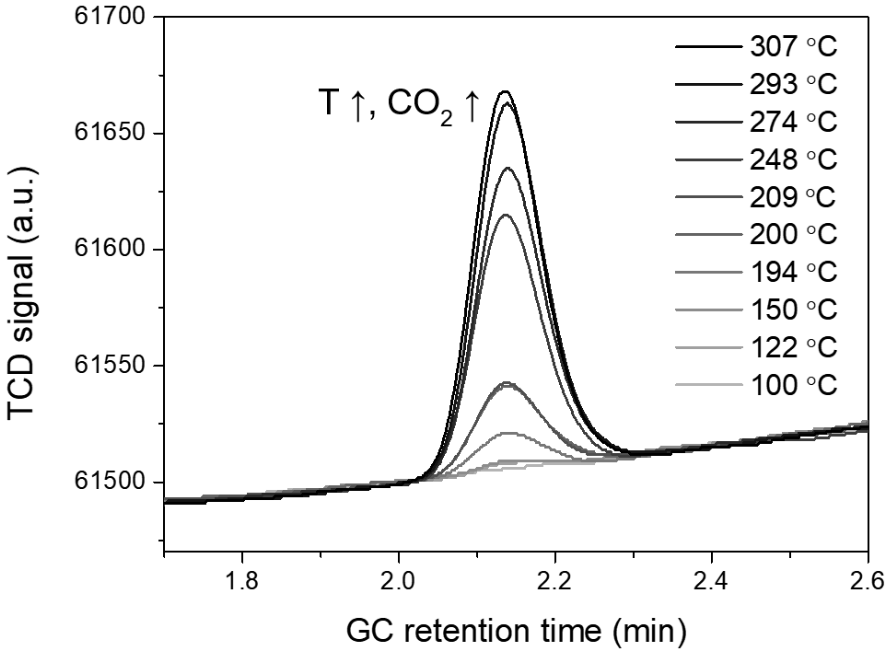

Figure A4.20. Gas chromatograph of thermal conductivity detector in the region of CO_2 as a function of methanol extraction temperature using 3% steam/He.

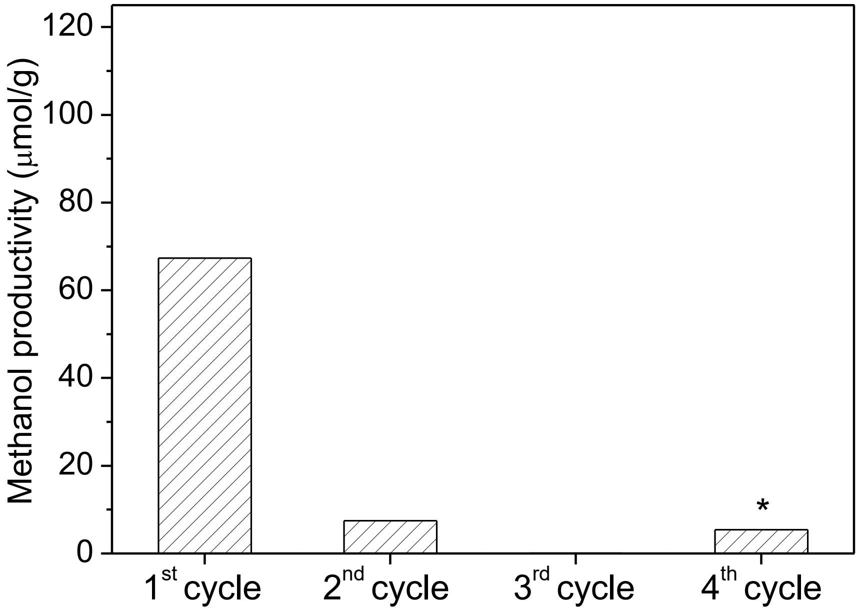

Figure A4.21. Recyclability test of MOF-808-Bzz-Cu. Each cycle was performed with a series of treatments: He for 1 h; 3% N_2O/He for 2 h; CH_4 for 1 h and 3% steam/He at 150 °C. *4th cycle was carried out after He treatment at 250 °C for 10 min with a ramping rate of 3 °C min^{-1} after the 3rd cycle.

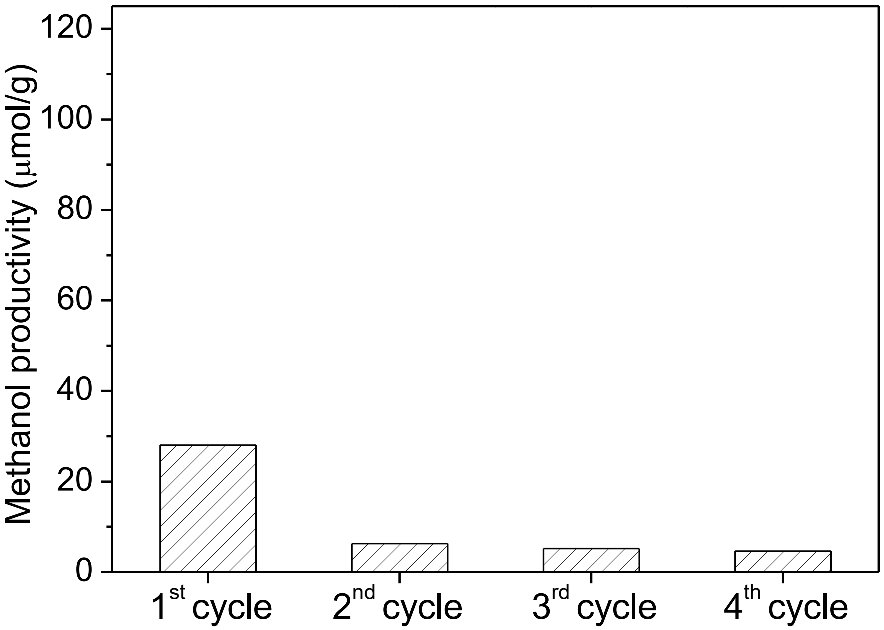

Figure A4.22. Recyclability test of MOF-808-His-Cu. Each cycle was performed with a series of treatments: He for 1 h; 3% N_2O/He for 2 h; CH_4 for 1 h and 3% steam/He at 150 °C.

Table A4.2. Crystal data and structure refinement for MOF-808-His.

Empirical formula	$C_{2.12}H_{0.5}O_{2.67}Zr_{0.5}$
Formula weight	114.18
Temperature/K	100
Crystal system	cubic
Space group	*Fd-3m*
a/Å	35.0494(9)
b/Å	35.0494(9)
c/Å	35.0494(9)
α/°	90
β/°	90
γ/°	90
Volume/Å^3	43057(3)
Z	192
ρ_{calc}g/cm^3	0.845
μ/mm^{-1}	1.094
F(000)	10469.0
Crystal size/mm^3	0.03 × 0.03 × 0.03
Radiation	Synchrotron (λ = 0.8856 Å)
2Θ range for data collection/°	2.508 to 67.542
Index ranges	$-43 \leq h \leq 43$, $-43 \leq k \leq 43$, $-43 \leq l \leq 43$
Reflections collected	141131
Independent reflections	2140 [R_{int} = 0.2489, R_{sigma} = 0.0567]
Data/restraints/parameters	2140/0/77
Goodness-of-fit on F^2	1.209
Final R indexes [I>=2σ (I)]	R_1 = 0.0745, wR_2 = 0.2204
Final R indexes [all data]	R_1 = 0.1166, wR_2 = 0.2485
Largest diff. peak/hole / e Å^{-3}	1.31/-1.32

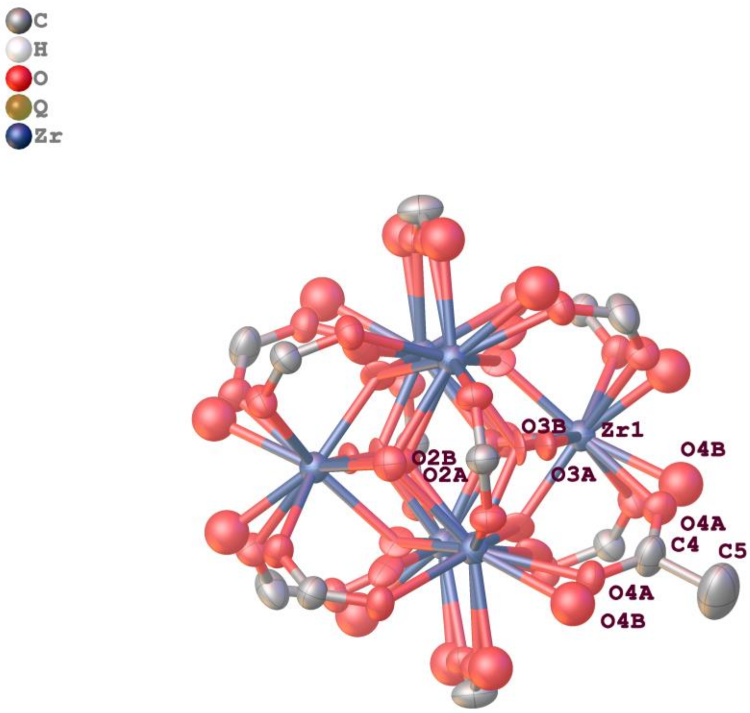

Figure A4.23. Partial structure of MOF-808-His resolved from the single-crystal structure. Thermal ellipsoids are plotted with 50% probability.

Table A4.3. Crystal data and structure refinement for MOF-808-Iza.

Empirical formula	$C_{1.74}H_{0.5}O_{2.83}Zr_{0.5}$
Formula weight	112.36
Temperature/K	100
Crystal system	cubic
Space group	*Fd-3m*
a/Å	35.0104(14)
b/Å	35.0104(14)
c/Å	35.0104(14)
α/°	90
β/°	90
γ/°	90
Volume/Å^3	42913(5)
Z	192
ρ_{calc}g/cm^3	0.835
μ/mm^{-1}	1.398
F(000)	10294.0
Crystal size/mm^3	0.03 × 0.03 × 0.03
Radiation	Synchrotron (λ = 0.9537 Å)
2Θ range for data collection/°	2.704 to 73.35
Index ranges	$-42 \leq h \leq 43$, $-43 \leq k \leq 43$, $-43 \leq l \leq 42$
Reflections collected	90231
Independent reflections	2111 [R_{int} = 0.1485, R_{sigma} = 0.0346]
Data/restraints/parameters	2111/15/82
Goodness-of-fit on F^2	1.191
Final R indexes [I>=2σ (I)]	R_1 = 0.0566, wR_2 = 0.1880
Final R indexes [all data]	R_1 = 0.0716, wR_2 = 0.2031
Largest diff. peak/hole / e Å^{-3}	1.08/-0.97

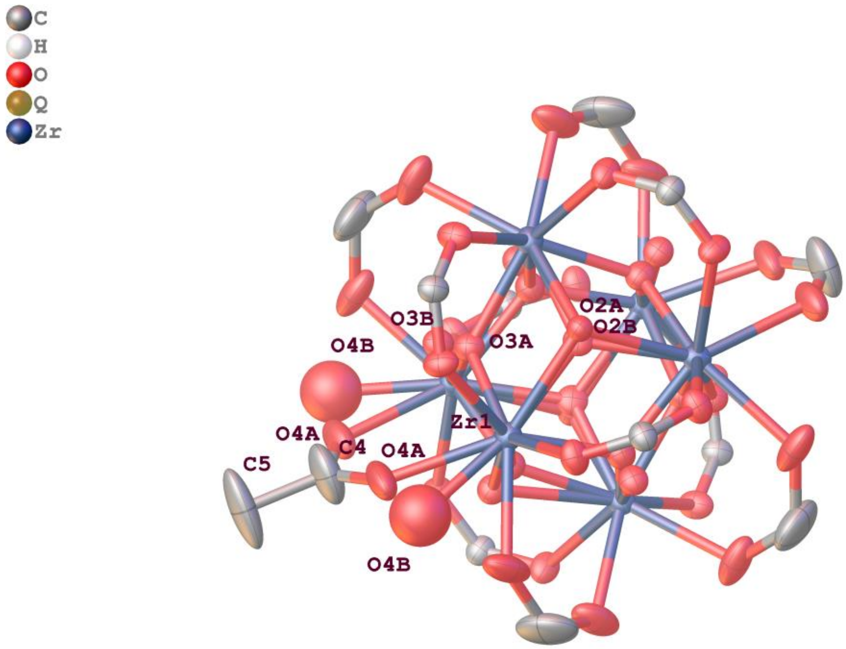

Figure A4.24. Partial structure of MOF-808-Iza resolved from the single-crystal structure. Thermal ellipsoids are plotted with 50% probability.

Table A4.4. Crystal data and structure refinement for MOF-808-Bzz.

Empirical formula	$C_{1.9}H_{0.55}O_{2.77}Zr_{0.5}$
Formula weight	113.34
Temperature/K	100
Crystal system	cubic
Space group	*Fd-3m*
a/Å	35.0221(15)
b/Å	35.0221(15)
c/Å	35.0221(15)
α/°	90
β/°	90
γ/°	90
Volume/Å^3	42956(6)
Z	192
ρ_{calc}g/cm^3	0.841
μ/mm^{-1}	1.318
F(000)	10393.0
Crystal size/mm^3	0.03 × 0.03 × 0.03
Radiation	Synchrotron (λ = 0.9538 Å)
2Θ range for data collection/°	2.702 to 68.494
Index ranges	$-41 \leq h \leq 41$, $-41 \leq k \leq 41$, $-41 \leq l \leq 41$
Reflections collected	110349
Independent reflections	1797 [R_{int} = 0.1312, R_{sigma} = 0.0341]
Data/restraints/parameters	1797/63/79
Goodness-of-fit on F^2	1.181
Final R indexes [I>=2σ (I)]	R_1 = 0.0713, wR_2 = 0.2200
Final R indexes [all data]	R_1 = 0.0873, wR_2 = 0.2392
Largest diff. peak/hole / e Å^{-3}	2.08/-1.10

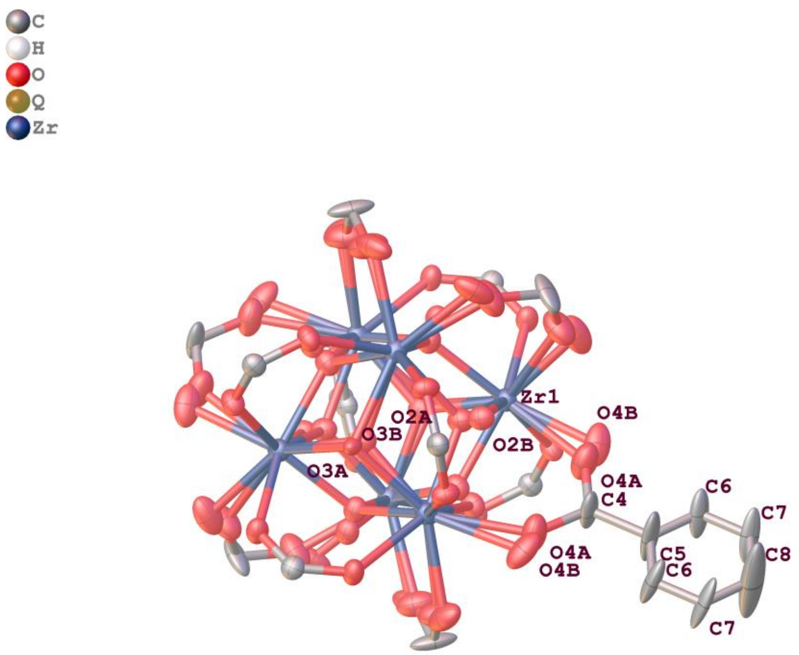

Figure A4.25. Partial structure of MOF-808-Bzz resolved from the single-crystal structure. Thermal ellipsoids are plotted with 50% probability.

Chart A4.1. DFT calculated Raman shift of Cu_2O_2 models. The reported Raman shifts are multiplied by 0.966 following the vibrational scaling factor.[30]

MOF-808-His-Cu

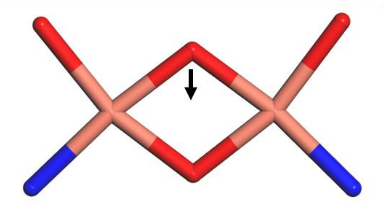

561 cm^{-1}

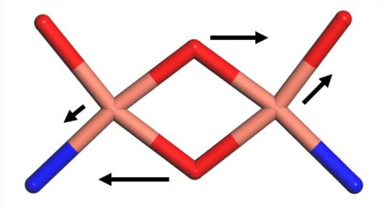

621 cm^{-1}

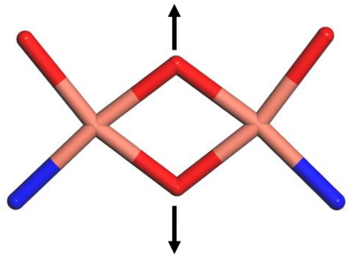

626 cm^{-1}

MOF-808-Iza-Cu

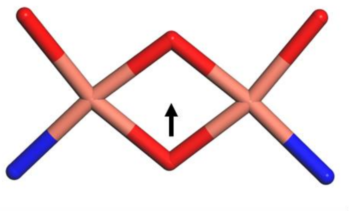

625 cm^{-1}

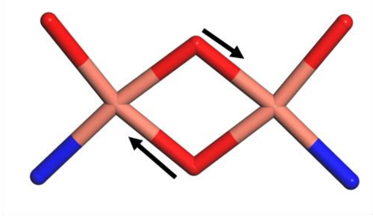

626 cm^{-1}

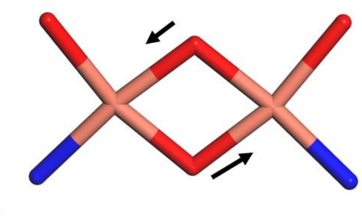

632 cm^{-1}

MOF-808-Bzz-Cu

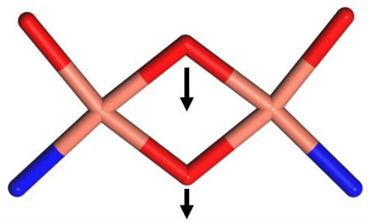

566 cm^{-1}

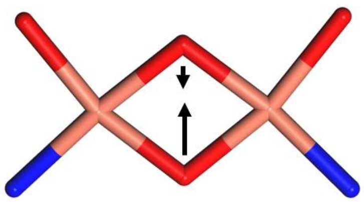

623 cm^{-1}

Table A4.5. XYZ coordinates for DFT optimized MOF-808-Bzz-Cu.

O	22.8655	26.2385	18.3411
O	11.7898	17.9039	23.5902
O	17.8916	14.7089	10.4660
O	13.1169	19.3225	24.8242
O	23.9866	25.1857	16.6293
O	16.6259	13.2810	11.7523
H	23.0978	27.0430	17.8426
H	11.0666	18.3715	24.0464
H	17.2861	14.4216	9.7585
C	23.3588	25.1449	17.6783
C	12.9888	18.4194	24.0092
C	17.5479	14.0757	11.6320
C	22.9918	23.9185	18.4718
C	18.5015	14.5320	12.7048
C	14.0868	17.6761	23.2947
C	15.4182	18.0913	23.3980
C	16.3858	17.3511	22.6965
C	16.0188	16.2264	21.9123
C	14.6823	15.8246	21.7986
C	13.7325	16.5557	22.4954
C	23.2212	22.6379	17.9588
C	22.8454	21.5421	18.7552
C	22.2534	21.7344	20.0308
C	22.0105	23.0187	20.5330
C	22.3865	24.0959	19.7453
C	18.2980	14.1779	14.0423
C	19.2269	14.6475	14.9872
C	20.3271	15.4528	14.5929
C	20.5172	15.8187	13.2547
C	19.6005	15.3497	12.3263
N	17.1816	15.7054	21.3392
C	18.1872	16.5038	21.7403
N	17.7787	17.4860	22.5666
N	21.9889	20.4752	20.5751
C	22.3776	19.5784	19.6509
N	22.9151	20.1524	18.5573
N	21.0629	15.7647	15.7389
C	20.4107	15.1962	16.7690
N	19.3245	14.5003	16.3815
Cu	17.2276	14.1960	20.1853
O	18.2369	14.8792	18.8742
Cu	18.2167	13.5997	17.6210
O	17.2788	12.8952	18.9648
Cu	22.6322	16.8365	15.7496
O	22.2054	17.9414	17.0919
Cu	23.5447	19.1308	17.0963
O	24.0013	17.9792	15.8129
Cu	18.9807	18.7575	23.2829
O	20.2711	19.8859	23.7761
Cu	21.1826	20.1854	22.2715
O	19.9391	18.9919	21.7879
H	22.2629	18.5118	19.7639
H	20.7149	15.2936	17.7993
H	19.2122	16.3815	21.4272
H	15.6571	18.9748	23.9809
H	14.3835	14.9936	21.1696
H	12.6898	16.2820	22.4246
H	23.6461	22.5298	16.9663
H	21.5209	23.1798	21.4869
H	22.2064	25.1022	20.0948
H	17.4279	13.5877	14.3108
H	21.3290	16.4677	12.9460
H	19.7085	15.6188	11.2857
O	18.1976	18.7985	25.0508
O	22.4028	21.3439	23.2337
O	25.1203	20.2030	16.7666
O	23.5254	15.8342	14.3515
O	17.9340	12.0273	16.5308
O	16.2179	13.0474	21.3762
H	17.5278	18.2113	25.4305
H	25.4991	20.9071	17.3127
H	17.3820	11.3049	16.8684
H	22.2832	21.4743	24.1871
H	23.1644	21.8400	22.9008
H	23.2249	15.0446	13.8789
H	24.4017	16.1177	14.0482
H	16.0081	12.1420	21.0997
H	15.8719	13.2373	22.2601
H	18.5801	19.3758	25.7298
H	25.7218	19.9592	16.0460
H	18.3822	11.7692	15.7122

Table A4.6. XYZ coordinates for DFT optimized MOF-808-Iza-Cu.

O	15.6790	23.9618	12.4297
O	13.2198	16.0569	24.7248
O	22.8456	11.1650	14.5702
O	12.7286	18.2878	24.4289
O	17.6041	23.2925	11.3568
O	22.7297	10.4798	16.7663
H	15.4835	24.3939	11.5783
H	12.4209	16.0662	25.2829
H	23.1171	10.2428	14.4097
C	16.8797	23.3147	12.3395
C	13.4237	17.3076	24.2120
C	22.6072	11.3369	15.9052
C	17.2671	22.6418	13.6061
C	22.2057	12.7267	16.2434
C	14.6386	17.3891	23.3608
C	16.8755	16.5412	22.5999
C	15.6199	16.4612	23.3269
C	17.1100	22.3326	16.0922
C	16.6997	22.8777	14.8092
C	22.0817	15.1838	15.7448
C	22.3538	13.7924	15.4264
N	17.4379	17.6830	22.0114
C	18.5920	17.3028	21.4374
N	18.8299	15.9897	21.6383
C	17.7605	15.5005	22.3623
N	21.8701	15.7316	17.0182
C	21.6437	17.0455	16.8494
N	21.7212	17.3929	15.5477
C	21.9917	16.2351	14.8451
N	18.3150	21.6771	16.3834
C	18.2719	21.3311	17.6812
N	17.1252	21.7441	18.2607
C	16.3875	22.3699	17.2751
Cu	20.3625	15.0321	21.0584
O	20.5131	15.7485	19.4239
Cu	21.9707	14.9491	18.7525
Cu	21.5270	19.1460	14.8469
O	21.2703	20.8411	14.3574
Cu	19.8621	21.3637	15.3164
Cu	16.6561	21.5263	20.0868
O	16.3570	21.1944	21.8129
Cu	16.8840	19.5060	22.0302
O	17.2362	19.8461	20.3054
O	20.1438	19.6763	15.8533
O	21.8393	14.2811	20.3994
H	14.6716	18.2973	22.7669
H	15.4741	15.5475	23.8976
H	18.0825	21.9377	13.4720
H	21.7877	12.8089	17.2419
H	15.8413	23.5436	14.8437
H	22.7135	13.6115	14.4166
H	19.2395	17.9586	20.8786
H	17.6653	14.4622	22.6392
H	21.4180	17.7324	17.6486
H	22.0740	16.2070	13.7698
H	19.0475	20.7843	18.1920
H	15.4012	22.7720	17.4466
O	16.5922	19.6295	23.9416
O	15.8516	23.2844	20.2498
O	20.5097	13.9794	22.6816
O	23.6883	14.0865	18.5077
O	22.9461	18.9468	13.5387
O	20.0538	23.1779	14.6640
H	15.4469	23.5011	21.1058
H	20.2856	14.2613	23.5810
H	23.0973	19.6980	12.9418
H	16.2374	20.4786	24.2549
H	16.1760	18.9000	24.4343
H	23.9895	13.5396	19.2527
H	23.9152	13.6483	17.6683
H	19.2761	23.7028	14.4034
H	20.7703	23.3160	14.0218
H	16.1260	24.0950	19.7956
H	21.2146	13.3117	22.7060
H	23.7588	18.4284	13.6353

Table A4.7. XYZ coordinates for DFT optimized MOF-808-His-Cu.

O	15.3201	24.8040	14.0507
O	17.1267	17.7002	26.9338
O	25.3683	13.9674	15.1931
O	16.1149	19.7500	26.6483
O	17.0920	24.4448	12.6232
O	25.8425	13.4728	17.3924
H	15.1039	25.5995	13.5214
H	16.9881	17.8083	27.8975
H	26.2186	13.5438	14.9540
C	16.4198	24.1525	13.5700
C	16.6517	18.7669	26.2254
C	25.1436	13.9400	16.5398
C	16.6198	22.9373	14.5115
C	23.7767	14.6431	16.7410
C	16.9498	18.4371	24.7402
C	16.3998	16.5432	22.9903
C	16.0464	17.2497	24.2763
C	15.2604	20.8329	15.3332
C	15.4581	21.9143	14.2992
C	21.2813	14.3741	15.9335
C	22.6372	13.7494	16.1545
N	15.7780	16.7290	21.7480
C	16.3451	15.8491	20.8943
N	17.2720	15.0888	21.5058
C	17.3177	15.5175	22.8232
N	20.1608	14.2314	16.7634
C	19.1443	14.8846	16.1592
N	19.5237	15.4167	14.9828
C	20.8658	15.1051	14.8310
N	15.6684	19.4967	15.2194
C	15.2267	18.8603	16.3261
N	14.5385	19.687	17.1347
C	14.5551	20.9307	16.5229
Cu	18.3125	13.6649	20.7531
O	19.3183	12.4649	19.9023
Cu	19.8069	13.2154	18.3623
Cu	18.4478	16.3835	13.7242
O	17.5766	17.4717	14.8614
Cu	16.5045	18.4730	13.8170
Cu	13.6635	19.2619	18.7870
O	14.9544	18.2706	19.5534
Cu	14.2805	17.7853	21.1513
O	13.0183	18.7741	20.3749
O	17.3824	17.3886	12.7092
O	18.7976	14.4451	19.2064
H	16.8323	19.3300	24.1250
H	16.0391	16.5099	25.0849
H	17.6077	22.5008	14.3591
H	23.6299	14.8876	17.7938
H	14.528	22.4885	14.2194
H	22.9937	13.3527	15.1971
H	16.0877	15.7726	19.8501
H	17.9331	15.0253	23.5622
H	18.1533	14.9713	16.575
H	21.4105	15.3523	13.9314
H	15.4106	17.8186	16.5347
H	14.0107	21.7721	16.9262
H	15.0303	17.6532	24.224
H	15.6286	21.4729	13.3122
H	22.5572	12.8908	16.8286
N	18.4341	18.0459	24.7045
H	18.6781	17.5599	23.8314
H	18.6245	17.4266	25.5110
N	23.8881	15.9676	15.9724
H	24.3407	15.7759	15.0621
H	24.4845	16.6441	16.4692
N	16.588	23.5188	15.9322
H	17.4553	24.0285	16.1516
H	16.449	22.7856	16.6401
O	18.0916	12.4858	22.2839
O	20.7576	11.5861	17.8405
O	19.1802	15.4778	12.1668
O	15.5143	19.2462	12.3162
O	13.1263	17.4845	22.7030
O	12.0638	20.2921	18.3843
H	17.2471	12.2759	22.7159
H	18.6552	11.6917	22.3080
H	18.9598	15.8575	11.2973
H	19.2731	14.5159	12.0668
H	11.5575	20.2455	17.5564
H	11.4400	20.4346	19.1187
H	20.5979	11.0968	17.0155
H	14.5443	19.2823	12.2577
H	12.3342	18.0518	22.7410
H	20.8796	10.9355	18.5565
H	15.8597	19.0147	11.4343
H	12.8831	16.6077	23.0459
H	19.0446	18.8689	24.8053
H	22.9656	16.3948	15.8156
H	15.8133	24.2025	15.9843

4.6 References

(1) (a) Periana, R. A.; Taube, D. J.; Evitt, E. R.; Löffler, D. G.; Wentrcek, P. R.; Voss, G.; Masuda, T., *Science* **1993,** *259*, 340; (b) Groothaert, M. H.; Smeets, P. J.; Sels, B. F.; Jacobs, P. A.; Schoonheydt, R. A., *J. Am. Chem. Soc.* **2005,** *127*, 1394; (c) Woertink, J. S.; Smeets, P. J.; Groothaert, M. H.; Vance, M. A.; Sels, B. F.; Schoonheydt, R. A.; Solomon, E. I., *Proc. Natl. Acad. Sci. U.S.A.* **2009,** *106*, 18908; (d) Hammond, C.; Forde, M. M.; Rahim, A.; Hasbi, M.; Thetford, A.; He, Q.; Jenkins, R. L.; Dimitratos, N.; Lopez-Sanchez, J. A.; Dummer, N. F., *Angew. Chem. Int. Ed.* **2012,** *51*, 5129; (e) Grundner, S.; Markovits, M. A.; Li, G.; Tromp, M.; Pidko, E. A.; Hensen, E. J.; Jentys, A.; Sanchez-Sanchez, M.; Lercher, J. A., *Nat. Commun.* **2015,** *6*, 7546; (f) Narsimhan, K.; Iyoki, K.; Dinh, K.; Román-Leshkov, Y., *ACS Cent. Sci.* **2016,** *2*, 424; (g) Sushkevich, V. L.; Palagin, D.; Ranocchiari, M.; van Bokhoven, J. A., *Science* **2017,** *356*, 523; (h) Tomkins, P.; Mansouri, A.; Bozbag, S. E.; Krumeich, F.; Park, M. B.; Alayon, E. M. C.; Ranocchiari, M.; Bokhoven, J. A. v., *Angew. Chem. Int. Ed.* **2016,** *55*, 5467.

(2) (a) Lawton, T. J.; Rosenzweig, A. C., *J. Am. Chem. Soc.* **2016,** *138*, 9327; (b) Ravi, M.; Ranocchiari, M.; van Bokhoven, J. A., *Angew. Chem. Int. Ed.* **2017**; (c) Schoedel, A.; Ji, Z.; Yaghi, O. M., *Nat. Energy* **2016,** *1*, 16034.

(3) Balasubramanian, R.; Smith, S. M.; Rawat, S.; Yatsunyk, L. A.; Stemmler, T. L.; Rosenzweig, A. C., *Nature* **2010,** *465*, 115.

(4) (a) Culpepper, M. A.; Cutsail III, G. E.; Hoffman, B. M.; Rosenzweig, A. C., *J. Am. Chem. Soc.* **2012,** *134*, 7640; (b) Culpepper, M. A.; Cutsail III, G. E.; Gunderson, W. A.; Hoffman, B. M.; Rosenzweig, A. C., *J. Am. Chem. Soc.* **2014,** *136*, 11767; (c) Cao, L.; Caldararu, O.; Rosenzweig, A. C.; Ryde, U., *Angew. Chem. Int. Ed.* **2018,** *57*, 162.

(5) (a) Elwell, C. E.; Gagnon, N. L.; Neisen, B. D.; Dhar, D.; Spaeth, A. D.; Yee, G. M.; Tolman, W. B., *Chem. Rev.* **2017,** *117*, 2059; (b) Mirica, L. M.; Ottenwaelder, X.; Stack, T. D. P., *Chem. Rev.* **2004,** *104*, 1013; (c) Solomon, E. I.; Ginsbach, J. W.; Heppner, D. E.; Kieber-Emmons, M. T.; Kjaergaard, C. H.; Smeets, P. J.; Tian, L.; Woertink, J. S., *Faraday Discuss.* **2011,** *148*, 11.

(6) Citek, C.; Herres-Pawlis, S.; Stack, T. D. P., *Acc. Chem. Res.* **2015,** *48*, 2424.

(7) Que Jr, L.; Tolman, W. B., *Angew. Chem. Int. Ed.* **2002,** *41*, 1114.

(8) Pappas, D. K.; Borfecchia, E.; Dyballa, M.; Pankin, I. A.; Lomachenko, K. A.; Martini, A.; Signorile, M.; Teketel, S.; Arstad, B.; Berlier, G., *J. Am. Chem. Soc.* **2017,** *139*, 14961.

(9) (a) Wang, V. C.-C.; Maji, S.; Chen, P. P.-Y.; Lee, H. K.; Yu, S. S.-F.; Chan, S. I., *Chem. Rev.* **2017,** *117*, 8574; (b) Lu, Y.; Yeung, N.; Sieracki, N.; Marshall, N. M., *Nature* **2009,** *460*, 855; (c) Lillerud, K. P.; Olsbye, U.; Tilset, M., *Top. Catal.* **2010,** *53*, 859; (d) Xiao, D. J.; Bloch, E. D.; Mason, J. A.; Queen, W. L.; Hudson, M. R.; Planas, N.; Borycz, J.; Dzubak, A. L.; Verma, P.; Lee, K., *Nat. Chem.* **2014,** *6*, 590; (e) Gu, Z. Y.; Park, J.; Raiff, A.; Wei, Z.; Zhou, H. C., *ChemCatChem* **2014,** *6*, 67.

(10) Furukawa, H.; Cordova, K. E.; O'Keeffe, M.; Yaghi, O. M., *Science* **2013,** *341*, 1230444.

(11) (a) Rungtaweevoranit, B.; Diercks, C. S.; Kalmutzki, M. J.; Yaghi, O. M., *Faraday Discuss.* **2017,** *201*, 9; (b) Osborn Popp, T. M.; Yaghi, O. M., *Acc. Chem. Res.* **2017,** *50*, 532; (c) Fracaroli, A. M.; Siman, P.; Nagib, D. A.; Suzuki, M.; Furukawa, H.; Toste, F. D.; Yaghi, O. M., *J. Am. Chem. Soc.* **2016,** *138*, 8352; (d) O'Keeffe, M.; Yaghi, O. M., *Chem. Rev.* **2011,** *112*, 675.

(12) (a) Lee, S.; Kapustin, E. A.; Yaghi, O. M., *Science* **2016,** *353*, 808; (b) Deria, P.; Mondloch, J. E.; Tylianakis, E.; Ghosh, P.; Bury, W.; Snurr, R. Q.; Hupp, J. T.; Farha, O. K., *J. Am. Chem. Soc.* **2013,** *135*, 16801; (c) Yuan, S.; Lu, W.; Chen, Y.-P.; Zhang, Q.; Liu, T.-F.; Feng, D.; Wang, X.; Qin, J.; Zhou, H.-C., *J. Am. Chem. Soc.* **2015,** *137*, 3177.

(13) (a) Manna, K.; Zhang, T.; Lin, W., *J. Am. Chem. Soc.* **2014,** *136*, 6566; (b) Doonan, C. J.; Morris, W.; Furukawa, H.; Yaghi, O. M., *J. Am. Chem. Soc.* **2009,** *131*, 9492.

(14) Furukawa, H.; Gándara, F.; Zhang, Y.-B.; Jiang, J.; Queen, W. L.; Hudson, M. R.; Yaghi, O. M., *J. Am. Chem. Soc.* **2014,** *136*, 4369.

(15) Choi, K. M.; Jeong, H. M.; Park, J. H.; Zhang, Y.-B.; Kang, J. K.; Yaghi, O. M., *ACS Nano* **2014,** *8*, 7451.

(16) Blatter, F.; Moreau, F.; Frei, H., *J. Phys. Chem.* **1994,** *98*, 13403.

(17) (a) Becke, A. D., *J. Chem. Phys.* **1993,** *98*, 5648; (b) Lee, C.; Yang, W.; Parr, R. G., *Phys. Rev. B* **1988,** *37*, 785.

(18) Frisch, M. J.; Trucks, G. W.; Schlegel, H. B.; Scuseria, G. E.; Robb, M. A.; Cheeseman, J. R.; Scalmani, G.; Barone, V.; Petersson, G. A.; Nakatsuji, H.; Li, X.; Caricato, M.; Marenich, A. V.; Bloino, J.; Janesko, B. G.; Gomperts, R.; Mennucci, B.; Hratchian, H. P.; Ortiz, J. V.; Izmaylov, A. F.; Sonnenberg, J. L.; Williams; Ding, F.; Lipparini, F.; Egidi, F.; Goings, J.; Peng, B.; Petrone, A.; Henderson, T.; Ranasinghe, D.; Zakrzewski, V. G.; Gao, J.; Rega, N.; Zheng, G.; Liang, W.; Hada, M.; Ehara, M.; Toyota, K.; Fukuda, R.; Hasegawa, J.; Ishida, M.; Nakajima, T.; Honda, Y.; Kitao, O.; Nakai, H.; Vreven, T.; Throssell, K.; Montgomery Jr., J. A.; Peralta, J. E.; Ogliaro, F.; Bearpark, M. J.; Heyd, J. J.; Brothers, E. N.; Kudin, K. N.; Staroverov, V. N.; Keith, T. A.; Kobayashi, R.; Normand, J.; Raghavachari, K.; Rendell, A. P.; Burant, J. C.; Iyengar, S. S.; Tomasi, J.; Cossi, M.; Millam, J. M.; Klene, M.; Adamo, C.; Cammi, R.; Ochterski, J. W.; Martin, R. L.; Morokuma, K.; Farkas, O.; Foresman, J. B.; Fox, D. J. *Gaussian 16 Rev. A.03*, Wallingford, CT, 2016.

(19) Marcus, M. A.; MacDowell, A. A.; Celestre, R.; Manceau, A.; Miller, T.; Padmore, H. A.; Sublett, R. E., *J. Synchrotron Radiat.* **2004,** *11*, 239.

(20) Kelly, S.; Hesterberg, D.; Ravel, B., *Methods of soil analysis. Part 5. Mineralogical methods* **2008,** *5*, 387.

(21) (a) Ravel, B.; Newville, M., *J. Synchrotron Radiat.* **2005,** *12*, 537; (b) Newville, M., *J. Synchrotron Radiat.* **2001,** *8*, 322.

(22) Ikuno, T.; Zheng, J.; Vjunov, A.; Sanchez-Sanchez, M.; Ortuño, M. A.; Pahls, D. R.; Fulton, J. L.; Camaioni, D. M.; Li, Z.; Ray, D., *J. Am. Chem. Soc.* **2017,** *139*, 10294.

(23) Zubavichus, Y.; Shaporenko, A.; Grunze, M.; Zharnikov, M., *J. Phys. Chem. A* **2005,** *109*, 6998.

(24) Kau, L. S.; Spira-Solomon, D. J.; Penner-Hahn, J. E.; Hodgson, K. O.; Solomon, E. I., *J. Am. Chem. Soc.* **1987,** *109*, 6433.

(25) (a) Shadle, S. E.; Penner-Hahn, J. E.; Schugar, H. J.; Hedman, B.; Hodgson, K. O.; Solomon, E. I., *J. Am. Chem. Soc.* **1993,** *115*, 767; (b) Kau, L. S.; Hodgson, K. O.; Solomon, E. I., *J. Am. Chem. Soc.* **1989,** *111*, 7103.

(26) Groothaert, M. H.; van Bokhoven, J. A.; Battiston, A. A.; Weckhuysen, B. M.; Schoonheydt, R. A., *J. Am. Chem. Soc.* **2003,** *125*, 7629.

(27) (a) Mahadevan, V.; Hou, Z.; Cole, A. P.; Root, D. E.; Lal, T. K.; Solomon, E. I.; Stack, T., *J. Am. Chem. Soc.* **1997,** *119*, 11996; (b) Kang, P.; Bobyr, E.; Dustman, J.; Hodgson, K. O.; Hedman, B.; Solomon, E. I.; Stack, T. D. P., *Inorg. Chem.* **2010,** *49*, 11030; (c) Smeets, P. J.; Hadt, R. G.; Woertink, J. S.; Vanelderen, P.; Schoonheydt, R. A.; Sels, B. F.; Solomon, E. I., *J. Am. Chem. Soc.* **2010,** *132*, 14736; (d) Kim, Y.; Kim, T. Y.; Lee, H.; Yi, J., *Chem. Commun.* **2017,** *53*, 4116.

(28) Tromp, M.; van Bokhoven, J. A.; Arink, A. M.; Bitter, J. H.; van Koten, G.; Koningsberger, D. C., *Chemistry-A European Journal* **2002,** *8*, 5667.

(29) (a) Herres-Pawlis, S.; Verma, P.; Haase, R.; Kang, P.; Lyons, C. T.; Wasinger, E. C.; Flörke, U.; Henkel, G.; Stack, T. D. P., *J. Am. Chem. Soc.* **2009,** *131*, 1154; (b) DuBois, J. L.; Mukherjee, P.; Stack, T.; Hedman, B.; Solomon, E. I.; Hodgson, K. O., *J. Am. Chem. Soc.* **2000,** *122*, 5775.

(30) NIST Computational Chemistry Comparison and Benchmark Database, NIST Standard Reference Database Number 101. Release 17b, September 2015, Editor: Russell D. Johnson III. http://cccbdb.nist.gov/

Chapter 5

Investigation of Metalated Frameworks for Hydrogen Storage

5.1 Introduction

Reversible hydrogen storage is an important challenge with respect to the development of practical on-board hydrogen fuel cells for light-duty vehicles.[1] Current technologies employ high-pressure gas cylinders (up to 700 bar) that store an adequate amount of hydrogen gas to achieve driving distances comparable to those of automobiles fueled by gasoline.[2] The low compressibility of hydrogen gas requires these cylinders to occupy large storage space with thick walls to sustain such pressures without rupturing.[3] This has led to challenges with both volumetric and gravimetric hydrogen capacity. Metal hydrides such MgH_2, $MgBH_4$ exhibit moderate gravimetric capacities, but suffer from sluggish kinetics that requires heating cycles for storage and delivery.[4] A promising alternative strategy involves the use of porous media to physisorb hydrogen molecules. Physisorption allows for fast charge and discharge of the media under ambient temperature and moderate pressure.[5] However, hydrogen molecules have extremely small dipole moments compared to other gases making it difficult for hydrogen to interact with porous media with sufficient strength for storing hydrogen with high volumetric/gravimetric capacity.[6]

Among porous media, MOFs possess many desirable attributes for hydrogen storage. They are highly porous and their interior surfaces can be altered or functionalized systematically.[7] Extensive study on hydrogen adsorption properties of MOFs has shown that MOFs are promising candidates as sorbent materials that can reach the DOE target for gravimetric uptake albeit at 77 K.[8] Systematic studies also indicate a linear correlation between gravimetric uptake and surface area at this temperature and high pressure (1–26 bars).[9] However, at operating temperature such as 298 K, the gravimetric uptake decreases dramatically, signifying the weak interaction between hydrogen adsorbate molecules and the frameworks.[10] To enhance this interaction, several strategies have been developed including catenation and adsorption on open metal sites.[11] Of these parameters, a high density of cationic open metal sites has been shown to effectively enhance the framework interaction with hydrogen molecules. During the synthesis of MOFs, solvent molecules remain as ligands on the metal clusters. These solvent molecules can be removed upon evacuation to create coordinatively unsaturated open metal sites.[12] Open metal sites can interact with hydrogen molecules through charge-induced dipole interaction which greatly increases the heat of adsorption.[13] Among many MOFs that utilize this interaction, Ni_2(*m*-dobdc), a MOF-74 analogue, has been reported to exhibit the highest observed volumetric hydrogen uptake (12.1 g L^{-1} at 25 °C and 100 bar) with adsorption enthalpy of up to 13.7 kJ mol^{-1} at zero coverage (Figure 5.1).[14] However, these values remain below the DOE 2025 targets for hydrogen storage (40 g L^{-1}) which prompts further research.

In this chapter, Mg-IRMOF-74-III was chosen as a platform for introducing additional open metal sites due to its surface area, high chemical stability and the availability of open metal sites which can interact with hydrogen molecules.[15] The organic linker of this MOF was functionalized with primary amines which were post-synthetically modified (PSM) to install metal-binding ligands for subsequent metalations.[16] The resulting materials were investigated for hydrogen adsorption properties.

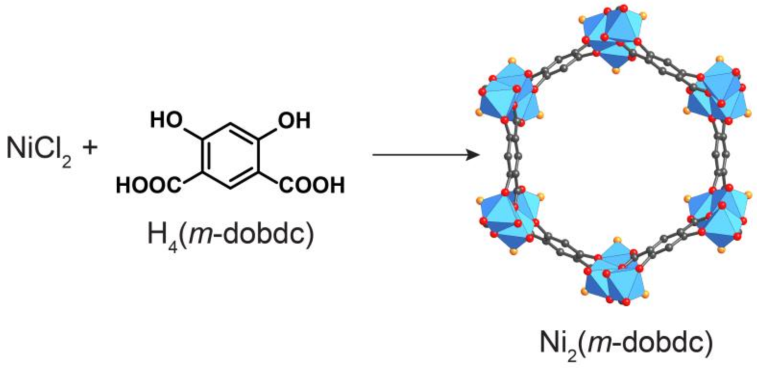

Figure 5.1. Construction of Ni$_2$(*m*-dobdc) which comprises Ni-O rods and H$_4$(*m*-dobdc). Atom labeling scheme: C, black; O, red; Ni, blue polyhedra; open metal site, orange. H atoms are omitted for clarity.

5.2 Experimental Section

Chemicals used in this work. All chemicals unless noted were obtained from Sigma-Aldrich. Anhydrous methanol was obtained EMD Millipore Chemicals. These chemicals were used without further purification.

Analytical techniques. Powder X-ray diffraction patterns (PXRD) were recorded using a Bruker D8 Advance diffractometer (Göbel-mirror monochromated Cu Kα radiation λ = 1.54056 Å). Gas adsorption analyses were performed on a Quantachrome Quadrasorb-SI automatic volumetric gas adsorption analyzer. A liquid nitrogen bath (77 K), ultra-high purity grade N_2 and He (99.999%, Praxair) were used for the measurements. The amounts of metals in the samples were analyzed by an ICP–AES spectroscope (Optima 7000 DV, Perkin Elmer). The samples were digested in a solution mixture of nitric acid, hydrochloric acid in 70 °C water bath for an hour. The resulting solutions were diluted with milliQ water to 10 mL before the measurement. Elemental microanalyses (EA) were performed in the Microanalytical Laboratory at the College of Chemistry, UC Berkeley using a Perkin Elmer 2400 Series II CHNS elemental analyzer.

Synthesis of Materials:

Mg-MOF-74. Mg-MOF-74 was synthesized with slight modifications from the reported procedure.[17] In a 20-mL scintillation vial, $Mg(NO_3)\cdot 6H_2O$ (116 mg, 0.450 mmol) and 2,5-dihydroxy-1,4-benzenedicarboxylic acid (30 mg, 0.151 mmol). The reaction was heated in a 120 °C isothermal oven for a day. Yellow microcrystalline powder was washed with DMF 5 times (10 mL × 5) over 48 h period and with anhydrous methanol 5 times (10 mL × 5) over 48 h period.

Mg-IRMOF-74-III-(CH_2NH_2)$_2$. Mg-IRMOF-74-III was synthesized according to the reported procedure.[16] The resulting pale-yellow powder (~100 mg) was washed with DMF 3 times (10 mL × 3) over 24 h period and with ethyl acetate 3 times (10 mL × 3) over 24 h period.

Mg-IRMOF-74-III-$(CH_2NH_2)_2$-2OHBAL. In a 20-mL scintillation vial, Mg-IRMOF-74-III-$(CH_2NH_2)_2$ was added to a solution of 2-hydroxybenzaldehyde (537 mg) dissolved in ethyl acetate (5 mL). The suspension was allowed to react at room temperature for 18 h. Orange powder was washed with ethyl acetate 5 times (20 mL × 5) over 48 h period. For material characterization, the sample was dried under vacuum at 120 °C for 6 h.

Mg-IRMOF-74-III-$(CH_2NH_2)_2$-34OHBAL. In a 20-mL scintillation vial, Mg-IRMOF-74-III-$(CH_2NH_2)_2$ was added to a solution of 3,4-hydroxybenzaldehyde (607 mg) dissolved in ethyl acetate (20 mL). The suspension was allowed to react at room temperature for 18 h. Red powder was washed with ethyl acetate 5 times (20 mL × 5) over 48 h period. For material characterization, the sample was dried under vacuum at 120 °C for 6 h.

Mg-IRMOF-74-III-$(CH_2NH_2)_2$-2OHBAL-Ni. Mg-IRMOF-74-III-$(CH_2NH_2)_2$-2OHBAL (~30 mg) was washed with anhydrous MeOH 3 times (20 mL × 3). The MOF was added to a solution of $Ni(OAc)_2{\cdot}4H_2O$ (197 mg) dissolved in anhydrous MeOH (6 mL). The suspension was allowed to react at room temperature for 7 days. Yellow powder was washed with anhydrous MeOH 5 times (10 mL × 5) over 48 h period.

Mg-IRMOF-74-III-$(CH_2NH_2)_2$-34OHBAL-Ni. Mg-IRMOF-74-III-$(CH_2NH_2)_2$-34OHBAL (~30 mg) was washed with anhydrous MeOH 3 times (20 mL × 3). The MOF was added to a solution of $Ni(OAc)_2{\cdot}4H_2O$ (197 mg) dissolved in anhydrous MeOH (6 mL). The suspension was allowed to react at room temperature for 7 days. Red powder was washed with anhydrous MeOH 5 times (10 mL × 5) over 48 h period.

Solution ^1H NMR of digested samples:

Solution ^1H NMR spectra of digested samples were acquired on a Bruker AVB-400 (400 MHz) spectrometer at 297–300 K. Samples of MOFs (~5 mg) were digested and sonicated in a mixture of DMSO-*d6* (500 μL) and 35 wt.% DCl in D_2O (20 μL). The suspension was heated with a heat gun until the solution clarified.

Nitrogen adsorption measurements:

Gas adsorption analyses were performed on a Quantachrome Quadrasorb-SI automatic volumetric gas adsorption analyzer. A liquid nitrogen bath (77 K), ultra-high purity grade N_2 and He (99.999%, Praxair) were used for the measurements. The samples were prepared and measured after evacuating at 180 °C with a heating rate of 0.1 K min^{-1} for 12 h.

Hydrogen adsorption measurements:

Measurements were performed using a Quantachrome Autosorb instrument. Ca. 30 mg of guest free samples in 9 mm bulb gas cells were charged with argon to avoid air contamination and the cells were mounted on the instrument. A liquid nitrogen bath (77 K), ultra-high purity grade H_2 and He (99.999%, Praxair) were used for the measurements. The samples were prepared and measured after evacuating at 180 °C with a heating rate of 0.1 K min^{-1} for 12 h.

X-ray photoelectron spectroscopy analysis (XPS):

Chemical characterization of the catalyst was performed using a Thermo Scientific K-Alpha X-ray photoelectron spectrometer (XPS) with a monochromatic Al X-ray source (Kα=1486.7 eV). High-resolution spectra of Ni 2p regions were obtained with analyzer pass energy of 50 eV and 0.1 eV energy steps. The binding energy was corrected using adventitious C 1s peak.

5.3 Results and Discussion

Mg-IRMOF-74-$(CH_2NH_2)_2$ was employed as a platform for post-synthetic modification to install metal-binding ligands. This MOF is constructed from magnesium oxide rods of composition $[O_2Mg_2](-CO_2)_2$ linked with hydroxy and carboxylate groups of terphenylene organic linkers bearing primary amine functionalities (Figure 5.2). The available primary amine groups on the organic linker were used as an anchor for the incorporation of metal-binding ligands due to its ability to react with a wide range of substrates. Mg-IRMOF-74-$(CH_2NH_2)_2$, Mg_2(2′,5′-bis(aminomethyl)-3,3″-dioxido-[1,1′:4′,1″-terphenyl]-4,4″-dicarboxylate), was synthesized according to the reported protocol.[16]

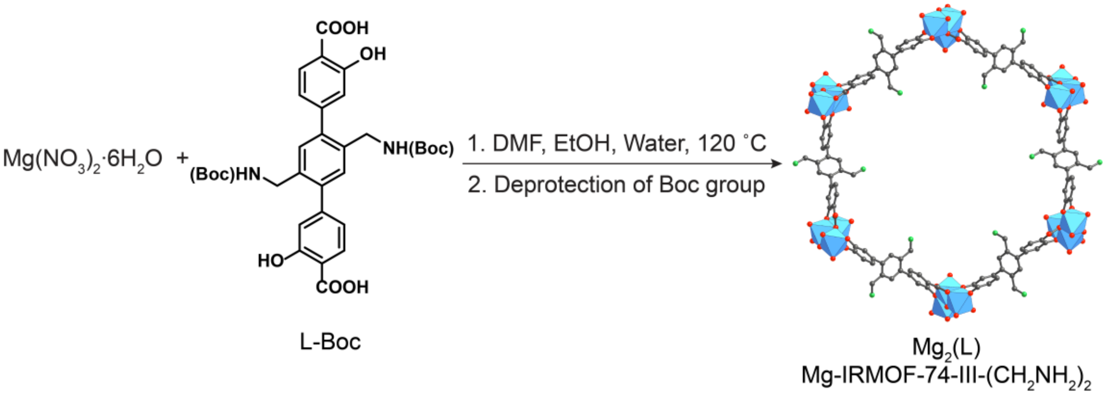

Figure 5.2. Synthesis of Mg-IRMOF-74-$(CH_2NH_2)_2$.

Imine condensation was selected as a method for installing ligands in the MOF because this reaction can proceed under ambient conditions and no sterically o bulky leaving group is involved in the process, allowing the reaction to occur with high yields without disadvantageous effects from diffusion issues.[18] In this work, the primary amines of the MOF reacted with 2-hydroxybenzaldehyde to produce Mg-IRMOF-74-2OHBAL and with 3,4-dihydroxybenzaldehyde to give Mg-IRMOF-74-34OHBAL (Figure 5.3). These two ligands were chosen based on literature precedent for their ability to bind to a wide variety of metals.[19] Additionally, the catecholate functionality in Mg-IRMOF-74-34OHBAL can theoretically benefit hydrogen storage based on the fact that this ligand is highly polarizing.[6a] Powder X-ray diffraction (PXRD) analysis indicates that the materials retain their crystallinity and phase purity of the parent material after PSM (Figure 5.4a). N_2 adsorption isotherms performed at 77 K show that these materials remain porous after these processes as well (BET surface area of Mg-IRMOF-74-2OHBAL = 840 and Mg-IRMOF-

74-34OHBAL = 905 m^2 g^{-1}) (Figure 5.4b). MOFs were digested in DCl/DMSO-d_6 to determine the extent of imine bond formation in these MOFs which show the quantitative reaction of primary amines with both aldehyde derivatives. Due to imine bond's sensitivity to acid, only hydrolyzed products were observed from digestion ^{1}H-NMR. To confirm the presence of imine bonds in both materials, Fourier-transform infrared spectroscopy (FT-IR) was performed. The results indicate the presence of imine stretches at 1629 and 1639 cm^{-1} for -2OHBAL and -34OHBAL adducts, respectively (Figure 5.5). These characteristic imine stretches were corroborated by the spectra obtained from molecular model compounds.

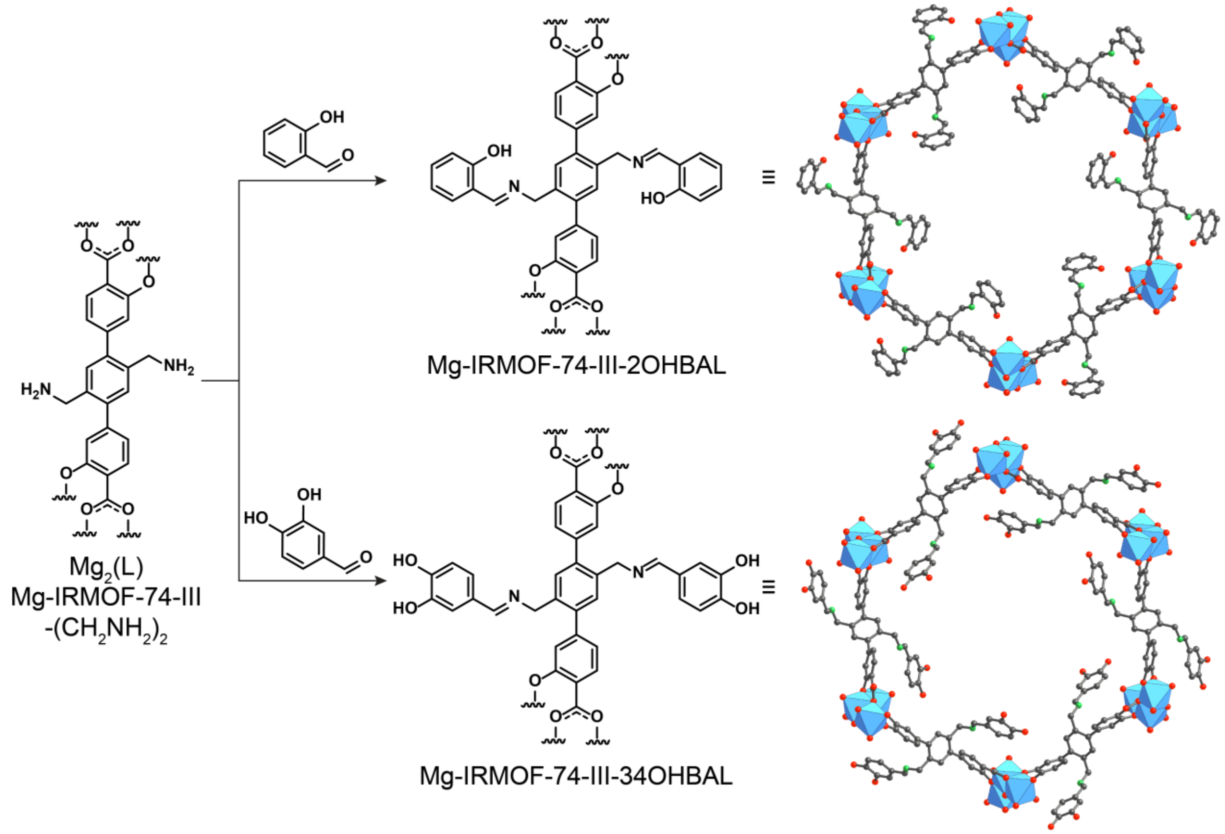

Figure 5.3. Post-synthetic modifications of Mg-IRMOF-74-III-(CH$_2$NH$_2$)$_2$ with 2-hydroxybenzaldehyde and 3,4-dihydroxybenzaldehyde to produce Mg-IRMOF-74-III-2OHBAL and Mg-IRMOF-74-III-34OHBAL, respectively.

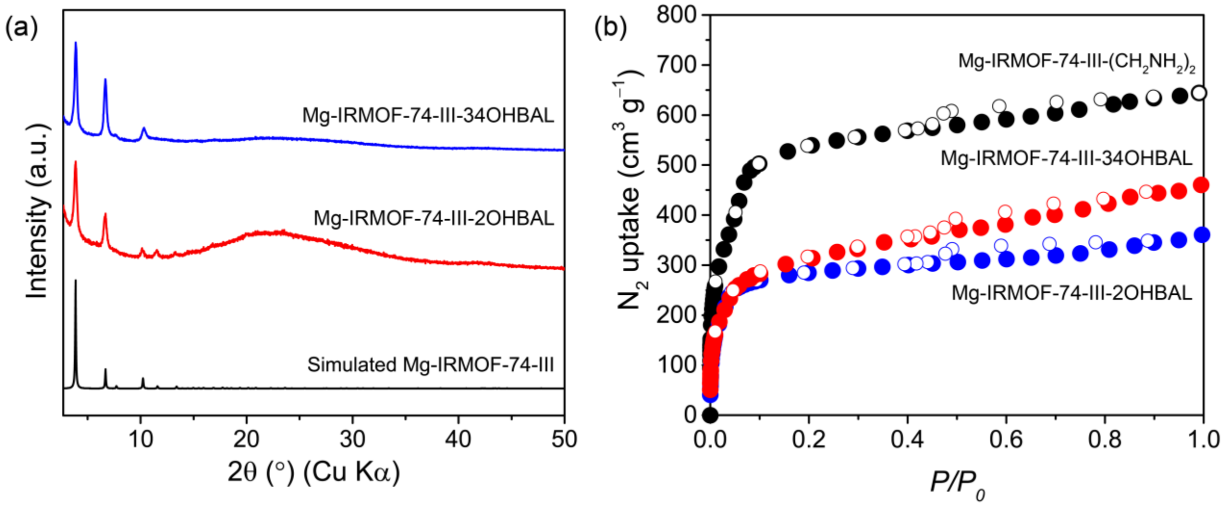

Figure 5.4. (a) Experimental PXRD patterns of functionalized Mg-IRMOF-74-III-$(CH_2NH_2)_2$ in comparison with simulated patterns of Mg-IRMOF-74-III-$(CH_2NH_2)_2$ and (b) N_2 adsorption-desorption isotherms at 77 K with adsorption and desorption points represented by closed circles and open circles, respectively ($P/P_\circ$, relative pressure).

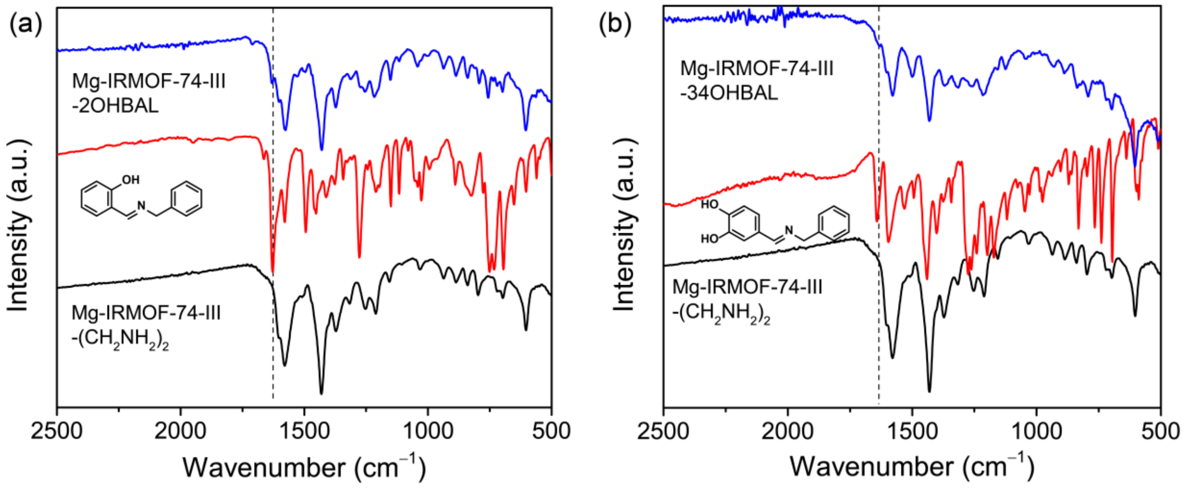

Figure 5.5. FT-IR spectra of Mg-IRMOF-74-III-2OHBAL and Mg-IRMOF-74-III-34OHBAL in comparison with their respective model compounds.

These functionalized MOFs were subsequently metalated with Ni(II) salts. Open metal sites of Ni(II) have been shown experimentally to the have highest hydrogen adsorption enthalpy among many divalent metals tested.[13] In this process, metalation conditions were optimized by screening reaction times between 1 day and 7 days and types of Ni salt including $Ni(OAc)_2 \cdot 4H_2O$, $NiCl_2 \cdot$glyme and $Ni(NO_3)_2 \cdot 6H_2O$. For Mg-IRMOF-74-2OHBAL, only Ni(II) from $Ni(OAc)_2 \cdot 4H_2O$ was found to be successfully incorporated into the MOF structure as indicated by inductively coupled plasma (ICP) analysis (Table 5.1). This material will be referred to as Mg-

IRMOF-74-2OHBAL-Ni. From ICP analysis, Ni/Mg molar ratio was found to be 0.43 translating to 43% metalation of the available ligands. Interestingly, Mg-IRMOF-74-III-34OHBAL can be metalated with all Ni(II) salts tested including $Ni(OAc)_2 \cdot 4H_2O$, $NiCl_2 \cdot$glyme and $Ni(NO_3)_2 \cdot 6H_2O$ to give Ni/Mg molar ratios of 0.44, 0.22 and 0.33, respectively. As a control experiment, Mg-MOF-74 which is a Mg-IRMOF-74-III analog with 2,5-dioxido-1,4-benzenedicarboxylate as organic linker was synthesized and tested for metalation under similar condition. Negligible incorporation of Ni(II) was found confirming that Ni(II) was bound to the ligands in Mg-IRMOF-74-2OHBAL and Mg-IRMOF-74-34OHBAL. Additionally, we performed X-ray photoelectron spectroscopy of metalated samples to probe the change in the electronic properties of Ni(II) after metalation. High-resolution Ni 2p XPS spectra of these samples show two regions assigned as Ni(II) $2p_{3/2}$ and satellites (Figure 5.6).[20] $Ni(OAc)_2 \cdot 4H_2O$, Mg-IRMOF-74-2OHBAL-Ni and Mg-IRMOF-74-34OHBAL-Ni (metalated with $Ni(OAc)_2 \cdot 4H_2O$) exhibit the binding energies of 856.2, 855.8 and 855.9 eV, respectively. The decreased binding energies after metalation indicate the increase in the electron donor ability of the ligands appended to the MOF.[21] PXRD analysis indicates that these materials remain crystalline and FT-IR spectra show that imine bonds remain intact (Figure 5.7).

Table 5.1. ICP analysis of Ni(II) incorporated in functionalized Mg-IRMOF-74-III-$(CH_2NH_2)_2$.

MOF	Ni salts	Ni/Mg molar ratio
Mg-IRMOF-74-III-2OHBAL	$Ni(OAc)_2 \cdot 4H_2O$	0.43
	$NiCl_2 \cdot$glyme	0.09
	$Ni(NO_3)_2 \cdot 6H_2O$	0.06
Mg-IRMOF-74-III-34OHBAL	$Ni(OAc)_2 \cdot 4H_2O$	0.44
	$NiCl_2 \cdot$glyme	0.22
	$Ni(NO_3)_2 \cdot 6H_2O$	0.33

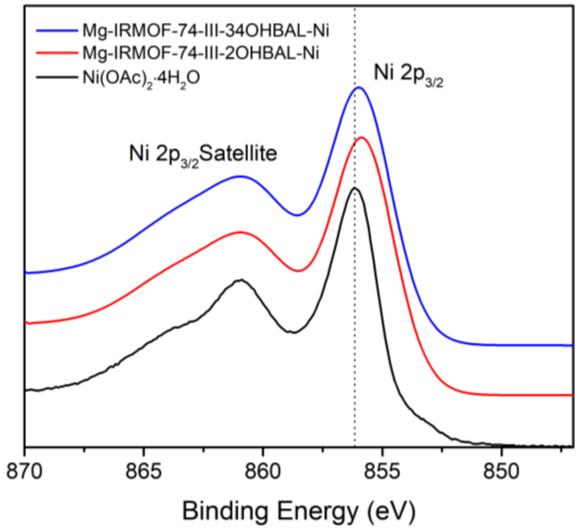

Figure 5.6. XPS Ni 2p$_{3/2}$ spectra of Mg-IRMOF-74-III-$(CH_2NH_2)_2$-2OHBAL-Ni and Mg-IRMOF-74-III-$(CH_2NH_2)_2$-34OHBAL-Ni in comparison with the Ni(II) precursor which is $Ni(OAc)_2·4H_2O$.

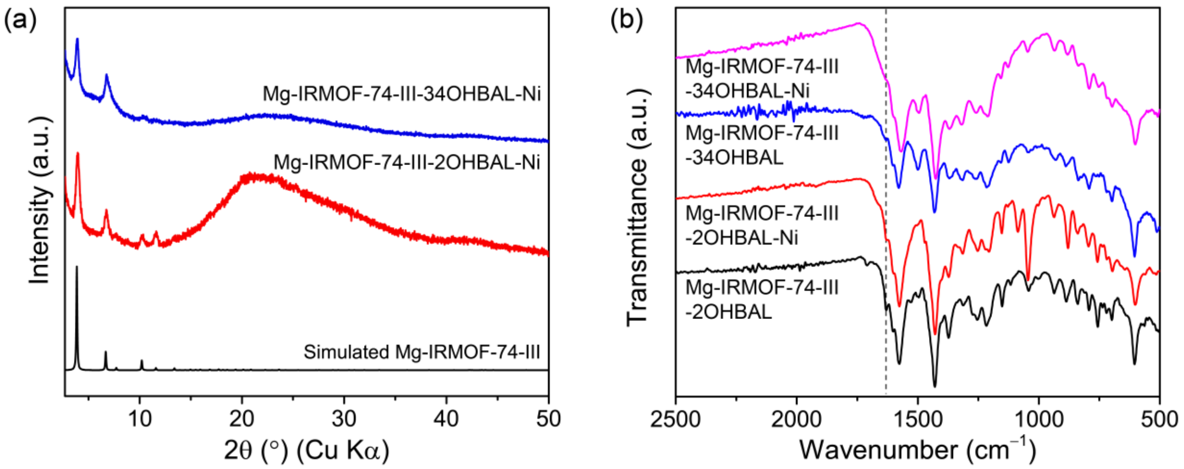

Figure 5.7. (a) Experimental PXRD patterns of functionalized Mg-IRMOF-74-III-$(CH_2NH_2)_2$ after metalation in comparison with simulated patterns of Mg-IRMOF-74-III-$(CH_2NH_2)_2$ and (b) FT-IR spectra of Mg-IRMOF-74-III-$(CH_2NH_2)_2$-2OHBAL-Ni and Mg-IRMOF-74-III-$(CH_2NH_2)_2$-34OHBAL-Ni in comparison with their parent compounds.

Figure 5.8 shows the low-pressure H_2 adsorption isotherms performed at 77K of Mg-IRMOF-74-III-$(CH_2NH_2)_2$-2OHBAL-Ni and Mg-IRMOF-74-III-$(CH_2NH_2)_2$-34OHBAL-Ni in comparison with Mg-MOF-74 which is the isostructural series of Mg-IRMOF-74-III-$(CH_2NH_2)_2$ except 2,5-dioxido-1,4-benzenedicarboxylate was used as an organic linker. Mg-MOF-74 shows a steep hydrogen uptake at low pressure (isotherm slope as $P \rightarrow 0$)indicating enhanced interaction of H_2 molecules with the MOF.[11] In contrast, Mg-IRMOF-74-III-$(CH_2NH_2)_2$-2OHBAL-Ni and Mg-IRMOF-74-III-$(CH_2NH_2)_2$-34OHBAL-Ni do not show such steep H_2. This could be due to the unoptimized activation conditions designed to remove solvent molecules from the metal sites

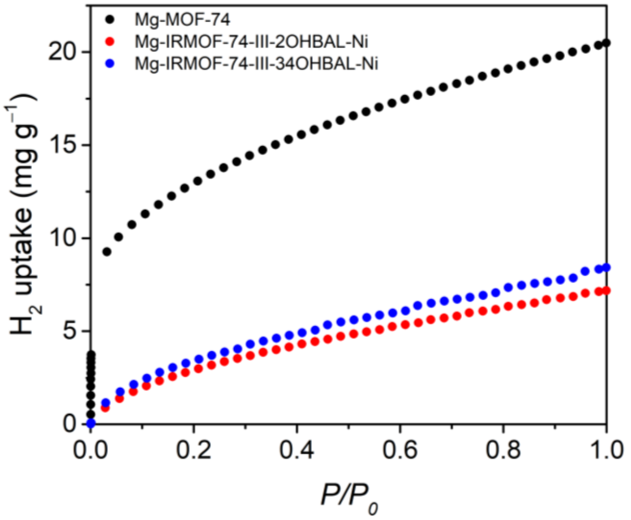

Figure 5.8. Comparison of low-pressure H_2 adsorption isotherms at 77 K of Mg-MOF-74, Mg-IRMOF-74-III-2OHBAL-Ni and Mg-IRMOF-74-III-34OHBAL-Ni.

5.4 Conclusion

This chapter describes the investigation of metalated framework for hydrogen storage. The primary amine functionalities on the organic linker of Mg-IRMOF-74-$(CH_2NH_2)_2$ were used to install ligands with Schiff base and catecholate functionalities. Metalation conditions for the incorporation of Ni(II) into the framework were identified. These materials were found to be crystalline and porous but lack strong interactions with hydrogen molecules. Due to the tunability of this system, this framework can be used as a platform to install other ligands for subsequent metalation and to investigate the effect of the ligands and types of metals for hydrogen adsorption properties systematically.

5.5 Appendices

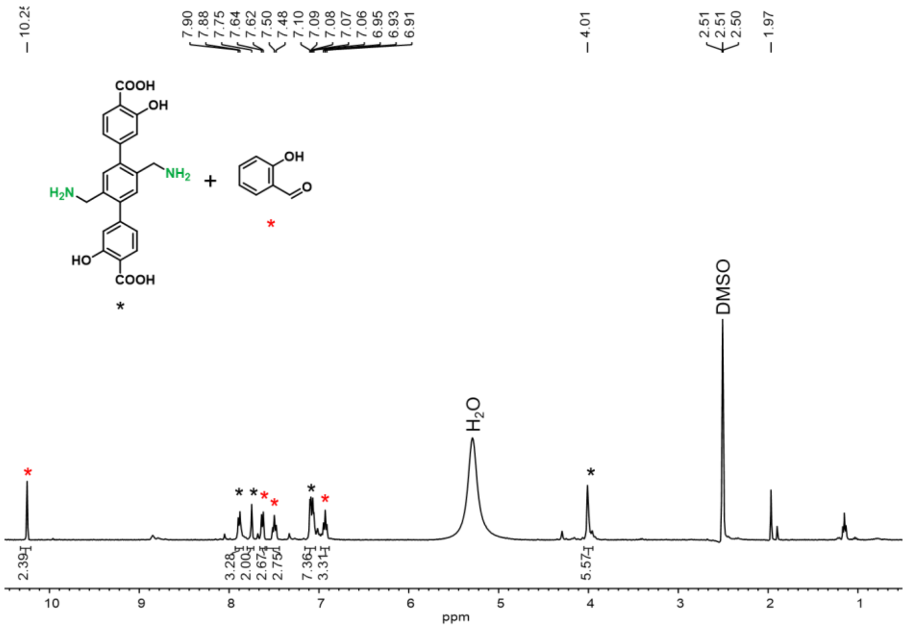

Figure A5.1. Solution ^{1}H NMR of digested Mg-IRMOF-74-III-2OHBAL.

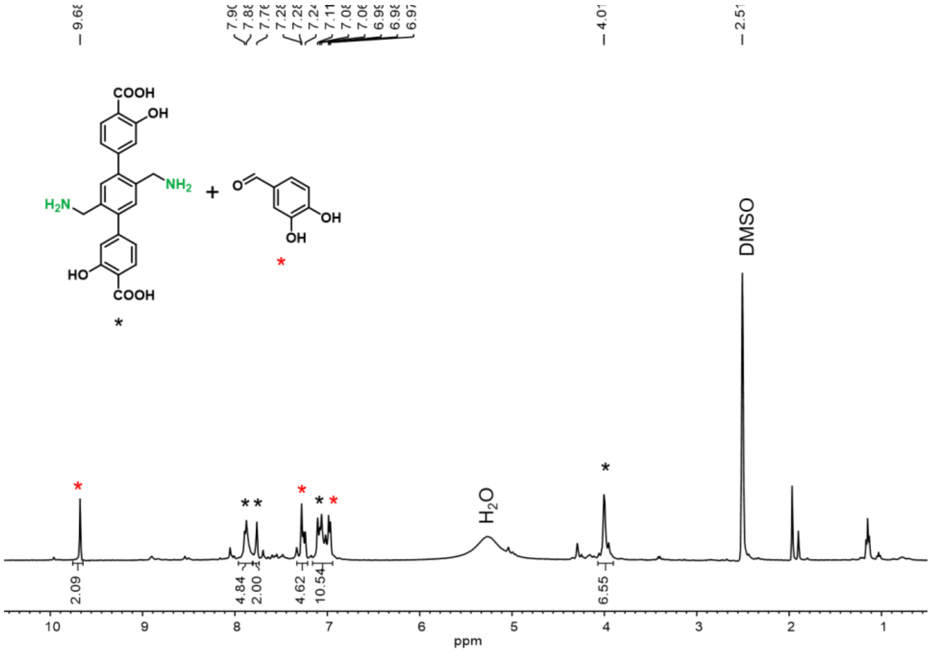

Figure A5.2. Solution ^{1}H NMR of digested Mg-IRMOF-74-III-34OHBAL.

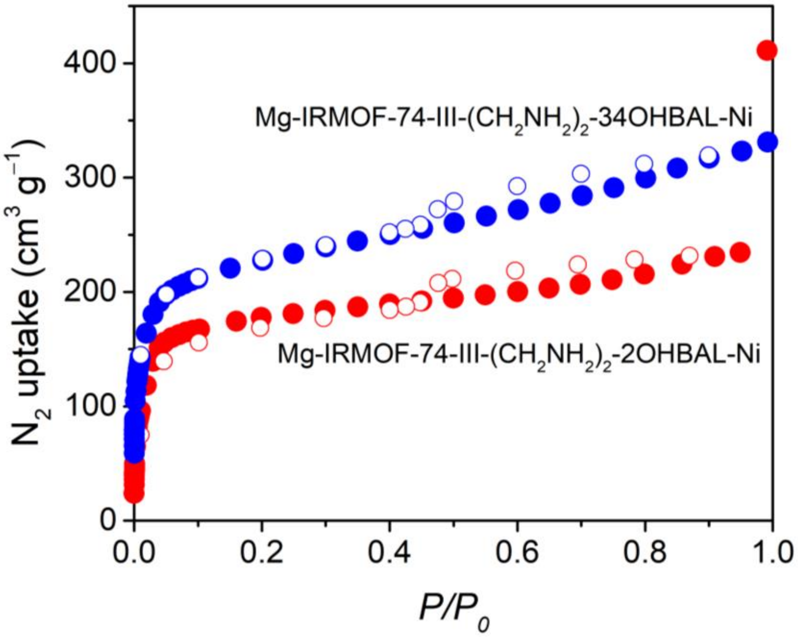

Figure A5.3. N_2 adsorption-desorption isotherms at 77 K with adsorption and desorption points represented by closed circles and open circles, respectively (*P/P*○, relative pressure).

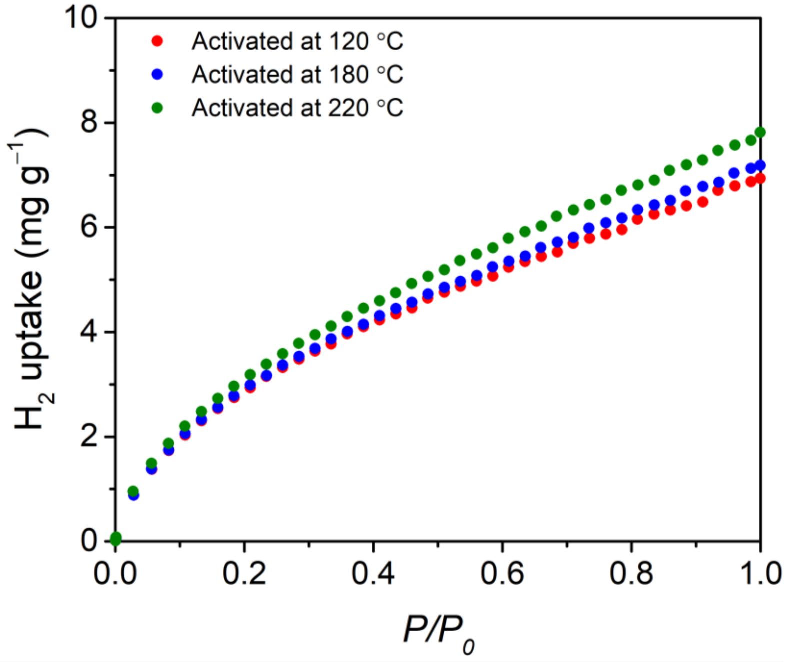

Figure A5.4. Low-pressure H_2 isotherms at 77 K of Mg-IRMOF-74-III-$(CH_2NH_2)_2$-2OHBAL-Ni under different activation temperatures.

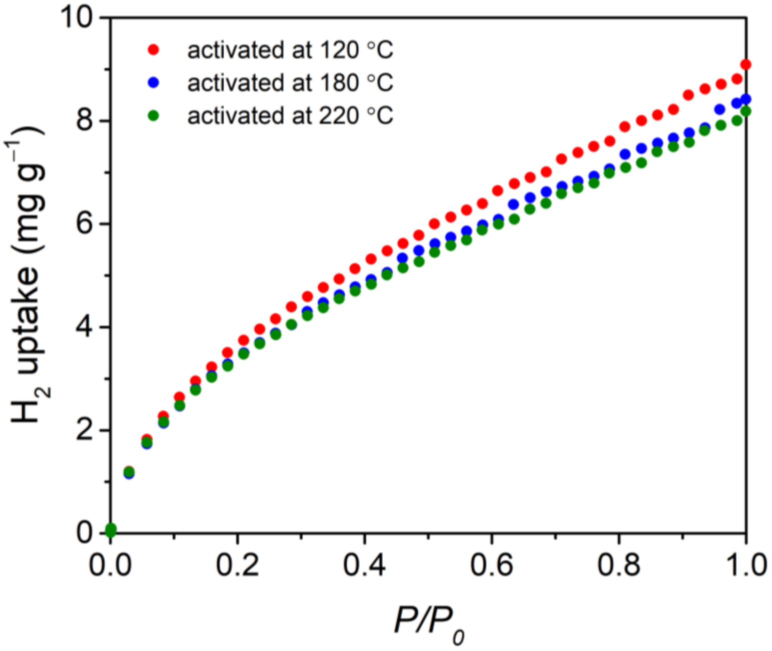

Figure A5.5. Low-pressure H_2 isotherms at 77 K of Mg-IRMOF-74-III-$(CH_2NH_2)_2$-34OHBAL-Ni under different activation temperatures.

5.6 References

(1) Rowsell, J. L.; Yaghi, O. M., *Angew. Chem. Int. Ed.* **2005,** *44*, 4670.

(2) The Toyota Fuel Cell Vehicle. https://ssl.toyota.com/mirai/fcv.html (accessed March 2018).

(3) García-Holley, P.; Schweitzer, B.; Islamoglu, T.; Liu, Y.; Lin, L.; Rodriguez, S.; Weston, M. H.; Hupp, J. T.; Gómez-Gualdrón, D. A.; Yildirim, T., *ACS Energy Lett.* **2018,** *3*, 748.

(4) He, T.; Pachfule, P.; Wu, H.; Xu, Q.; Chen, P., *Nat. Rev. Mater.* **2016,** *1*, 16059.

(5) Rosi, N. L.; Eckert, J.; Eddaoudi, M.; Vodak, D. T.; Kim, J.; O'keeffe, M.; Yaghi, O. M., *Science* **2003,** *300*, 1127.

(6) (a) Tsivion, E.; Long, J. R.; Head-Gordon, M., *J. Am. Chem. Soc.* **2014,** *136*, 17827; (b) Murray, L. J.; Dincă, M.; Long, J. R., *Chem. Soc. Rev.* **2009,** *38*, 1294.

(7) Furukawa, H.; Cordova, K. E.; O'Keeffe, M.; Yaghi, O. M., *Science* **2013,** *341*, 1230444.

(8) Rowsell, J. L.; Millward, A. R.; Park, K. S.; Yaghi, O. M., *J. Am. Chem. Soc.* **2004,** *126*, 5666.

(9) Wong-Foy, A. G.; Matzger, A. J.; Yaghi, O. M., *J. Am. Chem. Soc.* **2006,** *128*, 3494.

(10) Kaye, S. S.; Dailly, A.; Yaghi, O. M.; Long, J. R., *J. Am. Chem. Soc.* **2007,** *129*, 14176.

(11) Rowsell, J. L.; Yaghi, O. M., *J. Am. Chem. Soc.* **2006,** *128*, 1304.

(12) Chen, B.; Eddaoudi, M.; Reineke, T.; Kampf, J.; O'keeffe, M.; Yaghi, O., *J. Am. Chem. Soc.* **2000,** *122*, 11559.

(13) Zhou, W.; Wu, H.; Yildirim, T., *J. Am. Chem. Soc.* **2008,** *130*, 15268.

(14) Kapelewski, M. T.; Geier, S. J.; Hudson, M. R.; Stück, D.; Mason, J. A.; Nelson, J. N.; Xiao, D. J.; Hulvey, Z.; Gilmour, E.; FitzGerald, S. A., *J. Am. Chem. Soc.* **2014,** *136*, 12119.

(15) (a) Deng, H.; Grunder, S.; Cordova, K. E.; Valente, C.; Furukawa, H.; Hmadeh, M.; Gándara, F.; Whalley, A. C.; Liu, Z.; Asahina, S., *Science* **2012,** *336*, 1018; (b) Fracaroli, A. M.; Siman, P.; Nagib, D. A.; Suzuki, M.; Furukawa, H.; Toste, F. D.; Yaghi, O. M., *J. Am. Chem. Soc.* **2016,** *138*, 8352.

(16) Flaig, R. W.; Osborn Popp, T. M.; Fracaroli, A. M.; Kapustin, E. A.; Kalmutzki, M. J.; Altamimi, R. M.; Fathieh, F.; Reimer, J. A.; Yaghi, O. M., *J. Am. Chem. Soc.* **2017,** *139*, 12125.

(17) Wang, L. J.; Deng, H.; Furukawa, H.; Gándara, F.; Cordova, K. E.; Peri, D.; Yaghi, O. M., *Inorg. Chem.* **2014,** *53*, 5881.

(18) Cohen, S. M., *Chem. Rev.* **2011,** *112*, 970.

(19) (a) Cozzi, P. G., *Chem. Soc. Rev.* **2004,** *33*, 410; (b) Garnovskii, A. D.; Nivorozhkin, A. L.; Minkin, V. I., *Coord. Chem. Rev.* **1993,** *126*, 1.

(20) NIST X-ray Photoelectron Spectroscopy Database, NIST Standard Reference Database Number 20, National Institute of Standards and Technology, Gaithersburg MD, 20899 (2000), doi:10.18434/T4T88K, (retrieved April 2018).

(21) Matienzo, J.; Yin, L. I.; Grim, S. O.; Swartz Jr, W. E., *Inorg. Chem.* **1973,** *12*, 2762.

Chapter 6

Conclusions and Future Prospects

The field of MOFs has expanded rapidly over the last few decades with additions of new structures every year and has become the largest class of porous crystalline materials ever made. Different topologies along with their chemical diversities and functionalities have been discovered. Since MOFs are composed of organic and inorganic building units, the chemistry of each component can be explored and studied in a new environment where it was not possible before due to the imparted porosity and well-defined structure. The enhanced chemical stability has enabled a broader range of studies including post-synthetic functionalization and investigation of the properties. Due to a wide variety of structures, post-synthetic functionalization of MOFs with controlled spatial arrangement can serve as a mean to craft highly active species hold in three-dimensional space, similar to an enzyme whose active site are constructed by the folding of secondary structures of proteins. In this thesis, attempts have been made to explore the research in those areas.

In heterogeneous catalysis, strong-metal support interactions (SMSIs) between metal and metal oxide have been shown to influence the catalytic properties through the change in electronic structure, mechanical stability of the catalysts, the surface structure. In many cases, these SMSIs have been used in many industrial catalysts to improve catalyst activity and stability as shown in Cu/ZnO/Al_2O_3 catalyst for methanol synthesis from CO_2/CO/H_2. In Chapter 2, the nanosized nature of metal oxide building unit in MOFs was used to interface with metal for enhanced catalytic activity and selectivity. Through systematic studies, it had been shown there exist the SMSI between metal and metal oxide clusters of MOFs. Such construct enhances the density of interfacial contact significantly.

The work in Chapter 3 utilizes the SMSI between SBU of a MOF and Cu metal to create single atom catalyst for CO oxidation. Without such interaction, these atoms will migrate and sinter during catalysis because of the high surface energy of such single atom. Missing linker defect site in UiO-66 presented on the SBU allows for selective metalation to provide single atom of Cu per cluster. The nature of single atom Cu in Cu/UiO-66 catalyst is preserved throughout catalytic reaction confirming the presence SMSI even in a single atom. As such, one can expect this strategy to be useful in making more single atom catalysts in the future.

Despite the existence of SMSIs in many catalytic systems including ones currently utilized in industries, the interaction between metal and metal oxide is not clearly understood. The well-defined nature of metal oxide SBUs in MOFs offers a unique opportunity to study the interaction in detail using in-situ spectroscopic techniques such as X-ray absorption spectroscopies, X-ray photoelectron spectroscopies, high-resolution transmission electron microscopy and single crystal X-ray diffraction. The latter technique deserves a special emphasis because MOFs can be synthesized as large single crystals coupled with the capability to perform post-synthetic transformations to provide single crystal catalysts for operando studies using SXRD. This will provide definitive molecular level characterizations of the active sites and the mechanistic studies during the reaction. Mixed-metal MOFs coupled with SMSIs can be envisaged as a way to synthesize a new catalyst that was difficult to synthesize in traditional metal oxide due to phase separation problem.

In nature, enzymes have been inspirational for making new kinds of catalysts or to improving upon existing catalysts. Enzymes are known to catalyze a number of reactions, and some notoriously difficult reaction at ambient reaction conditions with high selectivity. Such reactivities led to the studies of synthetic models that reproduce the spectroscopies or occasionally the function of an enzyme. Some of the challenges in duplicating the active site in a synthetic system is brought upon by the difficulty to engineer the spatial arrangement of active species. MOFs offer an opportunity to tackle the challenge. As shown in Chapter 4 of this thesis, by judicious selection of MOF, we have stabilized a highly reactive species within a MOF to make a highly selective catalyst. It is therefore reasonable to contemplate the use of other MOFs with different topology to prepare other catalysts inspired by enzymes. Recent development in the field of artificial metalloenzymes has shown that reconstituting metal not readily available in biological systems such noble in native enzymes can alter catalytic reactivities. The same can be done in MOFs but with additional levels of control.

Regarding hydrogen storage sorbent, MOFs are promising materials for this application due to their adjustability of the gas adsorption sites. Chapter 5 describes an investigation on post-synthetic modifications of MOFs to incorporate additional open metal sites for hydrogen adsorption sites. Although the high volumetric or gravimetric hydrogen capacity has yet to be obtained in this study, the modular nature of this system may provide a way forward in tuning the MOF for improved performance. This can be achieved by changing the metal binding ligands to allow for higher metal loading. High density of open metal sites in close space may enhance the hydrogen adsorption enthalpy with the framework through secondary interactions.